

UNIVERSITY OF NAPLES FEDERICO II

*Department of structures
for engineering and architecture*

PH.D. PROGRAMME IN
MATERIALS ENGINEERING AND STRUCTURES
COORDINATOR PROF. GIUSEPPE MENSITIERI
XXV CYCLE



RAFFAELE DE RISI

PH.D. THESIS

**A PROBABILISTIC BI-SCALE FRAMEWORK FOR URBAN
FLOOD RISK ASSESSMENT**

TUTOR PROF. GAETANO MANFREDI
CO-TUTORS PROF. FATEMEH JALAYER, PROF. IUNIO IERVOLINO

2013

*To my great and wonderful Family,
real core of my passions,
continuous motivation to my improving*

Acknowledgements

Have the opportunity to attend a PhD program, meant for me to continue the study of the engineering topics learned during the master degree, to acquire the knowledge of new concepts and theories, to develop new methodologies and learn new instruments. Most of these expectations has been met. The reaming part it was compensated by the possibility to work in an environment full of bright people, comparison with which increased my desire to improve.

First of all I express my thanks to Prof. Gaetano Manfredi for the opportunity he gave me to join his research group. A special thanks goes to Prof. Iunio Iervolino that helps me in different ways during this three years. Moreover, I would express my thanks to Paolo Gasparini for the opportunity he gave me to enjoy Cluva project and for the possibility to touch by hand the African reality.

All my gratitude goes to Prof. Fatemeh Jalayer, the person that embodies the intellectual honesty and taught me what it means the research. Thanks to her way of doing, it was easier to find the right road to follow.

I would express my thanks to Prof. Francesco De Paola for the crucial support in the understanding of the hydraulic phenomena and for the analytical results in terms of inundation scenario. Moreover a great thanks to all the CLUVA partners for the fruitful mutual cooperation.

I would like to thank Stefano Carozza for his fundamental contribution to the development of VISK platform.

Finally, a special thanks to the people closer to me, that were able to tolerate lack of time stolen from them, whose unconditional love, made me stronger and more determined.

Naples, March 2013

Data Sources

Many data has been used in this work of thesis, work of many expertise in the different disciplines. Below a brief index of the data sources is reported:

- Climate Change prediction: Dr. Eng. Edoardo Bucchignani, CMCC (Centro Euro-Mediterraneo per i Cambiamenti Climatici);

- Hazard maps: Prof. Francesco De Paola, Prof Maurizio Giugni and Eng. Maria Elena Topa, DICEA (Dipartimento di Ingegneria Civile, Edile ed Ambientale);

- UMT maps: Sarah Lindley, Gina Cavan, UM (University of Manchester); Stephan Pauleit, Andreas Printz, Florian Renner, Katja Buchta; TUM (Technische Universität München);

- Addis Ababa city: Kumelachew Yeshitela, Nebyou Yonas, EiABC (Ethiopian Institute of Architecture, Building Construction and City Development, Ethiopia)

- Dar es Salaam city: Alphonse Kyessi, Elinorata Mbuya, IHSS (Institute of Human Settlements Studies, Ardhi University, Dar es Salaam, Tanzania).

Abstract

Quantification of flooding risk in urban areas is necessary as a decision-making support to stakeholders and policy-makers. It can also be effective in reducing the gap between perceived and quantified risk, in short- and long-term. The present work focuses on long-term flood risk assessment in urban areas in meso- and micro-scale. The meso-scale assessment may address an entire city; meanwhile, the micro-scale assessment covers smaller areas such as a neighborhood. This Ph.D. thesis is developed in line with the progress of the European FP7 project Climate Change and Urban Vulnerability in Africa (CLUVA). The flood risk assessment procedure is developed specifically for risk assessment in the African urban context. In the micro-scale, special attention is given to risk assessment for the informal settlements (i.e., non engineered construction). The informal settlements, which can be viewed as a direct product of rapid and un-programmed urbanization, are particularly vulnerable to flooding. They are often located in potentially flood-prone areas and are constructed without formal engineering criteria. The application of the methods adopted and developed in this work is demonstrated for various urban contexts in Africa. Meso-scale applications are presented for cities of Addis Ababa (Ethiopia), Dar es Salaam (Tanzania) and Ouagadougou (Burkina Faso). Detailed micro-scale flood risk assessment has been carried out for the urban informal settlements in the neighborhood of Suna in Dar es Salaam. A micro-scale flood hazard assessment has been performed also for the informal settlements located in the neighborhood of Little Akaki in Ethiopia.

The flood risk assessment problem can be sub-divided into three main components, namely, hazard, vulnerability and exposure. Two different approaches are adopted herein for flood risk assessment in the micro- and meso-scale, respectively.

The micro-scale flood hazard assessment procedure leads to the calculation of the inundation profiles --maximum flood height and velocity for each node within a lattice covering the zone of interest-- for different return periods. This is done, herein, based on both historical rainfall data and future climate projections for the precipitation. The relationship between flood height and velocity at a given point is approximated by a power-law relation. This way, only the flood height is going to be used as an interface variable for calculating flooding risk. Meso-scale flood hazard assessment in this work is based on a geo-spatial dataset of potentially flood prone urban areas, called the Topographic Wetness Index (TWI) map. In this approach, the flood-prone areas are identified by a TWI larger than a certain threshold. A GIS-based Bayesian parameter-estimation method is developed herein in order to estimate the TWI threshold based on the inundation profiles calculated for one or more micro-scale spatial windows. This Bayesian method is also used to estimate the TWI threshold based on the areal extent and delineation of flooding in previous flooding events.

Flood vulnerability assessment can be regarded as the back-bone of this work. An efficient Bayesian and simulation-based algorithm is developed for the assessment of the vulnerability of a class of buildings to flooding. This Bayesian algorithm is based on assigning prescribed analytic uni- and bi-modal probability distributions for characterizing the structural fragility functions. This allows for efficient calculation of structural fragility based on a small number of (around 20-50) Monte Carlo simulations. The fragility calculations, for each of the three limit state defined in the procedure, are performed on a bi-dimensional finite-element structural model considering the openings (door and windows) constructed using the open-source software OpenSees. This vulnerability assessment procedure takes into account the various sources of uncertainty due to building-to-building variability in construction geometry and detailing, and lack of complete knowledge about material mechanical properties and about characteristics of flood action (loading). The uncertain parameters considered in this work are classified into,

discrete binary variables (logical statements) and continuous uncertain variables. The uncertain parameters are characterized by employing various data acquisition tools and methods, such as, orthophoto recognition, building survey, laboratory tests for material mechanical properties and literature survey. Vulnerability of the class of buildings to flooding is represented herein through the *robust fragility curves*, calculated as the statistics (16th, 50th and 84th percentiles) of the set of plausible fragility curves, calculated by considering the above-mentioned sources of uncertainty.

Flood risk assessment in this work is developed both in meso- and micro-scale. The meso-scale flood risk assessment leads to the identification of urban flooding hot spots and the evaluation of exposure to risk. Arguably, identifying the urban flooding hot spots is one of the first steps in an integrated methodology for urban flood risk assessment and mitigation. In this work, three GIS-based datasets are employed for identifying the urban flooding hot spots for residential buildings and urban corridors (i.e., urban roads wider than 15 m). This is done by overlaying a map of potentially flood prone areas (Topographic Wetness Index, TWI), a map of residential areas and urban corridors (extracted from a city-wide assessment of urban morphology types (UMT)), and a geo-spatial Census dataset. For different statistics of the TWI threshold (e.g. MLE estimate, 16th percentile, 50th percentile), the map of the potentially flood prone areas is overlaid with the map of urban morphology units identified as residential and urban corridors in order to delineate the urban hot spots for both urban morphology types. Moreover, information related to population density is integrated by overlaying geo-spatial Census datasets in order to estimate the number of people affected by flooding. Differences in exposure characteristics are also assessed for a range of different residential types.

In the micro-scale, flood risk assessment for a single-class portfolio of buildings is performed by point-wise integration of flooding hazard and the robust fragility curves. Various risk metrics are adopted in this work, namely, the mean annual frequency of exceeding a specific limit state, the annual

probability of exceeding a limit state, expected number of casualties and expected replacement/reconstruction costs. The micro-scale flood risk assessment approach can be viewed as a linear and modular path starting from precipitation data (based on historical data/climate projections), to flood hazard assessment based on analysis of the hydrographic basin, to simulation-based portfolio (class) vulnerability assessment, finally leading to the assessment of flooding risk.

A GIS-compatible computer platform with Matlab®-based graphical user interface is developed in this work: VISK, "Visual Vulnerability & Risk", flooding module. VISK basically mirrors the procedure for micro-scale flood risk assessment developed in this thesis. This is done by performing detailed (micro-scale) flood risk assessment for building stock with more-or-less similar characteristics. The GIS compatibility allows for graphical processing of both input and output to the program, providing an efficient visualization of flooding risk. The results can be visualized both in a detailed building-to-building scale (of potential interest to single house-holds) or as overall estimates for the entire area (of interest to policy makers).

Keywords: Flood, Hazard, Fragility, Exposure, Risk Assessment, Bayesian framework, Flood prone, Topographic wetness index, Urban morphology types, GIS, Informal Settlements, Africa

Tables of contents

CHAPTER 1

INTRODUCTION	23
1.1 MOTIVATION	24
1.2 OBJECTIVES	25
1.3 SCOPE.....	25
1.4 PRODUCTS.....	26
1.5 ORGANIZATION AND OUTLINE	27
1.6 CASE STUDIES.....	28
1.6.1. Dar es Salaam.....	29
1.6.2. Addis Ababa	29
1.6.3. Ouagadougou	30
REFERENCES.....	31

CHAPTER 2

BASIC DEFINITIONS AND DATA REQUIREMENTS.....	33
2.1 HISTORICAL RAINFALL DATA	34
2.2 CLIMATE-CHANGE PROJECTION RAINFALL DATA	35
2.2.1. Climate projections used in this work	37
2.3 GEO-MORPHOLOGIC DATASETS.....	37
2.3.1. Topography: The Digital Elevation Model	38
2.3.2. Geological dataset	38
2.3.3. Land use maps	39
2.4 ORTHOPHOTOS AND THEIR BY-PRODUCTS.....	40
2.4.1. Micro-Scale boundary recognition	40
2.4.2. UMT: Uniform Morphology Types.....	41
2.5 CENSUS INFORMATION	42
2.6 FIELD SURVEY.....	43
2.7 MATERIAL PROPERTIES	43
REFERENCES.....	44

CHAPTER 3

MICRO-SCALE FLOOD HAZARD ASSESSMENT.....	45
3.1 THE RAINFALL CURVE	45
3.1.1. The rainfall curve based on incomplete historical event	48

3.1.2.	<i>Historical Data vs Climate Projections</i>	48
3.2	HYDROGRAPHIC BASIN MODEL	48
3.2.1.	<i>Catchment area definition</i>	49
3.2.2.	<i>Hydrograph building</i>	49
3.2.3.	<i>Two-dimensional propagation model</i>	51
3.3	FLOOD HAZARD CURVES	51
3.4	FLOOD HEIGHT AS AN INTERMEDIATE VARIABLE	53
3.5	THE CASE OF SUNA, DAR ES SALAAM.....	54
3.5.1.	<i>The IDF Curve: Histroical Data and Climate Projections</i>	55
3.5.2.	<i>The definition of the catchment area</i>	57
3.5.3.	<i>The characterization of the hydrographs</i>	59
3.5.4.	<i>The micro-scale flood hazard</i>	60
3.6	THE CASE OF LITTLE AKAKY, ADDIS ABABA	64
3.6.1.	<i>The rainfall-curve</i>	64
3.6.2.	<i>The characterization of the hydrograph</i>	65
3.6.3.	<i>The micro-scale flood hazard</i>	66
REFERENCES.....		68
CHAPTER 4		
MESO-SCALE FLOOD HAZARD ASSESSMENT		69
4.1	THE TOPOGRAPHIC WETNESS INDEX (TWI).....	69
4.1.1.	<i>Delineation of flood-prone areas using the TWI</i>	70
4.2	USING THE INUNDATION PROFILES FOR THE CALIBRATION OF THE TWI THRESHOLD	71
4.3	MAXIMUM LIKELIHOOD ESTIMATION OF THE TWI THRESHOLD	71
4.3.1.	<i>Estimation of the likelihood function using the areal extent: Part 1, the micro- scale estimation</i>	73
4.3.2.	<i>Estimation of the likelihood function using the areal extent: Part 2, the micro- scale estimation</i>	74
4.3.3.	<i>Using Bayesian parameter estimation in order to estimate τ based on information from more than one spatial window</i>	76
4.3.4.	<i>Calibration of TWI threshold based on information other than the inundation profile</i> 77	77
4.4	THE CASE OF ADDIS ABABA	77
4.4.1.	<i>Delineation of flood prone areas for Addis Abab using the topographic wetness index (TWI)</i>	77
4.4.2.	<i>The inundation profile for Little Akaki</i>	78
4.4.3.	<i>Maximum likelihood estimation of the flood-prone threshold</i>	78
4.5	THE CASE OF DAR ES SALAAM	85
4.5.1.	<i>Delineation of flood-prone areas for Dar es Salaam using the topographic wetness index (TWI)</i>	85
4.5.2.	<i>The inundation profile for Suna</i>	86
4.5.3.	<i>Maximum likelihood estimation of the flood-prone threshold</i>	86
4.6	THE CASE OF OUAGADOUGOU	92

4.6.1.	<i>Delineation of flood-prone areas for Ouagadougou using the topographic wetness index (TWI).....</i>	<i>92</i>
4.6.2.	<i>The inundation profile</i>	<i>93</i>
4.6.3.	<i>Maximum likelihood estimation of the flood-prone threshold</i>	<i>94</i>
REFERENCES.....		96
CHAPTER 5		
PORTFOLIO FLOOD VULNERABILITY ASSESSMENT		97
5.1	FLOOD DAMAGE TYPOLOGIES.....	98
5.1.1.	<i>Infiltration-seepage</i>	<i>99</i>
5.1.2.	<i>Material deterioration/erosion</i>	<i>100</i>
5.1.3.	<i>Structural member failure (structural failure).....</i>	<i>100</i>
5.2	THE LIMIT STATES	101
5.2.1.	<i>Serviceability (SE).....</i>	<i>101</i>
5.2.2.	<i>Structural Collapse (CO)</i>	<i>101</i>
5.2.3.	<i>Life Safety (LS)</i>	<i>101</i>
5.3	METHODOLOGY	102
5.3.1.	<i>Spatial delineation of the portfolio and its resolution</i>	<i>102</i>
5.3.2.	<i>Portfolio vulnerability/fragility formulation</i>	<i>103</i>
5.4	VULNERABILITY ASSESSMENT FOR A SINGLE BUILDING CLASS	104
5.4.1.	<i>Data acquisition</i>	<i>104</i>
5.4.2.	<i>The simulation routine</i>	<i>105</i>
5.4.2.1	<i>Characterization of the uncertainties</i>	<i>105</i>
5.4.2.2	<i>Flood Action</i>	<i>110</i>
5.4.2.3	<i>The structural modeling</i>	<i>114</i>
5.4.2.4	<i>Determining the critical water height</i>	<i>118</i>
5.4.3.	<i>The fragility assessment</i>	<i>121</i>
5.4.3.1	<i>The analytical fragility curve</i>	<i>121</i>
5.4.3.2	<i>Updating analytical fragility parameters</i>	<i>124</i>
5.4.3.3	<i>The robust fragilities</i>	<i>125</i>
5.5	APPLICATION: THE CASE OF SUNA, DAR ES SALAAM.....	127
5.5.1.	<i>Data acquisition</i>	<i>127</i>
5.5.2.	<i>The characterization of uncertainties</i>	<i>128</i>
5.5.3.	<i>Preliminary analysis results.....</i>	<i>131</i>
5.5.4.	<i>Numerical results</i>	<i>135</i>
REFERENCES.....		143
CHAPTER 6		
URBAN FLOOD RISK ASSESSMENT		145
6.1	MESO-SCALE FLOOD RISK ASSESSMENT.....	145
6.1.1.	<i>The case of Addis Ababa</i>	<i>147</i>
6.1.2.	<i>The case of Dar es Salaam</i>	<i>155</i>
6.1.3.	<i>Summary and remarks on meso-scale flood risk assessment</i>	<i>160</i>
6.2	MICRO-SCALE FLOOD RISK ASSESSMENT	163

6.2.1.	<i>Risk assessment</i>	165
6.2.2.	<i>Expected loss</i>	166
6.2.3.	<i>Expected number of people affected</i>	166
6.2.4.	<i>The case of Suna in Dar es Salaam</i>	166
REFERENCES		171
CHAPTER 7		
VISK: A GIS-COMPATIBLE PLATFORM FOR MICRO-SCALE ASSESSMENT OF FLOODING RISK IN URBAN AREAS		173
7.1	INTRODUCTION TO FRAMEWORK	174
7.2	INPUT DATA	177
7.2.1.	<i>Orthophoto and footprint of the buildings</i>	177
7.2.2.	<i>Characterization of uncertainties</i>	177
7.2.3.	<i>Hydraulic results and flooding hazard curves</i>	178
7.3	VISUAL VULNERABILITY ASSESSMENT PLATFORM	180
7.3.1.	<i>The limit states</i>	180
7.3.2.	<i>The structural analysis</i>	182
7.3.3.	<i>The analytical fragility curves and robust fragility estimation</i>	183
7.4	VISUAL RISK ASSESSMENT PLATFORM	184
7.4.1.	<i>Exposure to risk</i>	186
7.4.2.	<i>Numerical example</i>	186
7.5	SUMMARY AND FINAL REMARKS	187
REFERENCES		189
CHAPTER 8		
SUMMARY AND FINAL REMARKS		191
APPENDIX A		
THE SAMPLE FILED SURVEY SHEET		199

List of figures

Figure 1.1 - Scales of work considered.....	26
Figure 1.2 - Reading path.....	28
Figure 1.3 - The three African urban contexts considered in this thesis	29
Figure 2.1 - The Global Circulation model [3].....	36
Figure 2.2- DEM of Addis Ababa (overlaid with the main water courses)	38
Figure 2.3 - Boundary recognition based on the orthophotos	41
Figure 2.4 - Mapping UMT units (b) using ortho-rectified aerial photography (<i>source www.bing.it/maps</i>) (a), an example in Addis Ababa.....	42
Figure 3.1 - Hydrographic basin modeling procedure	49
Figure3.2 - The schematic diagram of a hydrographic basin.....	50
Figure 3.3 - Graphical representation of the spatial interpolation for point G.....	52
Figure 3.4 - a) Hazard curves, b) Flood height versus flood velocity power-law relation	54
Figure 3.5 - The case study area and the portfolio of the buildings studied.	55
Figure 3.6 - Rainfall Probability Curves for Dar es Salaam with and without climate change (CC) effects.	57
Figure 3.7 - Visualization of the Mzimbazi catchments with the position of the case- study area.....	58
Figure 3.8 - Mzimbazi River catchments: a) Land use, b) Geology.....	59
Figure 3.9 - Hydrographs evaluated for catchment 1 ($T_R= 2, 10, 30, 50, 100$ and 300 years) with and without CC effects	59
Figure 3.10 - The hazard curves a) considering the historical data and b) considering the climate projections.....	61
Figure 3.11 - Overlaying of the representative (mean and mean +/- standard deviation) hazard curves obtained based on, historical data (the blue curves) and climate projections (red curves).....	61

Figure 3.12 - Inundation profiles for different return periods, based on historical data, in terms of h_{\max} : a) $T_R=2$ years, b) $T_R=10$ years, c) $T_R=30$ years, d) $T_R=50$ years, e) $T_R=100$ years, f) $T_R=300$ years.....	62
Figure 3.13 - Inundation profiles for different return periods, based on historical data, in terms of v_{\max} : a) $T_R=2$ years, b) $T_R=10$ years, c) $T_R=30$ years, d) $T_R=50$ years, e) $T_R=100$ years, f) $T_R=300$ years.....	63
Figure 3.14 - Rainfall probability curves for Addis Ababa with and without climate change effects.....	65
Figure 3.15 - Hydrographs ($T_R= 10, 30, 50, 100$ and 300 years) with and without CC effects	66
Figure 3.16 - Inundation profiles based on historical data in terms of h_{\max} (in meters) for various return periods for the case study area (Little Akaki)	67
Figure 4.1 - The main components of the TWI calculation.	70
Figure 4.2 - FP and IN areas	72
Figure 4.3 - Identification of the total urban area (A_{urban}) and the flood prone urban area ($A_{urban} (FP)$) for a given threshold.....	75
Figure 4.4 - TWI for Addis Ababa	78
Figure 4.5 - The TWI and the spatial the window for hydraulic analyses at Little Akaki	79
Figure 4.6 - a) Probability of being FP and IN given τ . b) Probability of being \overline{FP} and \overline{IN} given τ	80
Figure 4.7 - a) The likelihood function $L(\tau W)$ (also the probability density for τ); b) threshold CDF.	81
Figure 4.8 - Overlay of FP and IN areas for the spatial window W (Little Akaki).....	82
Figure 4.9 - a) The likelihood function $L(\tau W)$. b) threshold CDF for different return periods.....	83
Figure 4.10 - a) Zones 1 and 2. b) $p(\tau W_1)$:the posterior distribution calculated for the Zone1 and used as prior for Zone 2.....	84
Figure 4.11 - a) the likelihood $L(\tau W_2)$; b) the posterior distribution $p(\tau W_1,W_2)$	85
Figure 4.12 - TWI for Dar Es Salaam	86
Figure 4.13 - The TWI and the spatial the window for hydraulic analyses at Suna	87
Figure 4.14 - a) Probability of being FP and IN given τ . b) Probability of being \overline{FP} and \overline{IN} given τ	88
Figure 4.15 - a) The likelihood function $L(\tau W)$ (also the probability density for τ); b) threshold CDF.....	89

Figure 4.16 - Overlay of FP and IN areas for the spatial window W.....	90
Figure 4.17 - a) The likelihood function $L(\tau W)$. b) threshold CDF for different return periods.....	91
Figure 4.18 - TWI for Ouagadougou	92
Figure 4.19 - Inundated area of in the September 2009 flooding event.....	93
Figure 4.20 - a) Inundated areas after the 2009 events, b) Area 1 (the smaller) and Area 2 (the bigger).....	93
Figure 4.21 - The likelihood function $L(\tau W_1, W_2)$, b) threshold CDF	94
Figure 4.22 - a) Matching for the inundate areas, b) flood prone areas for the entire city.....	95
Figure 5.1 - a) The frame delineating the spatial extension of the portfolio; b) Division of the portfolio frame into spatial units.....	102
Figure 5.2 - The schematic diagram of the procedure used for the assessment of the vulnerability of the portfolio of structures.	104
Figure 5.3 - a) logic tree for the waterproofness, b) logic tree for the modeling generation.	109
Figure 5.4 - a) velocity profile along the height, b) approximate velocity profile.....	112
Figure 5.5 - Break-down of the flood pressure profile into hydro-static and hydro-dynamic components for two different pairs of parameters: (a) low flooding height and low velocity; (b) low flooding height and high velocity.....	113
Figure 5.6 - Various structural configurations considered in the analysis (the number of the openings is randomized based on the wall length).	116
Figure 5.7 - Zones of panel in which is searched the critical section.	117
Figure 5.8 - Evaluation of critical flooding height in various situations corresponding to possible Monte Carlo extractions.....	120
Figure 5.9 - schematic diagrams of: a) step function for SE; b) the Lognormal CDF for SE; c) the three-parameter CDF for SE; d) step function for LS; e) the Lognormal CDF for SL; f) the three-parameter CDF for SL	123
Figure 5.10 - Three alternative possibilities for estimating the probability that the building has a raised platform: the entire distribution, the maximum likelihood estimate and the expected value	130
Figure 5.11 - Fragility curves for the four wall typologies and three loading combinations: hinged on the sides	133
Figure 5.12 - Fragility curves for the four wall typologies and three loading combinations: fixed in the sides.....	134

Figure 5.13 - Fragility curves for the four wall typologies and three loading combinations: hinged on the sides, considering the flooding height/velocity relationship similar to point P2 in Figure 3.4	135
Figure 5.14 - The robust fragility curves (SE).....	136
Figure 5.15 - The robust fragility curves (LS).....	136
Figure 5.16 - The robust fragility curves (20 simulations) and the empirical fragility curve calculated based on 200 simulations (CO).....	137
Figure 5.17 - The robust fragility curves (SE): sampling from the full distribution	138
Figure 5.18 - The robust fragility curves (SL): sampling from the full distribution	138
Figure 5.19 - The robust fragility curves (sampling from the full distribution, 20 extractions) and the empirical fragility curve calculated based on 200 simulations (CO).....	139
Figure 5.20 - Overlay of the median fragilities for the three limit states considered for the two typology of extraction	140
Figure 5.21 - The robust fragility curves (SE): sampling from the full distribution, 50 extractions.....	141
Figure 5.22 - The robust fragility curves (SL): sampling from the full distribution, 50 extraction.....	141
Figure 5.23 - The robust fragility curves (sampling from the full distribution, 50 extractions) and the empirical fragility curve calculated based on 500 simulations (CO).....	142
Figure 6.1 - Hazard (H), Vulnerability (V) and Risk (R), the concept of an urban hot-spot.....	146
Figure 6.2 - High level UMT map for Addis Ababa (2011)	148
Figure 6.3 - The urban residential flood hot spots delineated for different TWI thresholds: a) residential area, b)16 th percentile, c) τ^-_{ML} , d) maximum likelihood, e) 50 th percentile, f) τ^+_{ML}	150
Figure 6.4 - TWI threshold - number of people	151
Figure 6.5 - Breakdown of the residential hot-spot in terms of flood prone residential area and people affected by flooding in the residential area.	152
Figure 6.6 - The urban corridor hot spots for flooding delineated for different TWI thresholds: a) residential area, b)16 th percentile, c) τ^-_{ML} , d)maximum likelihood, e) 50 th percentile, f) τ^+_{ML}	154
Figure 6.7 - High level UMT map for Dar es Salaam.	155

Figure 6.8 - The urban residential hot spots for flooding delineated for different TWI thresholds: a) residential area, b)16 th percentile, c) $\bar{\tau}_{ML}$, d)maximum likelihood, e) 50 th percentile, f) $\bar{\tau}_{ML}^+$	157
Figure 6.9 - Breakdown of the residential hot-spot in terms of flood prone residential area and people affected by flooding in the residential area.	158
Figure 6.10 - The urban corridor hot spots for flooding delineated for different TWI thresholds: a) residential area, b)16 th percentile, c) $\bar{\tau}_{ML}$, d)maximum likelihood, e) 50 th percentile, f) $\bar{\tau}_{ML}^+$	160
Figure 6.11 - Flow-chart representation of the micro-scale flood risk assessment methodology (special application to a portfolio of informal settlements).	165
Figure 6.12 - Superposition of robust fragility curves and flooding hazard curves (SL, historical data)	167
Figure 6.13 - The mean annual rate of exceeding the life safety limit state, Suna Subward (historical rainfall data)	168
Figure 6.14 - Annual probability of exceeding the critical flooding height for Suna subward (historical rainfall data).....	169
Figure 6.15 - Expected number of people affected by flooding in a year corresponding to a) Fragility- σ b) Fragility and c) Fragility+ σ	169
Figure 6.16 - Expected annual replacement costs per building relative to a) Fragility- σ b) Fragility and c) Fragility+ σ (Suna Subward, historical rainfall data).	170
Figure 7.1 - The graphical user interface of VISK.....	175
Figure 7.2 - Inundation profiles for a given return period in terms of a)flood depth and b) flood velocity [5]	179
Figure 7.3 - Hazard curves in terms of maximum flood a) height, b) velocity and c) relation between flood height and flood velocity. [5]	180
Figure 7.4 - Histogram of critical section/mode of failure corresponding to h_{cr} for a set of N=200 simulations.....	183
Figure 7.5 - Robust Fragility curves and their plus/minus one standard deviation interval (SE), (LS) and (CO), respectively.....	184
Figure 7.6 - Risk maps in terms of mean annual rate of exceeding the collapse limit state [5]	185
Figure 7.7 - Risk maps in terms of the annual probability of exceeding the collapse limit state [5]	185
Figure 7.8 - The expected number of casualties [5]	186
Figure 7.9 - The expected replacement cost [5].....	187

List of tables

Table 3.1 - Growing factors for the different return periods (H:historical, CC: climate change)	56
Table 3.2 - The characteristics of the Mazimbazi River catchments.....	58
Table 3.3 - Growing factors for the different return periods (H:historical, CC: climate change)	64
Table 4.1 - The statistics for the <i>TWI</i> threshold distribution as a function of the return period.....	83
Table 4.2 - The statistics for the <i>TWI</i> threshold distribution as a function of the return period.....	91
Table 4.3 - The statistics for the <i>TWI</i> threshold distribution for the case of Ouagadougou.....	94
Table 5.1 - Discrete binary uncertain variables considered in the procedure.....	106
Table 5.2 - The continuous uncertain parameters: building geometry.....	107
Table 5.3 - The continuous uncertain parameters: material mechanical properties	108
Table 5.4 - Cement stabilized blocks available in literature [31]	128
Table 5.5 - Structural detailing parameters expressed as discrete binary uncertain variables	129
Table 5.6 - Continuous uncertain parameters related to building geometry.....	130
Table 5.7 - Continuous uncertain parameters related to material mechanical properties (cement-stabilized bricks)	131
Table 5.8 - Continuous uncertain parameters related to loading parameters	131
Table 6.1 - Exposure to flooding risk in terms of the estimated percent of residential area and people affected by flooding	151
Table 6.2 - Exposure to flooding risk in terms of the estimated percent of residential people affected by flooding respect to the entire city population.....	152
Table 6.3 - Exposure assessment in terms of urban corridors.....	154
Table 6.4 - Exposure to flooding risk in terms of the estimated percent of residential area and people affected by flooding.....	157

List of tables

Table 6.5 - Exposure to flooding risk in terms of the estimated percent of residential people affected by flooding respect to the entire city population.....	158
Table 6.6 - Exposure assessment in terms of urban corridors.....	160

Chapter 1

INTRODUCTION

Hydro-meteorological or climate-related hazards, such as storms, droughts, floods and landslides, transform into natural disasters when they hit vulnerable areas. In the last decades, climate-related disasters alone accounted for between 70-90 percent of the natural disasters around the globe [1]. Only in the first semester of the 2012, 35% of natural disasters were related to floods, and accounted for the 62% total people affected and almost 10% of the total economic losses [2] due to natural disasters. Moreover, the rapid rate of urbanization leads to an increase the exposure to risk in urban areas. It is sufficient to highlight that around half of the world's population lives in urban areas at present; by 2050, this ratio is estimated to rise up to around 70% [3]. One of the most significant consequences of the rapid urbanization process is the phenomenon of the squatter settlements also known as the informal settlements, shanty towns, and slums. Although they defer slightly in their definitions, these denominations all refer to generally poor standards of living and construction. This kind of construction, generally, can be seriously damaged by weather-related events since it is not covered by design standards or regulations.

Furthermore, there is increasing evidence in the favor of a correlation between the climate change and extreme weather-related phenomena [4]. In this regard, assessment and prediction of the adverse effects of climate change on the frequency and/or intensity of extreme weather-related events and delineation of the potentially vulnerable areas are --undoubtedly-- important steps in an integrated climate change adaptation strategy.

1.1 Motivation

The work presented in this thesis is developed in the context of the FP7 project CLUVA (Climate Change and Urban Vulnerability in Africa). One of the project's goals is to define a methodology to quantify the climate-related risk in the African urban context. Special attention is dedicated to the urban informal settlements, which can be regarded as a direct consequence of rapid and un-programmed urban development. Moreover, these constructions are particularly vulnerable to climate-related hazards --due to both their location (usually built near rivers) and generally poor standards of construction.

This study presented particular challenges with regard to: a) lack of complete information and b) study of unconventional types of buildings. A Bayesian probabilistic framework for flood risk assessment seemed particularly suitable for characterization of uncertainties; both with regard to lack of information and also as a means of taking into account the building-to-building variability in construction detailing and geometry.

The flooding risk (e.g., casualties, downtime, financial losses, ..., etc.), due to flooding) can be evaluated as the convolution of Hazard (H), Vulnerability (V) and Exposure (E). Flood risk assessment involves many different disciplines and fields of expertise (e.g., climatologists, meteorologists, hydrologists, hydraulic and structural engineers, GIS experts, risk analysts, etc.) and various data (e.g., topography, rainfall history, land use, geology, exposure, ..., etc.). In the recent years, increasing attention is focused on flood risk assessment. Indeed, several publications discuss the consequences of flooding, such as loss of life [5], economic losses [6-8] and damage to buildings [9-13]. These research efforts have many aspects in common, such as a direct link between the flooding intensity and the incurred damage, or the fact that they are based on real damage observed in the aftermath of the flooding events. On the other hand, many research efforts are starting to galvanize in the direction of proposing analytical models for flood hazard and vulnerability assessment taking into account the various sources of uncertainty in this

problem. Nadal et al. [14] propose a stochastic method for the assessment of the direct impact of flood actions on buildings. A general methodological approach to flood risk assessment is embedded in the HAZUS procedures for risk assessment [15, 16]. Finally Apel et al. [17] have carried out a comprehensive study on the various scales of complexity and precision involved in the flood risk assessment.

1.2 Objectives

The general objective of this thesis is to contribute to the development of methods and tools for urban flood risk assessment with particular attention to non-engineered structures --referred to also as informal settlements. To achieve this general objective, attention was focused on specific issues related to the three basic elements of the risk assessment: hazard, vulnerability and exposure.

The first objective of this thesis is create quantitative methodologies and tools as decision-making support to the policy-maker and to stakeholders, for the long-term urban planning and, potentially, for the short-term emergency management planning.

The second objective is reduce the gap between the perceived and the quantified risk by laying out a quantified risk assessment procedure. Arguably, disseminating the outcomes of a quantified risk assessment procedure to a wider audience can contribute significantly in raising the level of public awareness.

1.3 Scope

This scope of this thesis can be laid out from many different aspects: the level of precision (accurate or approximate), the temporal scale (short- or long-term) and the spatial scale (meso- or micro-scale). Figure 1.1 below lays out a schematic representation of the scope and various working scales considered

in this thesis.

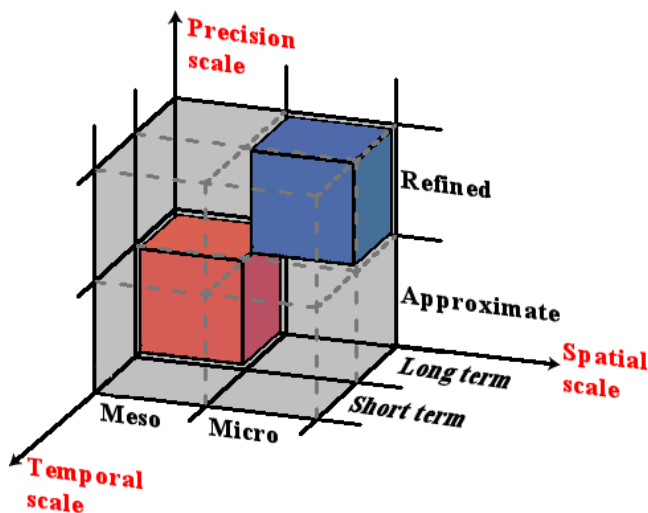


Figure 1.1 - Scales of work considered

The bi-scale framework, emphasized in the title, refers to the spatial scale. As it will be described in the following, the level of accuracy of the methods adopted is closely related to the spatial scale of the problem. In particular, the more accurate methods are employed for flood risk assessment in the micro-scale (e.g., a neighborhood). Meanwhile, the less accurate methods are employed for flood risk assessment in the meso-scale (e.g., an entire urban area). As far as it regards the temporal scale, the methodology and the instruments developed in this thesis are particularly useful for long-term strategic urban planning. Of course, they can be potentially useful in planning of emergency response.

1.4 Products

In this section various final products of this thesis are outlined. The order of presentation reflects the linear path from hazard, to vulnerability, and finally to risk:

1. Definition of a Bayesian meso-scale flood hazard assessment framework based on available information (e.g., classical micro-scale flood hazard assessment procedures, flooded areas in the past, etc.).
2. Development of a Bayesian simulation-based method for assessment of portfolio vulnerability to flooding, with particular application for a single class of buildings (the informal settlements in a given neighborhood). These is used later on for point-wise micro-scale flood risk assessment for the zone of interest.
3. Development of a GIS-based flood risk assessment methodology in the meso-scale. This involves overlaying three different geo-spatial datasets in order to take into account information related to hazard and exposure.
4. Building a software platform and graphical user interface for micro-scale flood risk assessment for a mono-class portfolio of structures.

1.5 Organization and outline

This work presents an integrated modular probabilistic methodology for predicting the urban flooding risk on a detailed micro-scale (e.g., a neighborhood) and meso-scale (e.g. city level), in a framework compatible with the Geographical Information System (GIS).

This modular approach is reflected in the general organization of the work. The schematic diagram in Figure 1.2 illustrates the organization of the thesis into chapters. Moreover, this flowchart emphasizes the logical connections between different chapters.

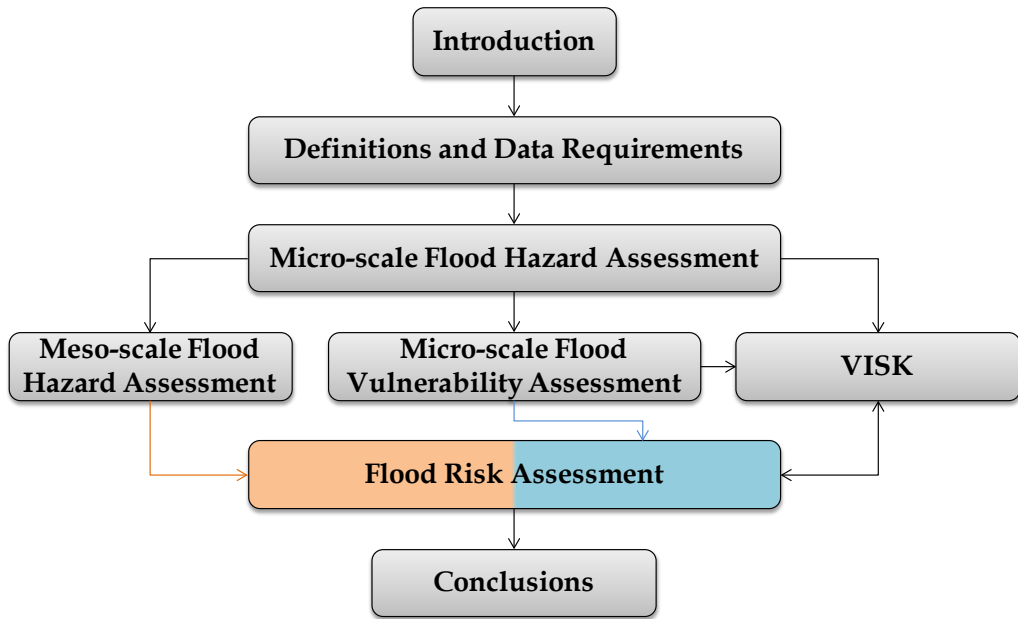


Figure 1.2 - Reading path

The thesis is divided into eight chapters, namely, the introduction (**Chapter 1**, the present chapter), basic concepts, definitions and data acquisition (**Chapter 2**), flood hazard assessment (micro-scale, **Chapter 3**), flood hazard assessment (meso-scale, **Chapter 4**), portfolio vulnerability assessment (**Chapter 5**), risk assessment (micro- and meso-scale, **Chapter 6**), software platform development (**Chapter 7**), and the final remarks (**Chapter 8**).

1.6 Case studies

The application of the methodology and instruments developed in this thesis is demonstrated for different urban contexts within Africa. In particular, on the meso-scale (city-level), the three cities of, Dar Es Salaam (Tanzania), Addis Ababa (Ethiopia) and Ouagadougou (Burkina Faso) are studied (Figure 1.3). In the micro-scale, a complete risk assessment procedure is carried out for the informal settlements in the neighborhood of Suna, Dar es Salaam.

Moreover, micro-scale hazard assessment results are processed and presented for some informal settlements in the zone of Little Akaki in Addis Ababa.



Figure 1.3 - The three African urban contexts considered in this thesis

1.6.1. *Dar es Salaam*

The city of Dar es Salaam (DSM) in Tanzania is located between latitudes 6.36° and 7.0° to the South of Equator and longitudes 39.0° and 33.33° to the East of Greenwich. It borders Indian Ocean on the east and its coastline stretches about 100 km between the Mpiji River to the north and the Mzinga River in the south.

The total surface area of Dar es Salaam city is about 1800 km², comprising of 1393 km² of land mass with eight offshore islands, which is about 0.19% of the entire Tanzania Mainland's area. Administratively, Dar es Salaam City is divided into three municipalities and Districts of Kinondoni, Ilala and Temeke, with a total population of 2698651 according to the 2005 population census.

1.6.2. *Addis Ababa*

Addis is the capital and the largest city in Ethiopia, with a population of

2739551 according to the 2007 population census. The city is situated in the high plateau of central Ethiopia in the North-South oriented mountain systems neighbouring the Rift-Valley. The city is overlooked by Mount Yarer in the east, Mount Entoto in the north and Mount Wochecha in the west.

Several small streams originate in the mountains surrounding the city and flow into the metropolitan area of Addis Ababa. Torrential rains, which are common during the rainy season, cause a sudden rise in the flow of these streams and periodically inundate the settlements built along their banks. This problem is exacerbated by the large tracts of Eucalyptus plantations which inhibit sufficient undergrowth, by soil erosion and or drainage [18].

The flooding of August 2006 was the worst in Ethiopian history. It affected 363000 people and left approximately 200000 people homeless [19]. The final death toll is estimated at around 647 but the impacts on health and wellbeing are much larger. Lifelines were affected across the whole country. For instance, the telephone and power lines were interrupted and the main roads to Addis Ababa were blocked rendering the city inaccessible. Last but not least, the floods had a severe impact on urban agriculture, leading to widespread food shortages in one of the world's poorest states.

1.6.3. Ouagadougou

Ouagadougou is the capital of the Burkina Faso, is placed situated on the central plateau (12.4° N 1.5° W) of the country. It has a population of 1475223 peoples and covers an area of 219.3 km². The city is part of the Soudano-Sahelian area, with a rainfall of about 900 mm per year. The rainy season stretches from May to October. On September 1, 2009, an unprecedented deluge of rain hit the capital city of Ouagadougou and resulted in wide-spread damage (destruction of buildings and infrastructure). More than 25 cm of rainfall in 12 hours turned the streets of Ouagadougou into fast-flowing rivers. The infrastructure were severely affected as the floods cut off electricity, fresh water and fuel supplies.

References

1. Hoyois P. and Guha-Sapir D., *Measuring the Human and Economic Impact of Disasters*, Report 297. 2012, Center for Research on the Epidemiology of Disaster. Available from: <http://www.bis.gov.uk/assets/foresight/docs/reducing-risk-management/supporting-evidence/12-1295-measuring-human-economic-impact-disasters.pdf>. Data last access: 01/01/2013.
2. CRED, *Disaster Data: A Balanced Perspective*, Report 299. 2012, Centre for Research on the Epidemiology of Disasters. Available from: <http://cred.epid.ucl.ac.be/f/CredCrunch29.pdf>. Data last access: 01/01/2013.
3. UN-HABITAT, *State of the World's Cities 2010/2011 - Cities for All: Bridging the Urban Divide*, Report in State of the World's Cities. 2010. Available from: <http://www.unhabitat.org/pmss/listItemDetails.aspx?publicationID=2917>. Data last access: 01/01/2013.
4. Khan S. and Kelman I., *Progressive climate change and disasters: connections and metrics*. Natural Hazards, 2011. **61**: p. 1477-1481.
5. Jonkman S.N., Vrijling J.K., and Vrouwenvelder A.C.W.M., *Methods for the estimation of loss of life due to floods: a literature review and a proposal for a new method*. Natural Hazards, 2008. **46**: p. 353-389.
6. Pistrika A. and Tsakiris G., *Flood risk assessment: A methodological framework*, in *Water Resources Management: New Approaches and Technologies*. European Water Resources Association, Chania, Crete-Greece. 2007.
7. Pistrika A.K. and Jonkman S.N., *Damage to residential buildings due to flooding of New Orleans after hurricane Katrina*. Natural Hazards, 2009. **54**: p. 413-434.
8. Pistrika A., *Flood Damage Estimation based on Flood Simulation Scenarios and a GIS Platform*, in *EWRA 7th International Conference "Water Resources Conseroancy and Risk Reduction Under Climatic Instability"*. 2009: Limassol, Cyprus. p. 419-427.
9. Smith D., *Flood damage estimation- A review of urban stage-damage curves and loss functions*. Water S. A., 1994. **20**(3): p. 231-238.
10. Kang J., Su M., and Chang L., *Loss functions and framework for regional flood damage estimation in residential area*. Journal of Marine Science and Technology, 2005. **13**(3): p. 193-199.
11. Schwarz J. and Maiwald H., *Damage and loss prediction model based on the vulnerability of building types*, in *4th International symposium of Flood Defence*. 2008: Toronto, Canada.
12. Chang L., Kang J., and Su M., *Depth-Damage Curve for Flood Damage Assessments Industrial and Commercial Sectors*, in *4th IASME/WSEAS Int. Conference on Water resources, Hydraulics & Hydrology*. 2009: Cambridge, UK.
13. Schwarz J. and Maiwald H., *Empirical vulnerability assessment and damage for description natural hazards following the principles of modern macroseismic scales*, in *14th WCEE - World Conference of Earthquake Engineering*. 2012: Lisboa, Portugal.

14. Nadal N.C., Zapata R.E., Pagán I., López R., and Agudelo J., *Building damage due to riverine and coastal floods*. Journal of Water Resources Planning and Management, 2009. **136**(3): p. 327-336.
15. Scawthorn C., Blais N., Seligson H., Tate E., Mifflin E., Thomas W., Murphy J., and Jones C., *HAZUS-MH flood loss estimation methodology. I: Overview and flood hazard characterization*. Natural Hazards Review, 2006. **7**(2): p. 60-71.
16. Scawthorn C., Flores P., Blais N., Seligson H., Tate E., Chang S., Mifflin E., Thomas W., Murphy J., and Jones C., *HAZUS-MH flood loss estimation methodology. II. Damage and loss assessment*. Natural Hazards Review, 2006. **7**(2): p. 72-81.
17. Apel H., Aronica G.T., Kreibich H., and Thieken A.H., *Flood risk analyses – how detailed do we need to be?* Natural Hazards, 2008. **49**: p. 79-98.
18. Belete D.A., *Road and urban storm water drainage network integration in Addis Ababa: Addis Ketema Sub-city*. Journal of Engineering and Technology Research, 2011. **3**(7): p. 217-225.
19. DRMFS. *Flah appeal for the 2006 Flood Disaster in Ethiopia*. 2006; Available from: <http://www.dppc.gov.et/downloadable/reports/appeal/2006/Flood%20Appeal%20II%20MASTER%20Final.pdf>.

Chapter 2

BASIC DEFINITIONS AND DATA REQUIREMENTS

Riverine Flooding phenomena can be triggered by natural processes, such as heavy precipitation or snowmelt, or by the failure of man-made structures such as levees, dams, and drainage systems (in urban areas). The impact of flooding can be quantified in terms of depth, peak discharge, extent of area inundated, and volume of water flow. Floods vary in size and scale, ranging from minor waterlogged fields or briefly blocked roads to the total inundation and destruction of homes and other structures, and casualties. Catastrophic flooding events take place with a certain regularity over long periods of time (in the order of one to hundreds of years). Therefore, one way to classify the recurrence characteristics of a flooding event is in terms of its *return period* (T_R). In evaluating inland river floods, the basic hydrological unit in river systems is the *drainage basin*, or *catchment* (i.e. the area that drains to any defined point along the river network). After a dry spell, rain-fall infiltrates into the upper layers of soil and rock and only a small amount of water runs off in the catchment. However, continuing rain may lead to saturation of the surface soil layers; and as a result, the volume of water will eventually exceed the amount that can be absorbed. At this point, surface runoff begins. The proportion of total rainfall that is transformed to surface runoff over a catchment is called the *runoff coefficient*.

Surface runoff usually starts as *sheet flow* in which water moves as a thin, continuous film over relatively smooth soil or rock surfaces and it is not concentrated into channels. As the volume of water increases, it forms tiny rills, then gullies, and then flows into small tributary streams.

The triggering of a flooding event is determined by many factors, such as:

- the amount of prior rainfall, which determines the degree of soil saturation—referred to in this document as *antecedent moisture condition*;
- topography of the drainage basin;
- type of soil and land use;
- intensity of rainfall.

Extended wet periods during any season can lead to saturated soil conditions. In such cases, additional rainfall will shortly run off into streams and rivers. At some point, the run-off volume is going to exceed the river holding capacity and lead to flooding.

At times, very heavy rainfall is followed almost immediately by a large run-off volume, despite highly pervious and dry soil conditions. This condition is usually caused when large volumes of rainfall take place in a short interval of time. Such bursts of extreme rainfall can produce spatio-temporally localized and devastating flooding events known as the *flash floods*.

It is particularly challenging to create a mathematical model of flooding due to its spatio-temporal complexity and multi-stage triggering process. As a consequence, quantified flood risk assessment demands considerable amount of data and information. Hence, data acquisition plays a pivotal role in a quantified flood risk assessment framework. This cross-cutting chapter is dedicated to discuss the basic concepts and data requirements for a quantified flood risk assessment procedure.

2.1 Historical rainfall data

As defined before, the riverine flooding events are strictly connected to rainfall patterns. Therefore, the rainfall data time-series are essential pieces of information for determining the total flooding discharge. They can be obtained as pluviometer records from governmental organizations and/or internet sources (e.g., www.tutiempo.net and www.knmi.nl). It is desirable (as will be shown in Chapter 3) that the pluviometric data are available as precipitation

extremes (maxima) recorded over a range of time intervals. The rainfall maxima recorded for different intervals are used in order to construct the rainfall curve, also known as, the Intensity-Duration-Frequency (IDF) curve. The historical rainfall data, can be also used to evaluate the antecedent soil moisture condition. In hydrological modeling, antecedent moisture condition is usually associated with the pre-storm soil moisture deficit. This latter has a significant effect on the amount of rainfall drained by the river network and finally on the flooding potential of a rainstorm.

2.2 Climate-Change projection rainfall data

As mentioned in the introduction, there is increasing evidence in the favor of a correlation between the climate change and extreme weather-related phenomena [1]. In particular, the future climate patterns may manifest adverse effects on the frequency and/or intensity of extreme weather-related events such as floods.

In compliance with the Intergovernmental Panel on Climate Change (IPCC) scenarios [2], climate projections are evaluated using the General Circulation Model (GCM). A GCM is a mathematical model that simulates the general atmospheric and oceanic circulation over long periods of time using a specific formulation of the Navier-Stokes equation, discretized with spatial resolutions in the order of 100x100 km.

As depicted in Figure 2., GCM is based on a rotating sphere whose key components are atmospheric (lands, mountains and atmosphere) and oceanic (oceans) GCMs. The energy sources (radiation, heat, etc.) of the sphere are expressed through thermodynamical equations. The mathematical models work using as lattice the grid-boxes depicted in Figure 2.1.

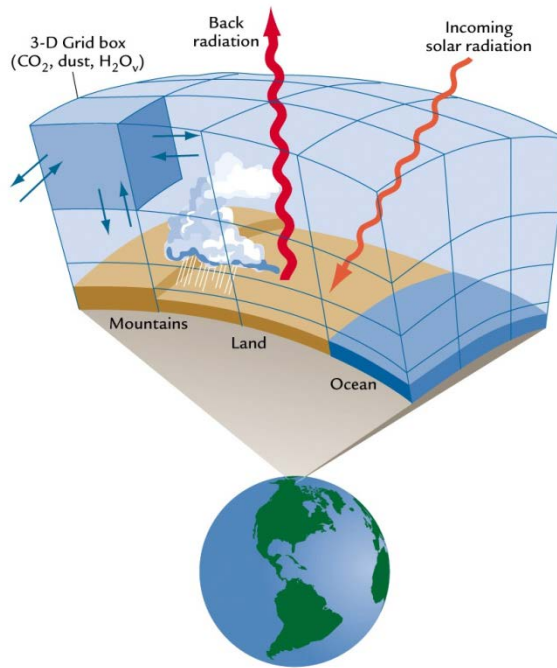


Figure 2.1 - The Global Circulation model [3]

Ideally, GCMs can be used to produce long-term simulations for catastrophe modeling. However, for a realistic simulation of precipitation patterns, representing the vertical structure of the atmosphere as well as the effect of the terrain on atmospheric circulation, a model must have a resolution less than 100 km. This is not practical since the calculation time increases exponentially. Therefore, using a GCM for direct simulation of precipitations is not feasible. Moreover, the GCMs are based on simplified microphysics and may not provide a solid representation of precipitation in the mountainous areas [4].

On the other hand, the application of a Regional Climate Model (RCM) with horizontal spatial resolution of 10x10 km can be useful for the description of the climate variability in the local scale. However, a RCM depends on the definition of boundary conditions that can be obtained based on the results of a GCM.

Finally, through statistical downscaling it is possible to obtain

climatological data for finer spatial resolutions, in the order of 1x1 km. This provides the precipitation data necessary for comprehensive flood modeling.

2.2.1. *Climate projections used in this work*

The climate projections used in this thesis are provided by the CMCC (*Centro Euro-Mediterraneo sui Cambiamenti Climatici*). They have been obtained by following the IPCC 20C3M protocol for the 20th Century, using RCP4.5 and RCP8.5 radiative forcing scenarios developed in the framework of the 5th Coupled Model Intercomparison project [5].

The initial conditions have been obtained from an equilibrium state reached by integrating the model for 200 years with constant greenhouse gas (GHG) concentrations corresponding to 1950's. Once the climate model reaches equilibrium with the prescribed constant radiative forcing (GHG and aerosol concentrations), the simulations have been conducted by increasing the GHG and aerosol concentrations in line with observed data.

CMCC has performed a set of climate simulations over the time period 1950-2050 (spatial resolution 80 km) in the context of the FP7 project CLUVA (Climate Change and Urban Vulnerability in Africa).

These simulations have been downscaled to a spatial resolution of 8 km, based on a non-hydrostatic RCM, developed considering the spatial extent covered by the urban area of interest. The results were further downscaled to a spatial resolution of 1 km in order to render them suitable for modeling of precipitation patterns.

In this work, the climate projections based on the RCP8.5 scenario and down-scaled to 1km resolution are taken into account. This may be considered a worst-case scenario in terms of gas emissions and temperature increase.

2.3 Geo-morphologic datasets

Geo-morphologic spatial datasets (e.g., topographic maps, geology maps, land-use, ..., etc.) are fundamental data requirements in various stages of flood risk assessment. These datasets are described in more detail below.

2.3.1. Topography: The Digital Elevation Model

Topography plays an important role in flood modeling. It is demonstrated that there exists a correlation in macro-scale between the terrain elevation and the annual accumulated rainfall [6]. Moreover, topography plays a key role in the surface runoff and catchment response time (i.e. the time between the peak rainfall and the peak flow discharge). Steeper catchments have higher runoff coefficients and response time. In addition, mountain rivers flow much more quickly with respect to rivers in lowlands.

The typical instrument used to describe the topography of a generic hydrological domain is the Digitalized Elevation Model (*DEM*), that is a 3D digital representation of terrain's surface. A typical *DEM* representation is shown in Figure 2.2 for the city of Addis Ababa, Ethiopia.

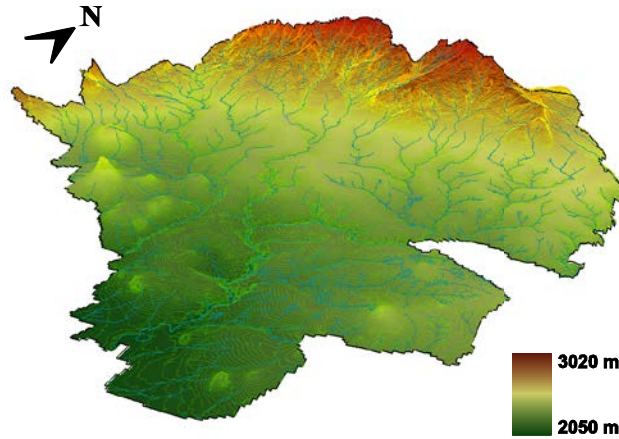


Figure 2.2- DEM of Addis Ababa (overlaid with the main water courses)

The DEM is used in this work for two specific purposes: a) evaluation of a meso-scale hazard indicator (Topographic Wetness Index); and b) flood diffusion/propagation by employing a classical hydraulic routine.

2.3.2. Geological dataset

The geological dataset is generally presented as a geologic map, that is a special-purpose map through which it is possible to show the soil's geological

features.

The underlying geology and the dominant soil type of a catchment area are important factors in determining the quantity and proportion of the surface run-off. The infiltration capacity of the soil depends on both the soil type (e.g., its grain size distribution and porosity) and also the characteristics of the underlying water-bearing rock layers (e.g., porosity and thickness) --known as "groundwater aquifers." Large groundwater aquifers act as large reservoirs in that they release --over long periods of time-- the infiltrated water after a storm. In this manner, they mitigate eventual river over-flow problems.

Igneous rocks produced from lava or magma from earth's lower crust (e.g., basalt and granite) have very low infiltration capacity unless they are heavily fractured. On the other hand, chalk and limestone, have high infiltration capacity to the extent that prevents rivers from forming. Sandstone and shale are the analogs of sand and clay consolidated to rocks over millions of years through the so-called process of lithification. Their infiltration capacity is usually low unless they are heavily fractured by subsequent geologic processes.

The best way to quantify the effect of soil type and stratification on the quantity of surface run-off is by means of the *runoff coefficient* (described in Chapter 3), that expresses the proportion of total rainfall that is drained by the river network. This coefficient reflects the numerous possible combinations of soil types and the underlying geology.

Generally the geological datasets are represented in form of GIS-based shape files or raster files with variable scale --between 1:1000 to 1:100000. In order to gain knowledge about subsoil stratigraphy, appropriate *geological sections* can be defined inside a geological spatial dataset.

2.3.3. *Land use maps*

The runoff coefficient, the catchment discharge, and the catchment response time all depend on the land cover. In forest areas, tree roots increase the infiltration of water by channeling it deeply inside the soil layers down to the ground water. This effect is less pronounced in areas covered by shrubs

and in pastures where the roots are much shallower.

In urbanized areas, and in particular in large cities, the large percentage of paved areas may increase the runoff coefficient significantly. This is because smooth surfaces like asphalt and concrete generally have very low infiltration capacity. This leads to larger flood discharge and lower response time in urban areas.

The land-use geo-spatial datasets can be found in GIS-based formats such as shape files and raster files. These land-use datasets/maps efficiently store the land cover type (e.g., green area, stone-paved, ..., etc.) for the spatial units considered. The resolution of the land-use maps may vary between 1:1000 to 1:100000.

2.4 Orthophotos and their by-products

Photos of the terrain taken with special camera from an airplane are generally called *aerial photos*. Generally, these kind of photos are taken in a sequential manner with a constant time interval, so as to achieve a strip of photos. The *orthophotos* are obtained by assembling the photos strips together and removing the topographic and geometric distortion by means of an orthorectification instrument. The orthophotos, the same as the other geo-spatial datasets, can be geo-referred in one of the many possible reference systems.

Orthophotos are very useful means for remote planimetric data acquisition. In this thesis, orthophotos are employed in two alternative ways: a) (directly) for the micro-scale recognition of the buildings boundaries; and b) (indirectly) through the urban morphology types (described hereafter).

2.4.1. *Micro-Scale boundary recognition*

In this work, boundary-recognition based on recent orthophotos of the zone of study is employed in order to determine the plan dimensions of the buildings. As depicted in Figure 2.3, this helps in obtaining the buildings' dimensions in the zone of interest.

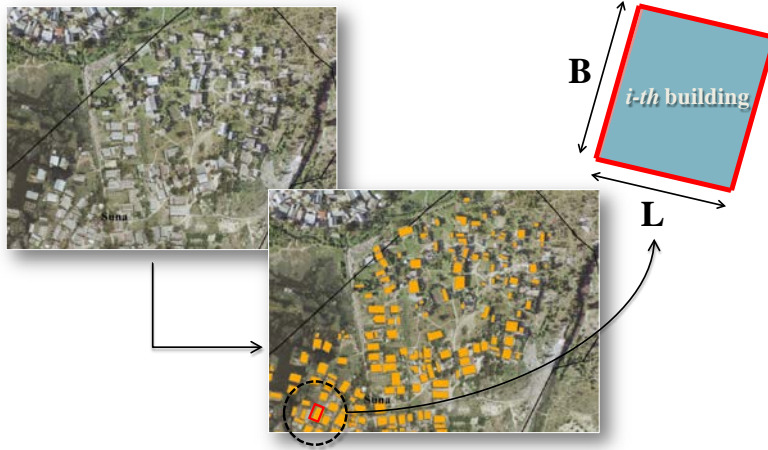


Figure 2.3 - Boundary recognition based on the orthophotos

As it will be demonstrated later, this boundary-recognition procedure is useful for obtaining information both for structural modeling and also for the estimation of the exposure (e.g., expected number of inhabitants, expected repair costs).

2.4.2. UMT: Uniform Morphology Types

Urban Morphology Types (UMTs) [7] form the foundation of a classification scheme which brings together facets of urban form and function. The UMT's are used to develop a geo-spatial dataset containing seamless polygons of UMT units. Each unit is associated with attribute information describing its class and its geometric properties. This geospatial layer provides complete and consistent coverage across the city having used an internally consistent process for unit delineation, data recording and coding. Linear features such as roads and rivers are usually used as the outline of UMT units, and they are matched with administrative units/zones whenever possible, e.g. for the boundary of the dataset, as shown in Figure 2.4 .

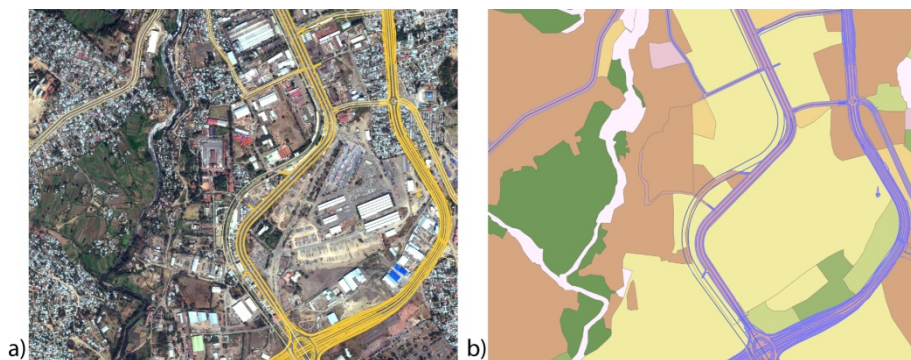


Figure 2.4 - Mapping UMT units (b) using ortho-rectified aerial photography (source www.bing.it/maps) (a), an example in Addis Ababa.

In order to build a UMT map, it is necessary to identify the various UMT classes for the specific urban area (e.g., farmland, transport, residential, etc.). The UMT classification is then subjected to a verification process in order to establish its suitability for the case-study area. The UMT classes can be detected through visual analysis of remote sensing data (ortho-rectified aerial photography) as primary method of applying the scheme [7, 8]. Furthermore, for each UMT class, typical images can be captured and kept for reference with a description of its characteristics. Finally, the dataset is going to undergo field verification and approval. Once a complete UMT layer has been created through the process of digitization, it can be combined with other datasets to produce spatial indicators.

2.5 Census information

Geo-spatial data-sets having Census information are fundamental sources of information for the estimation of exposure. These datasets can be used to obtain demographic information such as population density.

For example, the data used for estimating the exposure for Addis Ababa in Chapter 4 are obtained from the Central Statistical Authority of Ethiopia, and are related to the population census made in 2007. For Dar es Salaam, the data are related to the population census made in 2007 realized by National

Bureau of Statistics of the Ministry of Planning Economy and Empowerment.

2.6 Field survey

Field surveys are useful means of laying out the spatial variation in building geometry and structural detailing within a class of buildings. Appendix A demonstrates the sample field survey form developed in this work for mapping out detailed geometrical configuration and construction details for the buildings. The building characteristics deemed particularly relevant for flooding vulnerability analysis are: wall thickness, height of the building, presence of barriers in front of the door, presence of raised foundation, quality of doors and windows (water-tight or not), dimension of and configuration of doors and windows, height of the barrier, and height of the raised foundation. As it will be described in the next chapters, this work relies on a relatively small number of building surveys as opposed to exhaustive surveying of all the buildings in the zone of interest.

2.7 Material properties

Ideally, structural material properties should be obtained based on the results of specific laboratory tests. The laboratory tests mimic the construction materials and relevant techniques used in the field in order to evaluate material mechanical properties such as, the elastic modulus (E), the Poisson ratio (ν), the compression strength (f_m), the shear strength (τ), and the out of plane flexural strength ($f_{\bar{f}}$). The laboratory tests can also be used to gain an estimate of deterioration due to elongated contact with water. In this work, existing literature results are used in lieu of case-specific laboratory tests. In particular, existing literature results are used to obtain the above-mentioned material properties for panels made up of sand and cement brick for studying the informal settlements constructed with cement-stabilized bricks in Dar es Salaam.

References

1. Khan S. and Kelman I., *Progressive climate change and disasters: connections and metrics*. Natural Hazards, 2011. **61**: p. 1477-1481.
2. Alley R., Berntsen T., Bindoff N.L., Chen Z., Chidthaisong A., Friedlingstein P., Gregory J., Hegerl G., Heimann M., and Hewitson B., *IPCC 2007: summary for policymakers*. Climate Change, 2007: p. 1-18.
3. Ruddiman W.F., *Earth's Climate: Past and Future*. 2001, New York.
4. Bellucci A., Bucchignani E., Gualdi S., Mercogliano P., Montesarchio M., and Scoccimarro E., *Data for global climate simulations available for downscaling, deliverable D1.1 in CLUVA project - Climate Change and Urban Vulnerability in Africa*. 2012. Available from: http://www.cluva.eu/deliverables/CLUVA_D1.1.pdf. Data last access: 01/01/2013.
5. WCRP, World, Climate, Research, and Programme. *CMIP5 Coupled Model Intercomparison Project*. 2008; Available from: <http://cmip-pcmdi.llnl.gov/cmip5/>.
6. Allamano P., Claps P., Laio F., and Thea C., *A data-based assessment of the dependence of short-duration precipitation on elevation*. Physics and Chemistry of the Earth, 2009. **34**: p. 635-641.
7. Pauleit S. and Duhme F., *Assessing the environmental performance of land cover types for urban planning*. Landscape and Urban Planning, 2000. **52**: p. 1-20.
8. Gill S.E., Handley J.F., Ennos A.R., Pauleit S., Theuray N., and Lindley S.J., *Characterising the urban environment of UK cities and towns: A template for landscape planning*. Landscape and Urban Planning, 2008. **87**: p. 210-222.

Chapter 3

MICRO-SCALE FLOOD HAZARD ASSESSMENT

In this chapter, the methodology employed to assess the flood hazard at micro scale level is described in detail.

3.1 The rainfall curve

This work employs rainfall scenarios for various return periods, also known as the rainfall curves or the Intensity-Duration-Frequency (IDF) curves. The rainfall curves are normally used, in lieu of sufficient data for direct probabilistic discharge modeling, in order to evaluate the peak discharge. In particular the IDF curve presents the probability of a given rainfall intensity and duration expected to occur at particular location.

IDF curve, is a tool that characterizes an area's rainfall pattern. By analyzing past and projected rainfall events, statistics of rainfall extremes recurrence can be determined for various return periods (T_R) (e.g., 2, 10, 30, 50, 100 and 300-yr). The annual extremes are usually obtained as maximum rainfall over a time-series --spanning over the whole year-- of extreme rainfall height values (in mm) calculated over time window duration d . The rainfall curve, corresponding to a specific return period, is calculated by fitting a suitable probability model to the extreme rainfall data. The IDF curves can be characterized by two or three parameters, as shown in the following expressions:

$$h_r(d, T_R) = a(T_R) \cdot d^n \quad (3.1)$$

$$h_r(d, T_R) = \frac{a(T_R) \cdot d}{(b + d)^c} \quad (3.2)$$

in which T_R is the return period and $a(T_R)$, b , c and n are the parameters that have to be estimated through a probabilistic approach. In the present study, the power-law curves expressed in (3.1) have been used. Herein, a Gumbel probability distribution (belonging to the GEV family of distributions) has been employed, considering only the extreme events on a block fixed window [1] to fit the extreme rainfall data:

$$P(h_r) = \exp\left\{-\exp\left[-(h_r - \mu) \setminus \sigma\right]\right\} \quad (3.3)$$

where $P(h_r)$ is cumulative distribution function (CDF) for h_r . The two parameters v and u are related to the real mean (μ) and to the real standard deviation (σ) through the following equations:

$$\sigma = \frac{u}{1.28} \quad (3.4)$$

$$\mu = v - 0.577 \cdot \sigma = v - 0.45 \cdot u \quad (3.5)$$

The inverse of CDF (3.3) can be calculated by calculating h_r in terms of $P(h_r)$ and duration d :

$$h_r(d, P) = \mu - \sigma \cdot \ln\left[-\ln(P)\right] \quad (3.6)$$

where $h_r(d, P)$ denotes the maximum annual flooding height calculated over a time window of duration d and exceeded with probability $1-P$. Substituting (3.4) and (3.5), and introducing the variation coefficient CV equal to u/v :

$$h_r(d, P) = v(d) \cdot \left\{1 - CV(d) \cdot \left[0.45 + \frac{1}{1.28} \cdot \ln\left[-\ln(P)\right]\right]\right\} \quad (3.7)$$

Since the probability P is related to the return period T_R , through $1-p=1/T_R^1$, h_r can also be expressed in terms of the return period:

$$h_r(d, T_R) = v(d) \cdot \left[1 + CV(d) \cdot K\right] \quad (3.8)$$

¹ This is an approximate relationship in which a rate is made equal to a probability value. This relationship is almost exact for small probability of exceedance (rate) events.

where

$$K = - \left\{ 0.45 + \frac{1}{1.28} \cdot \ln \left[-\ln \left(1 - \frac{1}{T_R} \right) \right] \right\} \quad (3.9)$$

where $h_r(d, T_R)$ denotes the maximum annual flooding height calculated over a time window of duration d and exceeded with frequency $1/T_R$. The experimental evidence also shows that extreme precipitations have a physical property, known as scale invariance or *self-similarity*, so that the following relation holds:

$$h_r(T_R, sf \cdot d) / h_r(T_R, d) = (sf)^n \quad (3.10)$$

in which sf is a scale factor and n is a parameter function of the location. This scale invariance implies the statistical self-similarity between the probability distribution of $h_r(d)$ and $h_r(sf \cdot d)$. As a result of the statistical self-similarity, $v(d) = a_\mu \cdot d^n$, in which $v(d)$ is the parameter of Gumbel distribution. Substituting the expression for $v(d)$ in Eq. (3.8) one obtains the flood height as function of duration d and return period T_R :

$$h_r(d, T_R) = a_\mu \cdot d^n \cdot (1 + CV_m \cdot K_T) \quad (3.11)$$

Taking into account the general expression (3.1), the above equation can be written as:

$$h_r(d, T_R) = a(T_R) \cdot d^n$$

Where $a(T_R)$ can be calculated as: (3.12)

$$a(T_R) = a_\mu \cdot K_{T_R}$$

where $K_{T_R} = (1 + CV_m \cdot K)$. K_{T_R} is generally known as the *growing factor* (as a function of T_R). CV_m denotes the mean CV over different durations d . Assuming that the coefficient of variation is quasi-invariable as a function of duration d , its mean value for the coefficient of variation denoted as CV_m can be evaluated by the following expression:

$$CV_m = \frac{1}{k} \cdot \sum_{i=1}^k CV_i \quad (3.13)$$

in which k is the considered duration --taken equal to 5 in this work (i.e., refers to $d=1, 3, 6, 12$, and 24 hours).

3.1.1. The rainfall curve based on incomplete historical event

The maximum annual rainfall data calculated for a specific time window are not always available. In many cases (including the cases studied in this work), annual maxima are calculated over a 24 hour time window.

In such cases, the annual (24hr) maximum rainfall is synthetically simulated for the missing (smaller) time-window durations. This involves generating synthetic sequences of rainfall for smaller time windows (e.g., 10', 30', 1h, 3h, 6h, 12h), with statistical properties equal to that of the observed daily rainfall. In this work, two alternative temporal downscaling techniques are used in order to generate maximum rainfall values for the desired time windows. The short-time intensity disaggregation method [2] has been used for simulation of smaller time windows (i.e., 10', 30', 1h) and the random cascade-based disaggregation method [3, 4] has been used for larger time windows (i.e., 3h, 6h and 12h).

3.1.2. Historical Data vs Climate Projections

The IDF curves in this work are obtained based on: (a) historical pluviometric data; (b) downscaled results of a climate projection scenario (i.e., RCP8.5). In the first case, it is assumed that the historical climate trends are going to be valid also for future predictions. Meanwhile, in the second case, scenario-based climate projections are used to predict the future climate trends.

3.2 Hydrographic basin model

The hydrograph curve is the discharge (volume/time) plotted versus time. A schematic diagram of the procedure used for hydrographic basin modeling is illustrated in Figure 3.. As it can be observed, IDF curves, geologic and land-use information are used to characterize the hydrograph leading to the calculation of the discharge denoted by Q and the total water volume for different return periods (i.e., the area under the hydrograph). This information,

together with the topographic map of the zone of interest are used in a two-dimensional diffusion model in order to generate the maps of maximum water height and velocity for each node of a lattice covering the zone of interest for a given return period (the flood hazard map). This procedure is described in more detail in the following.

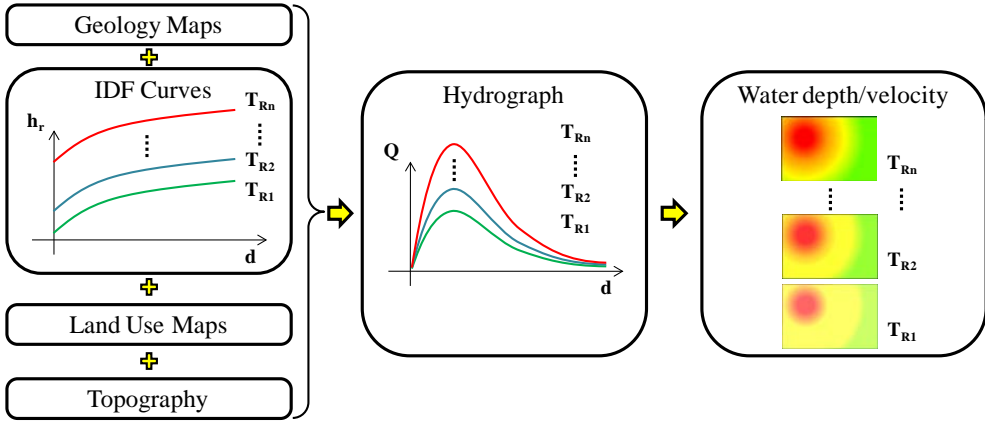


Figure 3.1 - Hydrographic basin modeling procedure

3.2.1. Catchment area definition

Catchment area characterization, which is done based on the topography of the zone, is one of the very first steps in hydrographic basin analysis. The catchment refers to the topographical area from which a watercourse, or a water course section, receives surface water from rainfall (and/or melting snow or ice).

3.2.2. Hydrograph building

Once the rainfall curve or the IDF curve has been characterized, a rainfall-runoff method must be applied in order to evaluate the hydrograph. The hydrograph refers to the flow discharge in the closure section of the catchment as a function of time and constitutes the input for the hydraulic diffusion model (Figure 3.2). The area under the hydrograph is equal to the total discharge volume for the basin under study. For drainage-type

catchments --where water runoff cannot be directly measured-- the classic Curve Number Method (CNM) [5] seems to be suitable for modeling the hydrograph. The Curve Number (CN) value depends (among other factors) on the antecedent soil moisture condition (AMC) in the drainage catchment. In particular, there are three classes of AMC, namely, AMC I: the soils in the catchment are practically dry; AMC II: Average condition; AMC III: the soils in the catchment are practically saturated from previous rainfalls). In this study a CNII class corresponding to the average condition (AMCII) has been considered.

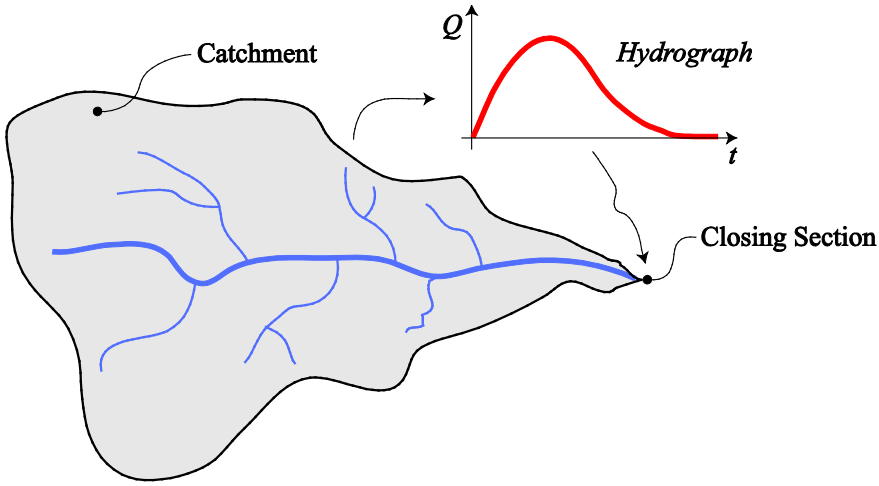


Figure3.2 - The schematic diagram of a hydrographic basin

In the framework of the CNM, the characteristics of the discharge hydrograph is evaluated using a unit Mockus [5] hydrograph depicting the discharge Q as a function of time. In particular for the evaluation of the hydrograph peak time t_p (in hours) the following formula is considered:

$$t_p = 0.5 \cdot D + t_l \quad (3.14)$$

where:

- D is the rainfall duration (in hours, equal to the concentration time evaluated from Viparelli formula [6])

- t_l is the catchment lag time (in hours), i.e. the time between the hydrograph centroid and the net rainfall centroid, equal to:

$$t_l = 0.342 \cdot \frac{L^{0.8}}{s^{0.5}} \cdot \left(\frac{100}{CN} - 9 \right)^{0.7} \quad (3.15)$$

in which L is the length of the main channel (in kilometers) and s is the mean slope (as percentage). It can be noted that t_p measures the response time of the catchment; that is, time elapsing from the beginning of rainfall to the maximum discharge in the basin closing section.

3.2.3. Two-dimensional propagation model

The characterization of the discharge hydrograph forms the basis for the identification of flood prone areas. In the next step, the flood discharge estimated by the hydrograph needs to be propagated through the zone of interest in order to delineate the flood prone areas for various return periods. In this work, flood routing in two dimensions is accomplished through the numerical integration of the equations of motion and continuity (dynamic wave momentum equation) for the flow. This has been accomplished by means of the commercial software FLO-2D ([7, 8]) which is a flood volume conservation model based on general constitutive fluid equations of continuity and flood dynamics. Such two-dimensional flood simulation is based on a digital elevation model (DEM) overlaid with the surface grid, aerial photography and orthographic photos, detailed topographic maps and digitized mapping. Such a detailed cartography is needed in order to identify the surface attributes of the grid system; for example, streets, buildings, bridges, culverts or other flood routing or storage structures. The principal advantages in using a two-dimensional diffusion model is that it can be applied in special cases such as, unconfined or tributary flow, very flat topography and split flow.

3.3 Flood hazard curves

The two-dimensional flood routing for a given surface grid in the flood

prone area, provides the values of maximum water height and velocity for all the nodes within a lattice covering the zone of interest, for a given return period. These results, referred to as the *inundation profiles*, can be visualized as the maximum flood height/velocity maps for a range of return periods. Alternatively, it is possible to represent the results in terms of the flood hazard curves depicting the mean annual rate (or annual probability) of exceeding various flood heights/velocities for each node within the zone. In particular, the flood hazard curves for water height are denoted by $\lambda(h_f)$ that is the mean annual rate of exceedance (equal to the inverse of return period for a homogeneous Poisson process) of a given maximum flooding height h_f at a given point in the considered area (e.g., centroid of a given building).

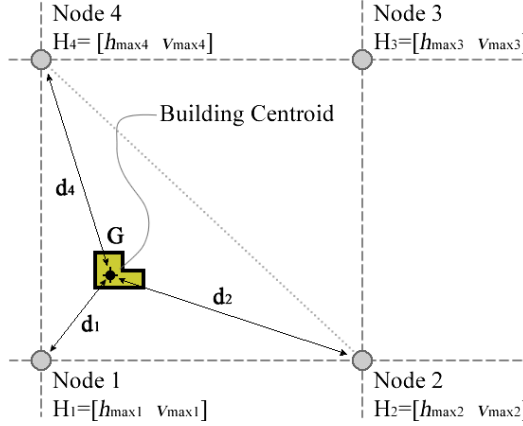


Figure 3.3 - Graphical representation of the spatial interpolation for point G

The hazard curves for a point within the zone of interest (identified as G in Figure 3.3) are extracted from the inundation profiles by performing a spatial interpolation between the flood height/velocity values at the nearby vertices (nodes) of the lattice grid containing the point in question. The flooding height and velocity vector denoted by $\mathbf{H}=[h_{max}, v_{max}]$ at a given point can be evaluated as follows:

$$H_G = \frac{\frac{H_1}{d_1} + \frac{H_2}{d_2} + \frac{H_4}{d_4}}{\frac{1}{d_1} + \frac{1}{d_2} + \frac{1}{d_4}} \quad (3.16)$$

where d_i denotes the distance to node i and H_i represents the flooding height and velocity vector for node i respectively. It can be observed in Eq. (3.16), that the flood height and velocity vector H_G is calculated as the spatial weighted average of H_i ; where the weights are equal to the inverse of the distance d_i . It is worth noting only the three closet nodes are taken into account in this spatial interpolation.

3.4 Flood height as an intermediate variable

In this work, the flood height has been used as the intermediate variable (i.e., a measure of the intensity of the flood) linking the hydrographic basin analysis and flooding vulnerability assessment of the portfolio of buildings (see the following sections). It should be noted that one could have also used the vector consisting of the maximum flood height and flood velocity pair as a link between flooding hazard and structural vulnerability. However, for the sake of tractability of calculations, it has been chosen to use the flooding height as the only interface variable. The flooding velocity for each point in the grid is then calculated from a power-law relation as a function of the flooding height. This power-law relation is characterized for each node within the lattice separately based on the results of flood propagation for the velocity/height pairs for various return periods. In particular, an analytical power-law relation of the form $h_{\max} = a \cdot v_{\max}^b$ is fitted by employing a linear regression in logarithmic scale to $\mathbf{H}=[h_{\max}, v_{\max}]$ pairs, for all the return periods considered. Figure 3.4 below demonstrates 3 different power-low fits performed for three different points within a given case-study area (Suna, Dar es Salaam City).

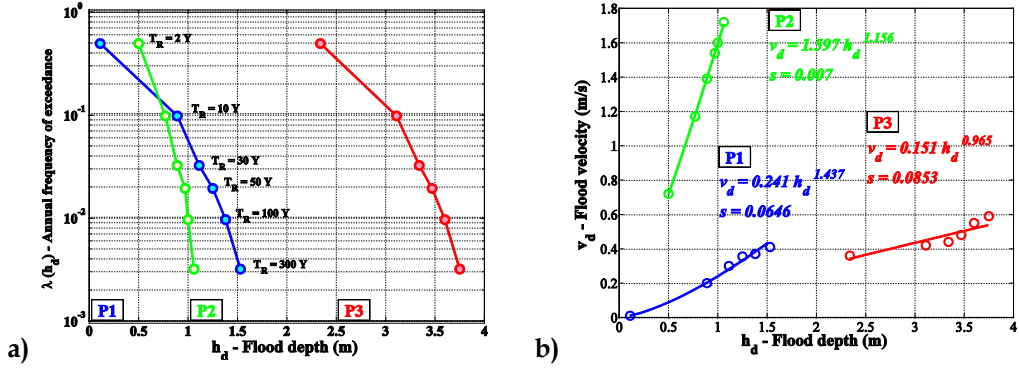


Figure 3.4 - a) Hazard curves, b) Flood height versus flood velocity power-law relation

It is worth re-emphasizing that this power-law fit helps in transforming an otherwise vector-based risk assessment using $\mathbf{H}=[h_{max}, v_{max}]$ as the hazard/fragility interface variable to a scalar risk assessment problem using only h_{max} as the interface variable.

3.5 The case of Suna, Dar es Salaam

As the case-study zone for micro-scale flood risk assessment in Dar es Salaam, the Suna subward (Figure 3.5) in the Kinondoni District has been chosen. Suna, located on the western bank of the Msimbazi river with an extension of about 50 ha, is a historically flood-prone area. The Msimbazi river flows across Dar es Salaam City from the higher areas of Kisarawe in the Coastal region and discharges into the Indian Ocean.

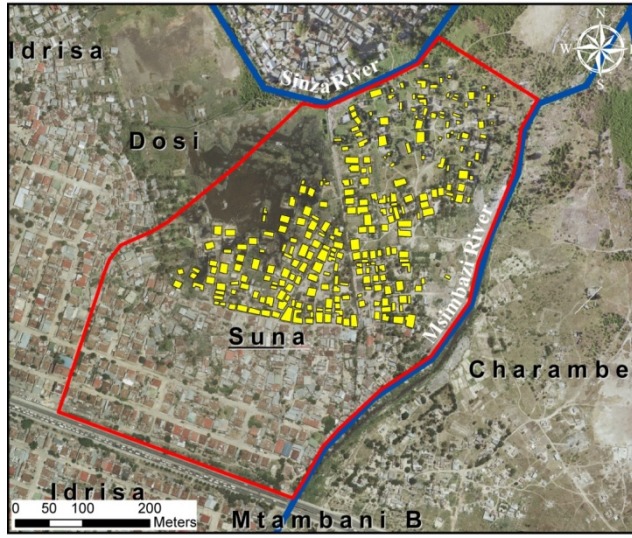


Figure 3.5 - The case study area and the portfolio of the buildings studied.

3.5.1. The IDF Curve: Historical Data and Climate Projections

As mentioned in Section 3.1.2, the rain-fall curve is calculated based on both historical data and a specific climate projection scenario. The historical rainfall data span from 1958 to 2010 and the climate projection is provided up to 2050.

The historical rainfall data is obtained from a single meteorological station located in the DSM International Airport at 55 meter altitude from the sea level, 6°86' latitude and 39°20' longitude. Based on these recordings, the mean annual rainfall for DSM city is estimated at around 1110 mm. The IDF curve is obtained by following the procedure outlined in Section 3.1 and is characterized by the following relationship:

$$h_r(d, T_R) = K_{T_R} \cdot 36.44 \cdot d^{0.25} \quad (3.17)$$

The values of the growing factor K_{T_R} as a function of the return period T_R are: $K_2=0.95$, $K_{10}=1.42$, $K_{30}=1.70$, $K_{50}=1.83$, $K_{100}=2.01$, $K_{300}=2.29$.

The projected IDF curve is obtained through the same procedure, based on the climate change projection for scenario RCP8.5 (which is a worst-case scenario reflecting increased emissions of greenhouses gasses in the

atmosphere) with a spatial resolution of 80Km, spatially downscaled to a spatial resolution of 8 Km, and subsequently stochastically downscaled to 1 km resolution. It is characterized by the following relationship:

$$h_r(d, T_R) = K_{T_R} \cdot 31.70 \cdot d^{0.26} \quad (3.18)$$

The corresponding values of the growing factor K_{T_R} are: $K_2=0.94$, $K_{10}=1.50$, $K_{30}=1.84$, $K_{50}=2.00$, $K_{100}=2.21$, $K_{300}=2.41$.

T_R	2 Ys	10 Ys	30 Ys	50 Ys	100 Ys	300 Ys
H	0.95	1.42	1.70	1.83	2.01	2.29
CC	0.94	1.50	1.84	2.00	2.21	2.41

Table 3.1 - Growing factors for the different return periods (H:historical, CC: climate change)

The rainfall curves with and without climate change effects and classified by 6 different return periods are plotted in Figure 3.6. It is possible to observe that for DSM city the particular climate scenario considered leads to a decrease in terms of rainfall intensity. In fact, the IDF curves that take into account the climate projection (the dotted lines in Figure 3.6) are lower than those evaluated based on historical data series (the solid line in Figure 3.6). It can be observed that, although the flooding intensity considering the projections decreases with respect to the historical data, the growing factor demonstrates a slight increase, given the return period. Since the growing factor is a function of the coefficient of variation for the extreme value distribution (see Section 3.1), having a higher coefficient of variation (with constant mean or central value) leads to higher probability for extreme rainfall events (i.e., in the tail of the distribution).

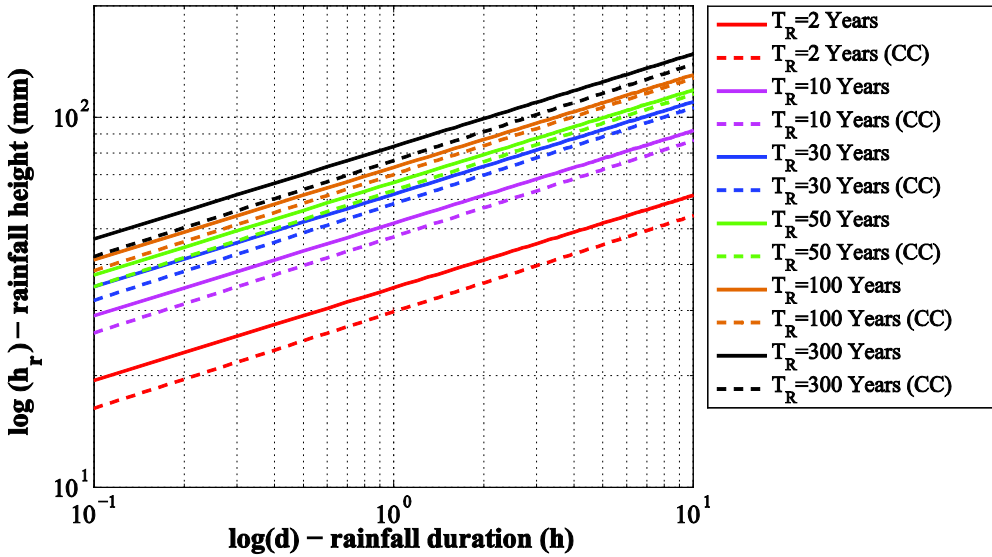


Figure 3.6 - Rainfall Probability Curves for Dar es Salaam with and without climate change (CC) effects.

3.5.2. The definition of the catchment area

The first step in the delineation of inundated areas in the Suna district was the definition of the catchments of the Msimbazi river and its main tributaries. Three different catchments (of about 250 km²) were identified as shown in Figure 3.7.

The characteristics of the three catchments identified are reported in Table 3.2. The land-use and geological maps are illustrated in Figure 3.8 (a) and Figure 3.8 (b), respectively. From the geological point of view, the catchments are characterized mainly by clay-band sands and gravels (corresponding to soil group B in the Curve Number method). With reference to the land use, catchment 1 and 2 are characterized mainly by agricultural use and catchment 3 is characterized as residential area.

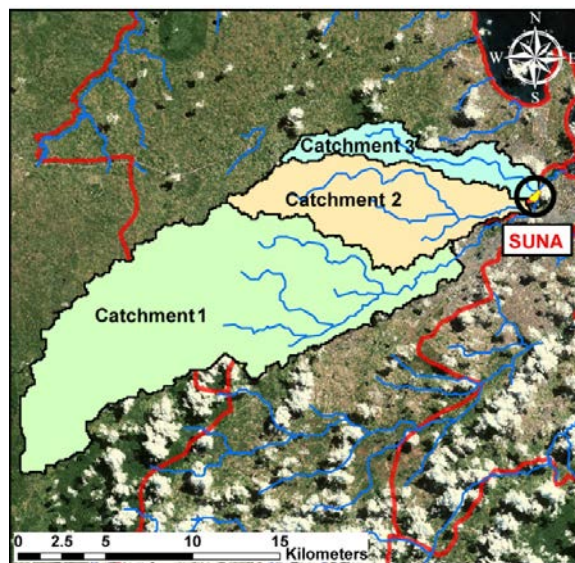


Figure 3.7 - Visualization of the Mzimba catchments with the position of the case-study area

Characteristics	Mzimba River		
	Catchment 1	Catchment 2	Catchment 3
Drainage area (km ²)	166.3	60.5	24.1
Main channel length (km)	32.7	18.2	14.9
Average slope (%)	5.8	4.2	3.9
Average height (m.a.s.l.)	175.5	108.6	97.2
CNII	64.73	77.98	89.91
t_p (h)	13.03	6.90	4.63

Table 3.2 - The characteristics of the Mzimba River catchments

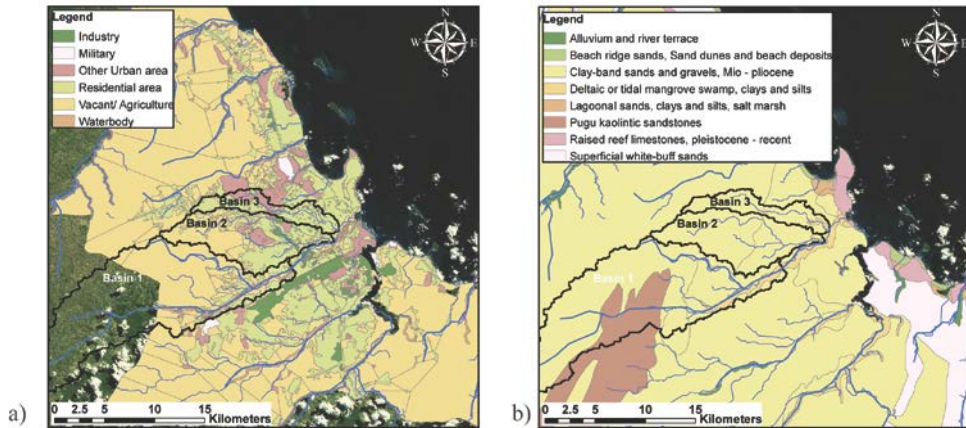


Figure 3.8 - Mzimba River catchments: a) Land use, b) Geology

3.5.3. The characterization of the hydrographs

The peak flow of the three catchments was evaluated by the Curve Number method, with reference to six different return periods (e.g., 2, 10, 30, 50, 100 and 300-yr) based on both historical data and climate projections. The inflow hydrographs for catchment 1, corresponding to the various return periods considered, are illustrated in Figure 3.9.

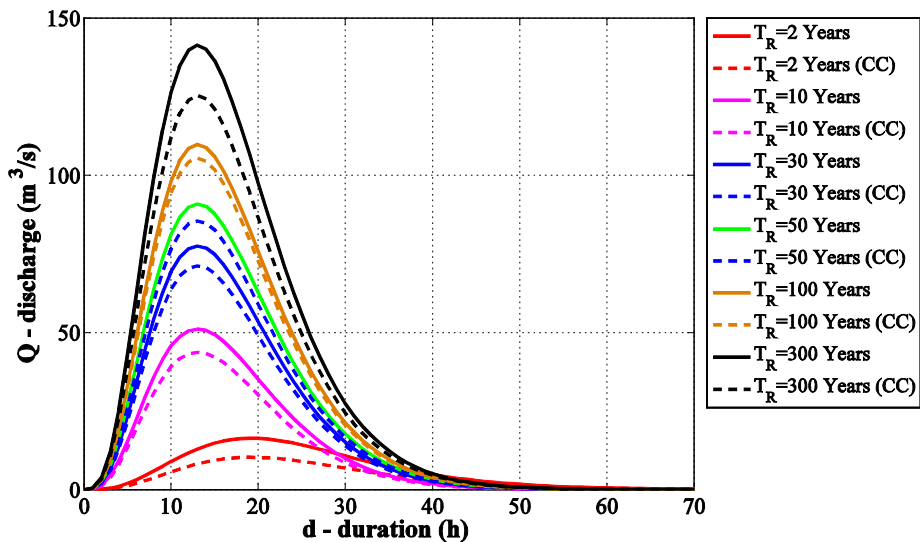


Figure 3.9 - Hydrographs evaluated for catchment 1 ($T_R = 2, 10, 30, 50, 100$ and 300 years) with and without CC effects

It is possible to observe that the hydrographs obtained with the effects induced by the climate change (the dotted lines in Figure 3.9) are lower than the hydrographs obtained with the historical data (the solid line in Figure 3.9). This results are coherent with the IDF curves shown in Figure 3.6.

3.5.4. *The micro-scale flood hazard*

The software FLO-2D was used for a bi-dimensional simulation of the flooding volume propagation (based on the calculated hydrographs and a digital elevation model, DEM) assuming a 45 hour simulation time (i.e., the total duration of the hydrograph). The outcome of the flood propagation considering the historical data (referred to hereafter also as the *inundation profiles*) is illustrated in Figure 3.12 and Figure 3.13, in terms of maximum flow depth h_{max} (in meters) and velocity v_{max} (in meters per second), with reference to the six considered return periods. It should be noted that the inundation profiles calculated based on the climate projections are not shown herein².

Moreover, the flood hazard curves, plotting the mean annual rate of exceeding various flooding heights (i.e., inverse of the return period) are illustrated in Figure 3.10 (a) and Figure 3.10 (b), for historical data and for the climate change projections³, respectively. Each grey curve maps to the centroid of a building belonging to the portfolio of the buildings considered.

² For the sake of brevity and also because they are quite similar to those based on historical data

³ It should be mentioned that the rainfall annual extremes time series used for climate projections spans from 1959 to 2050. This means that the data used for years 1959-2010 are based on historical data and the data used for years 2010-2050 is projected. This is a common practice ensuring consistency between recorded and projected data.

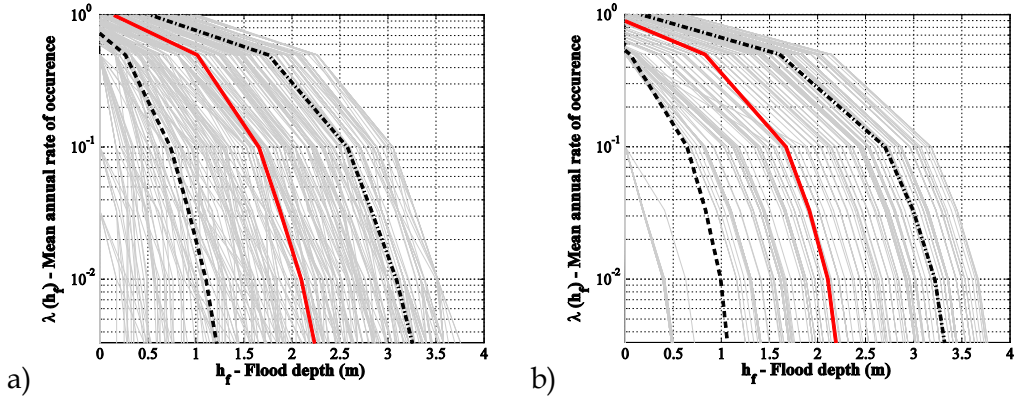


Figure 3.10 - The hazard curves a) considering the historical data and b) considering the climate projections

The red and the black curves are the mean, and the mean plus/minus one standard deviation curves, respectively. These three curves represent the statistics of the hazard curves calculated for various points of interest (e.g., centroid of a building) within the case-study area. Overlaying the three curves relative to the historical data and those relative to the climate change projections in Figure 3.11, it is possible to observe that the (statistics of the) hazard values obtained based on the historical data are larger with respect to those obtained considering the climate projections.

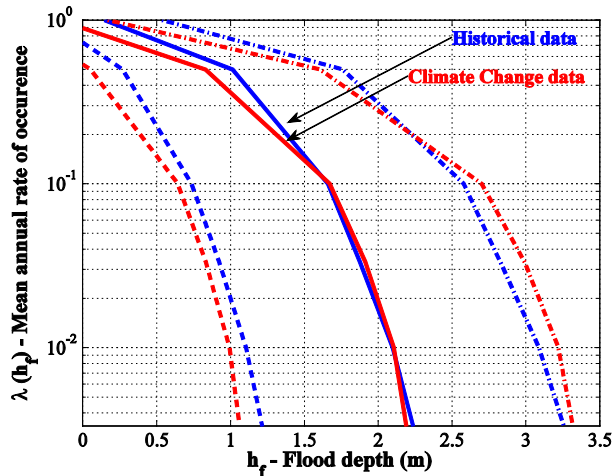


Figure 3.11 - Overlaying of the representative (mean and mean +/- standard deviation) hazard curves obtained based on, historical data (the blue curves) and climate projections (red curves)

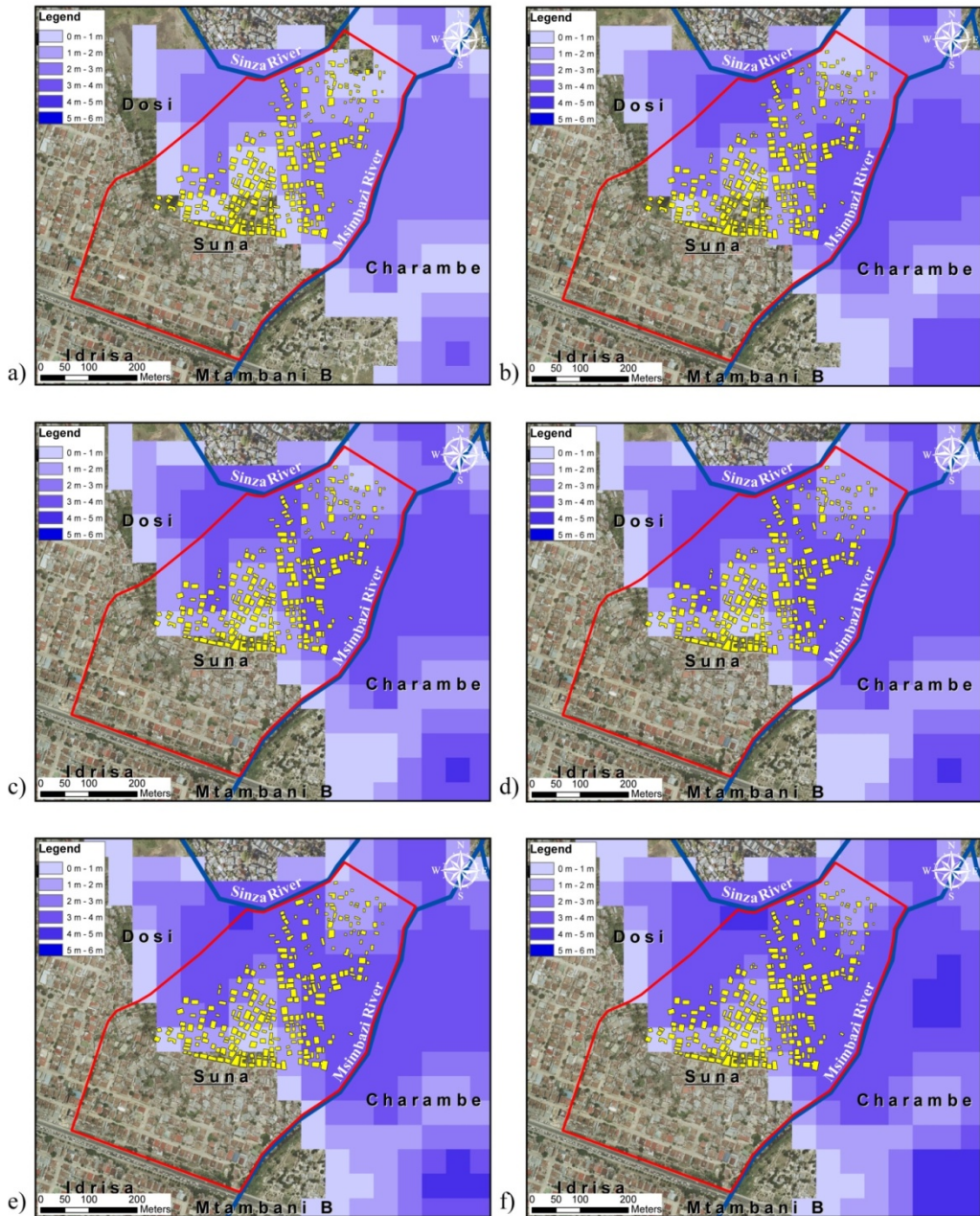


Figure 3.12 - Inundation profiles for different return periods, based on historical data, in terms of h_{max} : a) $T_R=2$ years, b) $T_R=10$ years, c) $T_R=30$ years, d) $T_R=50$ years, e) $T_R=100$ years, f) $T_R=300$ years.

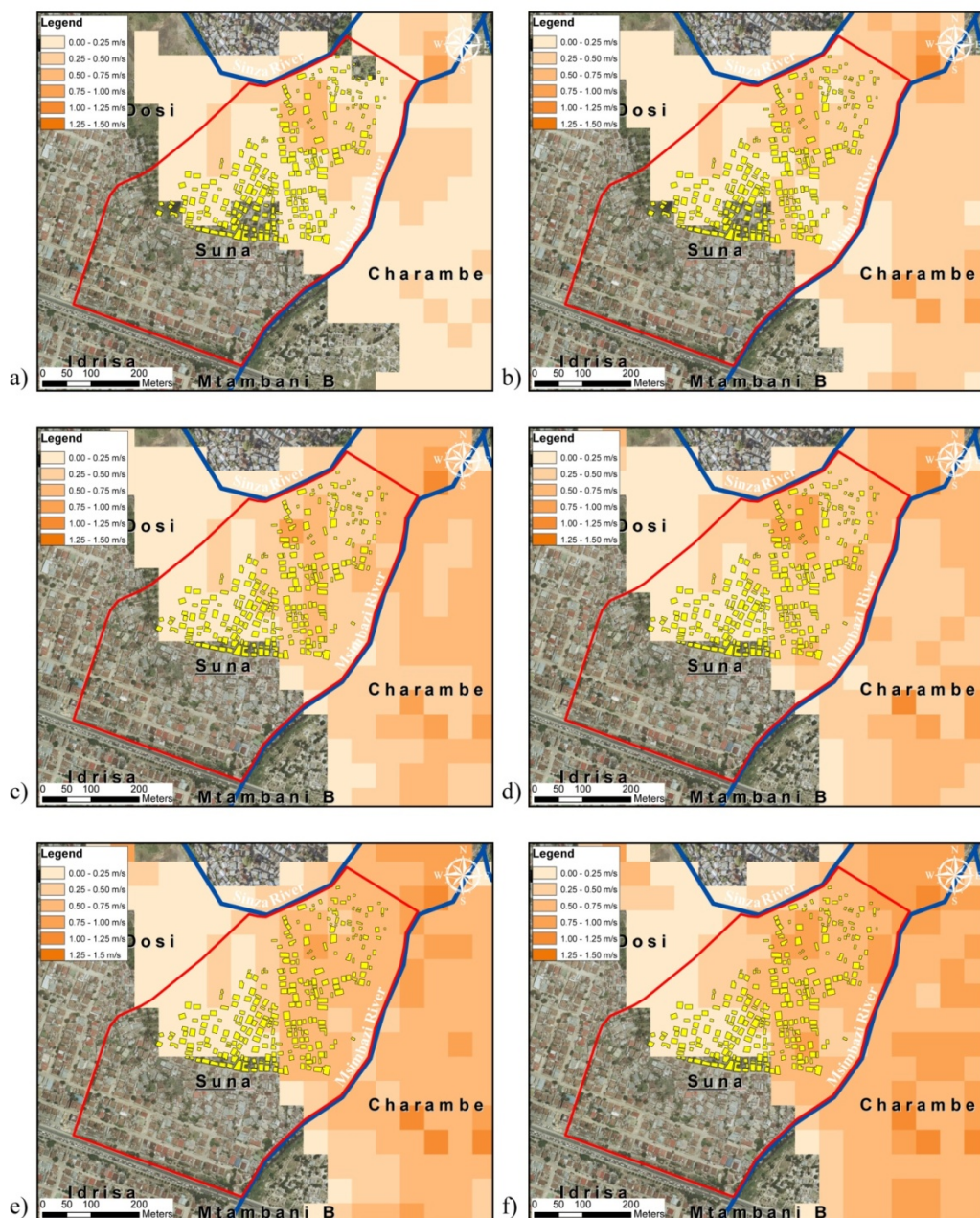


Figure 3.13 - Inundation profiles for different return periods, based on historical data, in terms of v_{max} : a) $T_R=2$ years, b) $T_R=10$ years, c) $T_R=30$ years, d) $T_R=50$ years, e) $T_R=100$ years, f) $T_R=300$ years.

3.6 The case of Little Akaky, Addis Ababa

As the case-study zone for micro-scale flood risk assessment in Addis Ababa, a portion of Little Akaky Sub-City in the southern part of the city is studied.

3.6.1. The rainfall-curve

As mentioned in Section 1.5.1, the rain-fall curve is calculated based on both historical data and a specific climate projection scenario (scenario RCP8.5, the same as the one considered for Dar es Salaam). The historical rainfall data span from 1958 to 2010 and the climate projections are provided up to 2050 (the entire time-series spans from 1959-2050).

The IDF curve is obtained by following the procedure outlined in paragraph 3.1 and is characterized by the following relationship:

$$h_r(d, T_R) = K_{T_R} \cdot 25.06 \cdot d^{0.23} \quad (3.19)$$

The values of the growing factor K_{T_R} are: $K_{10}=1.50$, $K_{30}=1.84$, $K_{50}=2.00$, $K_{100}=2.21$, $K_{300}=2.54$.

The projected IDF curve is obtained by the same procedure, based on the climate change projection and is characterized by the following relationship:

$$h_r(d, T_R) = K_{T_R} \cdot 35.42 \cdot d^{0.29} \quad (3.20)$$

The values of the growing factor K_{T_R} are: $K_{10}=1.67$, $K_{30}=2.12$, $K_{50}=2.33$, $K_{100}=2.61$, $K_{300}=3.05$.

T_R	10 Ys	30 Ys	50 Ys	100 Ys	300 Ys
H	1.50	1.84	2.00	2.21	2.54
CC	1.67	2.12	2.33	2.61	3.05

Table 3.3 - Growing factors for the different return periods (H:historical, CC: climate change)

The rainfall curves with and without climate change effects, classified by

5 different return periods, are plotted in Figure 3.14. It is possible to observe that for Addis Ababa city, the climate change effect induces an increase in terms of intensity. In fact, the IDF curves that take into account the climate projection (the dotted lines in Figure 3.14) are higher than those evaluated based on only historical data (the solid line in Figure 3.14). Moreover, it can be observed that the growing factor K_T for various return periods are higher when considering the effect of climate change. As discussed before, this entails a future increase in the frequency of extreme rainfall events based on this climate projection.

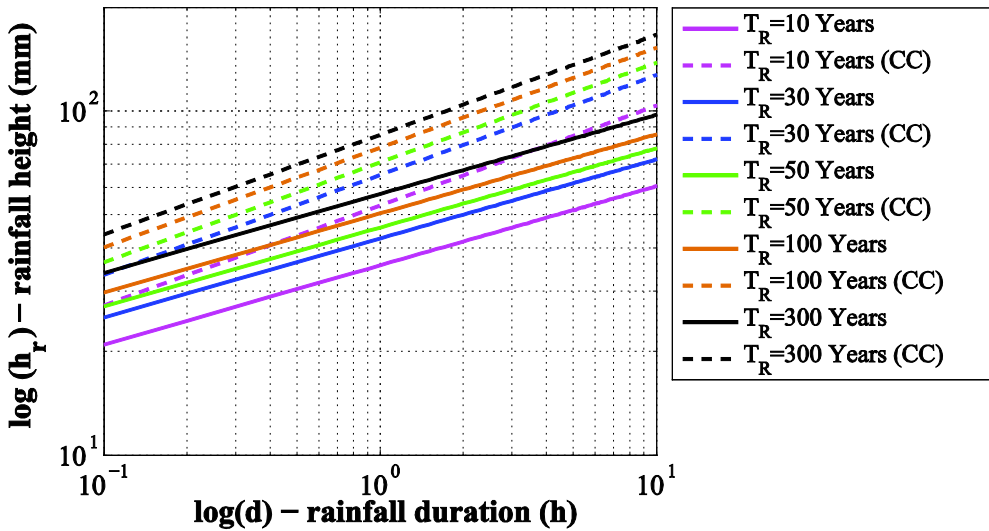


Figure 3.14 - Rainfall probability curves for Addis Ababa with and without climate change effects.

3.6.2. The characterization of the hydrograph

The peak flow for the catchment area considered was evaluated by the Curve Number method, with reference to five different return periods (e.g., 10, 30, 50, 100 and 300-yr) with and without the climate change effects. The inflow hydrographs corresponding to the various return periods considered are illustrated in Figure 3.15.

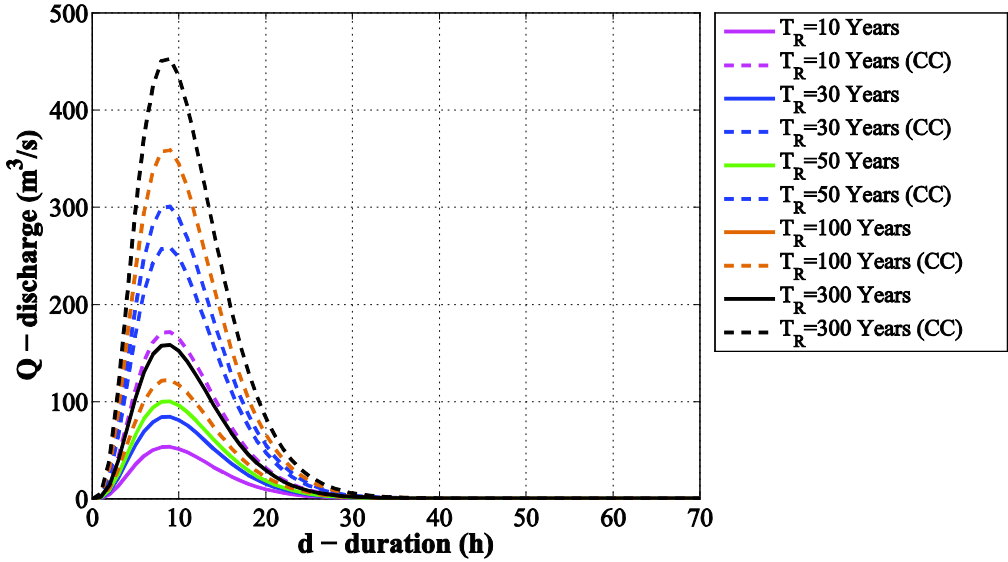


Figure 3.15 - Hydrographs ($T_R = 10, 30, 50, 100$ and 300 years) with and without CC effects

It is possible to observe that the hydrographs obtained based on down-scaled climate projections (the dotted lines in Figure 3.15) are higher than the hydrographs obtained with the historical data (the solid line in Figure 3.15). This results manifest a future increase in the maximum flooding discharge for Little Akaki, Addis Ababa.

3.6.3. The micro-scale flood hazard

Figure 3.16 below illustrates the inundation profiles, in terms of maximum flow depth h_{max} (in meters), calculated through flood volume (area under the hydrograph) propagation using the software FLO2D for the six return periods considered. These inundation profiles are based on historical data.

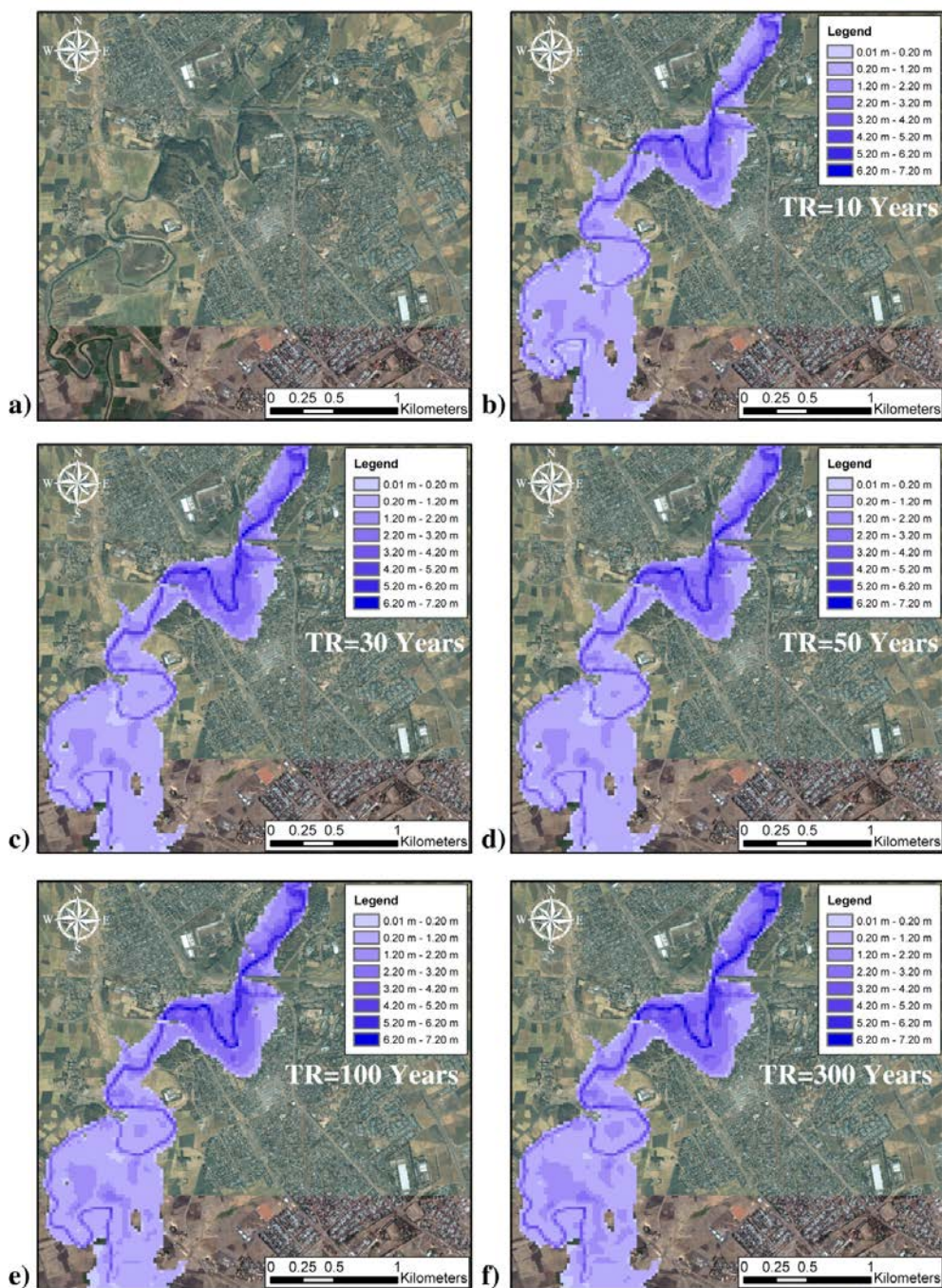


Figure 3.16 - Inundation profiles based on historical data in terms of h_{max} (in meters) for various return periods for the case study area (Little Akaki)

References

1. Maione U. and Mosiello U., *Elementi di statistica per l'idrologia*. 1993.
2. Connolly R.D., Schirmer J., and Dunn P.K., *A daily rainfall disaggregation model*. Agricultural and Forest Meteorology, 1998. **92**: p. 105-117.
3. Güntner A., Olsson J., Calver A., and Gannon B., *Cascade-based disaggregation of continuous rainfall time series: the influence of climate*. Hydrology and Earth System Sciences Discussions, 2001. **5**(2): p. 145-164.
4. Olsson J., *Evaluation of a scaling cascade model for temporal rain-fall disaggregation*. Hydrology and Earth System Sciences Discussions, 1998. **2**(1): p. 19-30.
5. Mockus V., *National engineering handbook, Section 4, hydrology*. US Soil Conservation Service, Washington, DC, 1972.
6. Viparelli C., *Ricostruzione dell'idrogramma di piena*. L'Energia Elettrica, 1963. **6**: p. 421-428.
7. O'Brien J., Julien P., and Fullerton W., *Two-dimensional water flood and mudflow simulation*. Journal of hydraulic engineering, 1993. **119**(2): p. 244-261.
8. FLO-2D S.I., *FLO-2D® User's Manual*. 2004: Nutrioso, Arizona.

Chapter 4

MESO-SCALE FLOOD HAZARD ASSESSMENT

In this chapter, a novel GIS-based Bayesian methodology for the delineation of potentially flood-prone areas, by calibration of the Topographic Wetness Index (TWI) based on available information, is developed. This methodology is particularly useful for flood hazard assessment in a meso-scale using a binary indicator (yes/no) for susceptibility to flooding.

4.1 The Topographic Wetness Index (TWI)

The Topographic Wetness Index [1] allows for the delineation of a portion of a hydrographic basin potentially exposed to flood inundation by identifying all the areas characterized by a topographic index that exceed a given threshold.

The TWI threshold value depends on the resolution of the digital elevation model (DEM), topology of the hydrographic basin and the constructed infrastructure [2, 3]. This threshold value is usually calibrated based on the results of detailed delineation of the inundation profile for selected zones. In this study, the TWI threshold is calibrated based on the calculated inundation profiles for various return periods for selected zones within the basin through a Bayesian framework. The Bayesian framework enables the probabilistic characterization of the threshold by calculating the complementary probability of false delineation of flood prone zones as a function of various threshold values. For a given return period, the probability of false delineation is calculated as the sum of the probability of indicating a zone flood prone, while it is not indicated as such by the inundation profile,

and the probability that a zone is indicated as not flood prone but indicated as flood prone by the inundation profile. Applying the above-mentioned procedure, taking into account all available information on the inundation profiles for various zones within the basin, leads to a probability distribution for the TWI threshold value.

4.1.1. Delineation of flood-prone areas using the TWI

The topographic wetness index, initially introduced by Kirkby [4], has been shown to be strongly correlated to the area exposed to flood inundation [2, 3, 5]. The *TWI* for a given point **O** within the hydrographic basin is calculated as following:

$$TWI = \log \left(\frac{A_s}{\tan \beta} \right) \quad (4.1)$$

where A_s is the specific catchment area expressed in meters and calculated as the local up-slope area draining through point **O** per unit contour length (A/L); β is the local slope at the point in question expressed in degrees. Figure 4.1 illustrates the main components used for the calculation of the *TWI* at a given point **O** within the hydrographic basin, namely the catchment area A for point **O**, the length L of the contour line, and the specific catchment area A_s .

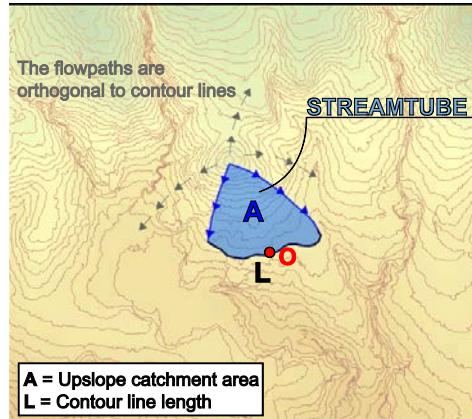


Figure 4.1 - The main components of the TWI calculation.

The *TWI* allows for the delineation of a portion of a hydrographic basin potentially exposed to flood inundation (referred to herein as flood prone or more briefly as *FP*) by identifying all the areas characterized by a topographic index that exceeds a given threshold. The *TWI* threshold value depends on the resolution of the digital elevation model (DEM), the topology of the hydrographic basin and the presence of constructed infrastructures (such as sewage system, bridges and culverts). This threshold is usually calibrated based on the results of detailed delineation of the inundation profile for selected zones.

4.2 Using the inundation profiles for the calibration of the *TWI* threshold

As was mentioned in the previous section, the *TWI* method delineates the flood prone areas as the portions of the basin for which the topographic index exceeds a prescribed threshold. One way for establishing the *TWI* threshold is to use the available inundation profile for one (or more) zones of interest within the basin. The inundation profile, reported as the flooding heights (and velocities) for various nodes within a lattice covering a given area for different return periods, can be obtained by means of classic hydraulic routines of various degrees of sophistication and accuracy [6]. The calculation of the inundation profiles is already explained in Chapter 3.

The inundation profile can be used to delineate the inundated areas (referred to hereafter as *IN*), for a given return period, as those areas within the zones of interest where the inundation height is greater than zero.

4.3 Maximum likelihood estimation of the *TWI* threshold

As mentioned before, the delineation of flood-prone areas is strictly dependent on the *TWI* threshold. In this study, the *TWI* threshold is calibrated probabilistically based on the calculated inundation profiles for various return periods for a selected zone within the basin by employing the maximum

likelihood parameter estimation. This section describes how the likelihood function for the TWI threshold is calculated based on the inundation profile available for a selected zone of interest within the basin (micro-scale).

Let W represent the spatial window of a zone of interest (within the basin) for which the inundation profile is calculated. Moreover, let FP represent the flood-prone areas identified as $TWI > \tau$ and $IN(T_R)$ represent the inundated areas for a given return period T_R identified as $h(T_R) > 0$; where $h(T_R)$ is the flooding height calculated for a given point within the zone of interest W . Figure 4.2 (a) illustrates in a schematic manner zone W and the portions identified as FP and $IN(T_R)$.

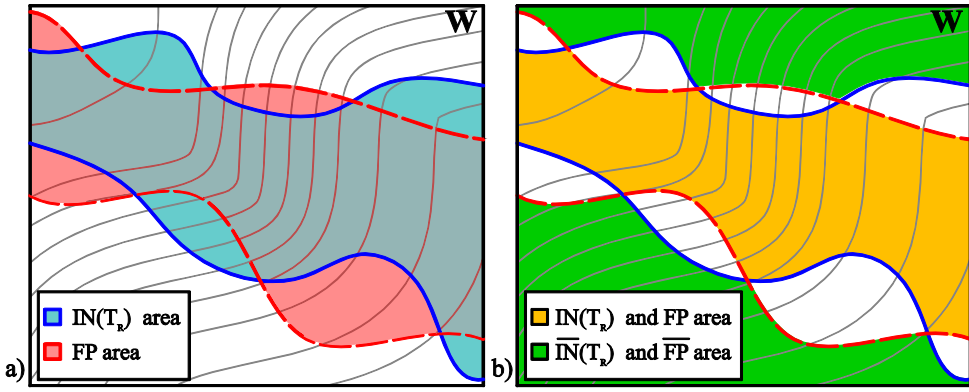


Figure 4.2 - FP and IN areas

The probability of the correct delineation of the flood-prone areas or the likelihood function for the TWI threshold τ denoted as $L(\tau|W)$ for various values of τ can be calculated as following:

$$L(\tau|W) = P(FP, IN(T_R) | \tau, W) + P(\overline{FP}, \overline{IN(T_R)} | \tau, W) \quad (4.2)$$

where $P(FP, IN(T_R) | \tau, W)$ denotes the probability that a given point within zone W is identified both as flood-prone FP (using the TWI method) and inundated $IN(T_R)$ (using the more accurate inundated profiles), for a given return period T_R and conditioned on (the $|$ sign) a given value of τ of the TWI threshold. The area FP and $IN(T_R)$ is indicated by color orange in Figure 4.2 (b).

Similarly, $P(\overline{FP}, \overline{IN}(T_R) | \tau, W)$ denotes the probability that a given point within the zone of interest is neither identified as FP nor as $IN(T_R)$ conditioned on a given value of τ of the TWI threshold. The area not FP and not $IN(T_R)$ is indicated by color green in Figure 4.2 (b). It can be shown that the likelihood function in Eq. (4.2) can be equivalently expressed as the complement of probability of false delineation of flood-prone areas or the so-called cry-wolf:

$$L(\tau | W) = P(FP, IN(T_R) | \tau, W) + P(\overline{FP}, \overline{IN}(T_R) | \tau, W) \quad (4.3)$$

where $P(FP, \overline{IN}(T_R) | \tau, W)$ for a given point within zone W denotes the probability that it is indicated as FP by the TWI method but not $IN(T_R)$ in the more accurate delineation of the inundated zones. Vice versa, $P(\overline{FP}, IN(T_R) | \tau, W)$ for a given point within zone W denotes the probability that it is not indicated as FP but its results as inundated in the delineation of the inundated zones.

Going back to Eq. (4.2), the terms $P(FP, IN | \tau, W)$ and $P(\overline{FP}, \overline{IN} | \tau, W)$ can be expanded, using the probability theory's product rule [7], as following:

$$P(FP, IN(T_R) | \tau, W) = P(FP | \tau, W) \cdot P(IN(T_R) | FP, \tau, W) \quad (4.4)$$

$$P(\overline{FP}, \overline{IN}(T_R) | \tau, W) = P(\overline{FP} | \tau, W) \cdot P(\overline{IN}(T_R) | \overline{FP}, \tau, W) \quad (4.5)$$

where the term $P(IN | FP, \tau, W)$ for a given point denotes the probability of being IN given that it is identified as FP and $P(\overline{IN} | \overline{FP}, \tau, W)$ denotes the probability of not being IN conditioned on not being FP , given the threshold value τ . The terms $P(FP | \tau, W)$ and $P(\overline{FP} | \tau, W)$ represent the probability of being FP or not being FP respectively, given the TWI threshold value τ .

4.3.1. Estimation of the likelihood function using the areal extent: Part 1, the micro-scale estimation

Let $A_W(FP)$ denote the areal extent of the flood-prone portion of the zone W identified via the TWI method (note that $A_W(FP)$ is a function of τ since the

flood-prone areas are identified as areas with $TWI > \tau$, the extent of the portion colored as red in Figure 4.2(a)); let $A_W(IN(T_R))$ denote the areal extent of the inundated portion of W identified via hydraulic calculations for a given return period (the extent of the portion colored as blue in Figure 4.2 (a)). Analogously, $A_W(\overline{FP})$ and $A_W(\overline{IN(T_R)})$ refer to the areas of the not flood-prone and not inundated portions, respectively. The probability terms $P(IN(T_R)|FP, \tau, W)$ and $P(\overline{IN(T_R)}|\overline{FP}, \tau, W)$ can be estimated by the ratio of areal extents, as expressed in the following:

$$P(IN(T_R)|FP, \tau, W) = \frac{A_W(IN(T_R), FP)}{A_W(FP)} \quad (4.6)$$

$$P(\overline{IN(T_R)}|\overline{FP}, \tau, W) = \frac{A_W(\overline{IN(T_R)}, \overline{FP})}{A_W(\overline{FP})} \quad (4.7)$$

where $A_W(IN(T_R), FP)$ denotes the areal extent of the portion of the area W that is both FP and $IN(T_R)$ (the extent of the area colored as orange in Figure 4.2 (b)); $A_W(\overline{IN(T_R)}, \overline{FP})$ denotes the areal extent of the portion of the area W that is neither FP nor $IN(T_R)$ (the extent of the area colored as green in Figure 4.2 (b)). As mentioned above, the areal extents $A_W(IN(T_R), FP)$, $A_W(\overline{IN(T_R)}, \overline{FP})$, $A_W(FP)$ and $A_W(\overline{FP})$ are --by definition-- all functions of the TWI threshold τ .

4.3.2. Estimation of the likelihood function using the areal extent: Part 2, the micro-scale estimation

In the previous section, it was demonstrated how $P(IN(T_R)|FP, \tau, W)$ and $P(\overline{IN(T_R)}|\overline{FP}, \tau, W)$ were estimated using the areal extent ratios calculated in a micro-scale delineated by window W . However, also $P(FP|\tau, W)$ and $P(\overline{FP}|\tau, W)$ need to be estimated in order to be able to calculate the likelihood function. It has been chosen to estimate the above two terms using the areal

extents calculated in the meso-scale (city-level)⁴. Denoting the total administrative area of the city under consideration as A_{urban} and denoting the total areal extent within the city having TWI greater than the given threshold τ as $A_{urban}(FP)$, one can estimate the term $P(FP|\tau)$ ⁵ as:

$$P(FP|\tau) = \frac{A_{urban}(FP)}{A_{urban}} \quad (4.8)$$

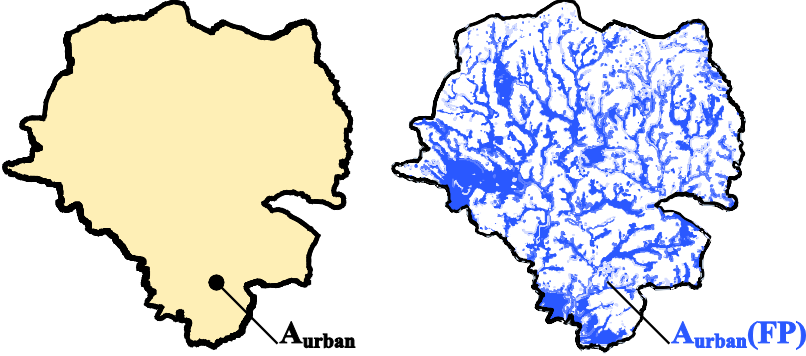


Figure 4.3 - Identification of the total urban area (A_{urban}) and the flood prone urban area ($A_{urban}(FP)$) for a given threshold

Figure 4.3 demonstrates schematically the areal extents A_{urban} and $A_{urban}(FP)$ for a given value of τ for the city of Addis Ababa. The probability $P(FP|\tau)$ can then be calculated as $1 - P(FP|\tau)$.

Finally, the likelihood function in Eq. (4.2) can be calculated by substituting the terms calculated in Equations (4.6,4.7) and (4.8) in Eqs. (4.4) and (4.5) and summing up these two last equations. The maximum likelihood estimate for the TWI threshold can be calculated as the τ value that maximizes the likelihood function in Eq. (4.2).

⁴ Note that this term could have also been estimated based on the information contained within window W . However, it was chosen to use the whole extent of the city as reference. Therefore, in this case the information provided by the inundation profiles within W is not used. In fact, the term $P(FP|\tau, W)$ is referred to as $P(FP|\tau)$ hereafter.

⁵ The conditioning on W is left out for brevity and simplicity of formulations.

4.3.3. *Using Bayesian parameter estimation in order to estimate τ based on information from more than one spatial window*

Suppose that some background information is available on the value of the TWI threshold τ . In that case, the maximum likelihood method presented in the previous section can be extended to a Bayesian parameter estimation, where the available background information is represented by a prior probability distribution. That is, the posterior probability distribution for τ given the information provided by the inundation profile within the spatial window W can be expressed as⁶:

$$p(\tau|W) = \frac{L(\tau|W)p(\tau)}{\sum L(\tau|W)p(\tau)} \quad (4.9)$$

where $p(\tau|W)$ denotes the posterior probability distribution for τ given spatial window W ; $L(\tau|W)$ is the likelihood function for τ calculated in the previous section and $p(\tau)$ is the prior probability distribution for τ before having the information on the inundation profile for window W . Note that Eq. (4.9) is particularly useful for calculating the threshold τ having the inundation profiles for than one spatial window within the basin. In that case, the posterior probability $p(\tau|W_1)$ can be used as prior probability distribution in order to calculate the posterior probability distribution $p(\tau|W_1, W_2)$ considering both spatial windows W_1 and W_2 and so on and so forth.

⁶ Strictly speaking, the formulation in Eq. 9 should have been conditioned on the "correct identification" of the flood-prone areas for window W (see Eq. 2). However, for the sake of simplicity and tractability of the equations, we have used the symbol W in order to imply in, a concise manner, all the additional information about the inundation profile contained within window W .

4.3.4. Calibration of TWI threshold based on information other than the inundation profile

It is worth noting that the probabilistic methodology presented in this thesis for the estimation of TWI threshold can also be used based on information other than the inundation profile. For instance, approximate maps delineating the flood prone areas for a city (e.g., based on historical information) can be used instead of the inundation profile for calibrating the threshold. Of course, in this case, the spatial window of interest W would be equal to the entire area of the city or the partial area for which the flood prone areas are delineated.

4.4 The case of Addis Ababa

In the following, the methodology described earlier is implemented in order to identify urban flooding hot spots in the city of Addis Ababa (for brevity referred to also as Addis), Ethiopia.

4.4.1. Delineation of flood prone areas for Addis Abab using the topographic wetness index (TWI)

The TWI is calculated in a GIS framework by applying Eq. (4.1) and based on a digital elevation model of the city (Year: 2007, vertical resolution: 1 meters). Figure 4.4 illustrates the resulting TWI map for Addis. It can be observed that the TWI values vary between 7 and 22; in particular, largest TWI values can be spotted around the natural water channels.

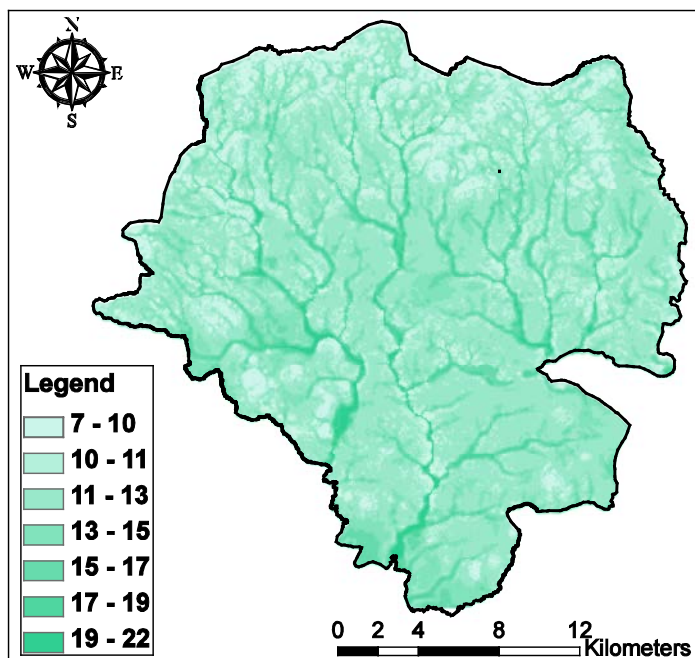


Figure 4.4 - TWI for Addis Ababa

4.4.2. *The inundation profile for Little Akaki*

In order to calibrate the *TWI* threshold for Addis, the inundation profile for various return periods have been calculated for the Little Akaki area located in the southern part of Addis. Little Akaki results as flood-prone based on past flooding experiences. The inundation profile has been calculated by bi-dimensional simulation of flood volume propagation using the software FLO-2D (using historical rainfall records, the DEM, and the calculation of the hydrograph based on the curve number method) assuming a simulation time of 45 hours. The outcome of the flood propagation is illustrated in Chapter 3 in terms of maximum flow depth h_{max} with reference to five considered return periods (TR 10, 30, 50, 100 and 300 years).

4.4.3. *Maximum likelihood estimation of the flood-prone threshold*

This section explains how the procedure described previously in the

methodology can be applied in order to calculate the likelihood of being flood prone as a function of the *TWI* threshold.

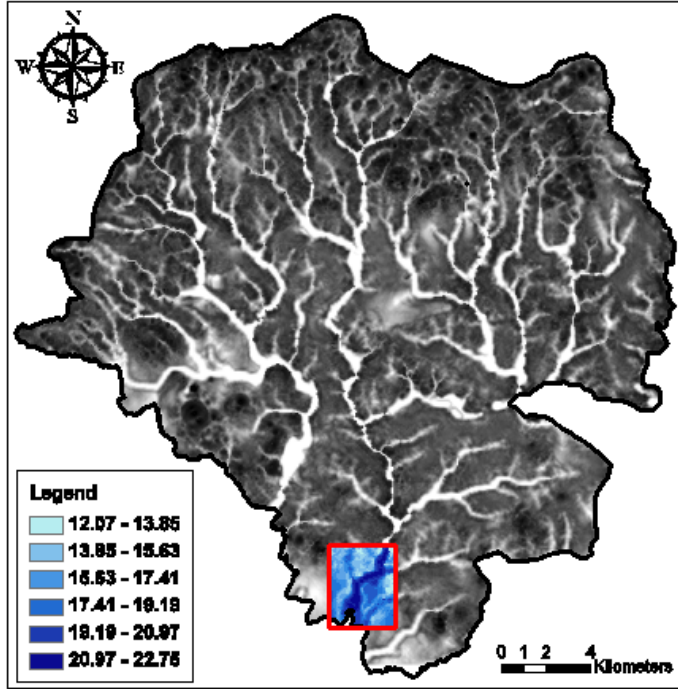


Figure 4.5 - The *TWI* and the spatial the window for hydraulic analyses at Little Akaki

A spatial window identified as W with $A(W)$ around 11 km² is defined in the zone of little Akaki (Figure 4.5). For a return period $T_R=100$ years and for all the possible values of τ , the probability that a given zone is flood prone $P(FP|\tau)$ is calculated from Eq. (4.8) (based on meso-scale estimations) and is plotted in Figure 4.6(a) (as the black dots). Moreover, the probability that a given point is inundated $P(IN|FP,\tau)$ given that it is already indicated as FP for a given value of τ is calculated from Eq. (4.6) (based on micro-scale estimations) and plotted in Figure 4.6(a) (as the stars in gray). The probability that a given point is indicated both as flood prone (by the *TWI* method) and inundated (based on the inundation profile), $P(FP,IN|\tau)$ is calculated from Eq. (4.4) as the product of $P(FP|\tau)$ and $P(IN|FP,\tau)$ from Eq. (4.4) and plotted in

Figure 4.6(a) (as the circles in red). In a similar manner, the probability that a given point is not indicated as flood prone based on the *TWI* method is calculated as the complementary probability of being flood prone in Eq. (4.8) and plotted in Figure 4.6(b) (as the black dots). The probability that a given zone is not indicated as inundated given that it is not flood prone for a given value of τ is calculated from Eq. (4.7) and is plotted as the gray stars in Figure 4.6(b). Finally the probability that a given point is not inundated and not flood prone for a given value of τ , is calculated from Eq. (4.5) and plotted as the red circles in Figure 4.6(b).

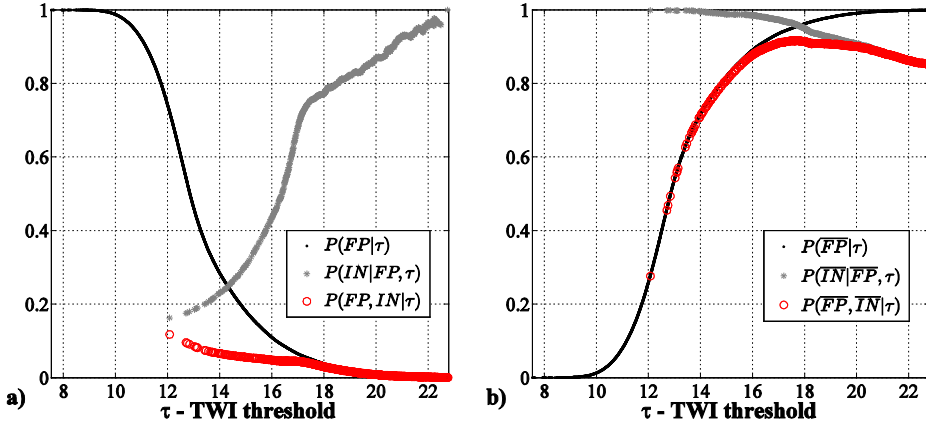


Figure 4.6 - a) Probability of being FP and IN given τ . b) Probability of being \overline{FP} and \overline{IN} given τ .

The likelihood function for window W at $T_R=100$ years is finally calculated from Eq. (4.2) by summing up the probability of being flood prone and inundated and the probability of not being flood prone and not being inundated for all possible τ values (i.e., summing up the curves illustrated by red circles in Figure 4.6(a) and Figure 4.6(b)). It is noteworthy that the probability $P(FP|\tau)$ and its complement are both defined in the domain of the threshold values ranging between 7.5 and 22.8 (the meso-scale estimations, Figure 4.4). Instead, the terms $P(IN|FP, \tau)$ and $P(\overline{IN}|\overline{FP}, \tau)$ are defined in the domain ranging between 12.1 and 22.8 (the micro-scale estimations, Figure

4.5).

The resulting likelihood function $L(\tau|W)$ is plotted in Figure 4.7 (a) as a function of the TWI threshold τ . Consequently, the maximum likelihood estimate for τ (i.e., the value that corresponds to the maximum likelihood) can be identified as $\tau=17.1$. Furthermore, by identifying the τ values corresponding to 99% of the maximum likelihood value, it is possible to define a maximum likelihood interval, that varies between $\tau_{ML}=16.7$ and $\tau^+_{ML}=17.9$. That is, from a practical point of view, the information used for calibrating the TWI threshold lead to identifying a maximum likelihood interval $[16.7, 17.9]$ for τ .

Recalling that the likelihood function also represents the probability density function (pdf) for τ , the cumulative distribution for τ can be calculated as the cumulative sum of the pdf. Figure 4.7 (b) illustrates the CDF for τ together with the threshold values corresponding to 16th and 50th percentiles of the probability distribution equal to 14.3, and 17.7, respectively.

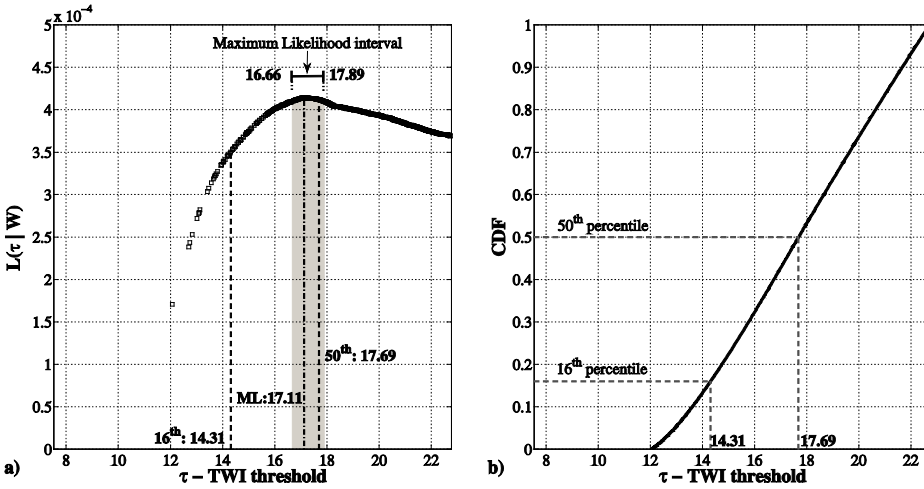


Figure 4.7 - a) The likelihood function $L(\tau|W)$ (also the probability density for τ); b) threshold CDF.

A basic visual check of the accuracy of the results (within window W) can be performed by overlaying the inundated zones (obtained from the hydraulic routine) and the TWI map for threshold values larger than the

maximum likelihood estimate for τ denoted by τ_{ML} equal to 17.1 (i.e., $TWI > \tau_{ML}$). Figure 4.8 below illustrates for the local window W , the result of overlaying of hydraulic profile and $TWI > \tau_{ML}$ for T_R of 100 years.

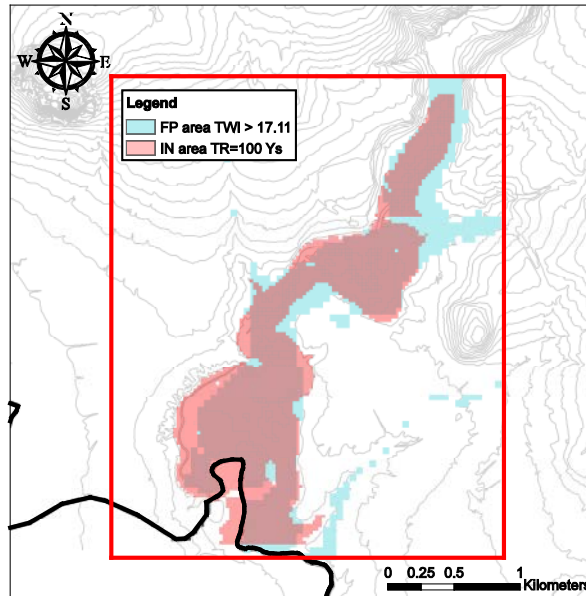


Figure 4.8 - Overlay of FP and IN areas for the spatial window W (Little Akaki).

The maximum likelihood estimation procedure is repeated also for the other return periods for which the hydraulic profiles have been calculated. The results are illustrated in Figure 4.9 (a) and Figure 4.9 (b) as the likelihood function and the cumulative distribution function for τ , respectively. As is depicted in Figure 4.9 (a), the maximum likelihood estimate does not depend on the value of the return period. Moreover, the cumulative distributions functions plotted for various return periods are almost identical. This is revealed also by examining the inundation profiles for various return periods in Figure 3.16 in Chapter 3. It can be observed that the delineation of the inundated areas is not sensitive to the return period (as opposed to flood height which is sensitive to the return period).

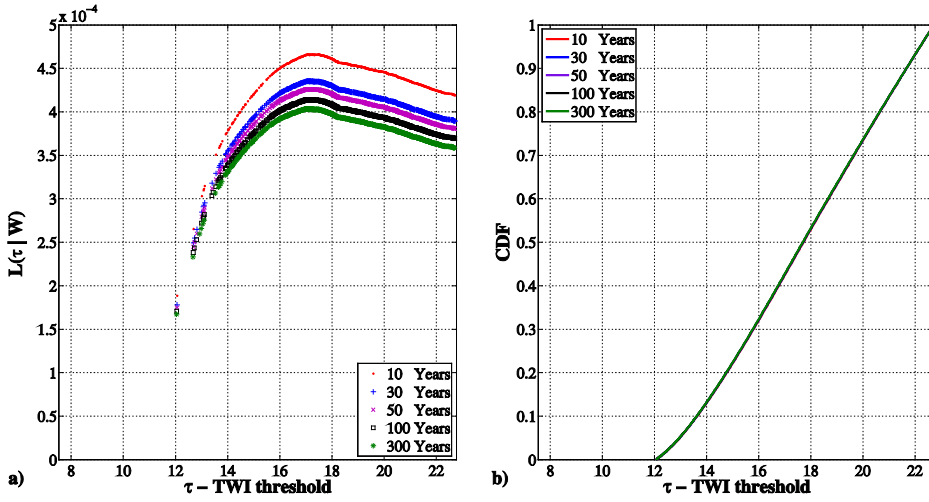


Figure 4.9 - a) The likelihood function $L(\tau|W)$. b) threshold CDF for different return periods.

The above-mentioned discussion can be summarized in the following table that reports various statistics of the threshold value τ : the maximum likelihood estimate (ML), the 16th and 50th percentiles for TWI threshold and the 99% maximum likelihood interval $[\tau_{ML}^-, \tau_{ML}^+]$ for various return periods.

T_R	τ_{ML}	τ_{16}	τ_{50}	τ_{ML}^-	τ_{ML}^+
10	17.48	14.33	17.72	16.71	17.99
30	17.11	14.32	17.70	16.66	17.93
50	17.11	14.32	17.70	16.66	17.91
100	17.11	14.31	17.69	16.66	17.89
300	17.05	14.31	17.69	16.64	17.85

Table 4.1 - The statistics for the TWI threshold distribution as a function of the return period

Hereafter in this work, maximum likelihood threshold (τ_{ML}) equal to 17.05, 16th percentile (τ_{16}) equal to 14.31, 50th percentile (τ_{50}) equal to 17.7 and the 99% maximum values interval $[16.6, 17.9]$, are adopted.

Using Bayesian parameter estimation in order to estimate τ based on information from more than one spatial window

As mentioned, Eq. (4.9) can be used to calculate the threshold τ based on the inundation profiles for more than one spatial window within the city. The inundation profiles for $T_R=300$ yrs were available also for another zone of Addis hereafter referred to as Zone 1. This area is located between the subcities of Akaki (on the right) and Nefas Silk (on the left). Using the same procedure outlined in the previous section for the zone Little Akaki (hereafter referred to as Zone 2), the likelihood function for τ can be calculated. The probability density function τ denoted by $p(\tau|W_1)$ is plotted in Figure 4.10 (b) below, recalling that the likelihood function $L(\tau|W_1)$ is equal to the probability density function for τ (using a uniform prior $p(\tau)$ in Eq. (4.9)). It can be observed that the distribution becomes almost uniform (in other words: non informative) for τ larger than about 17.

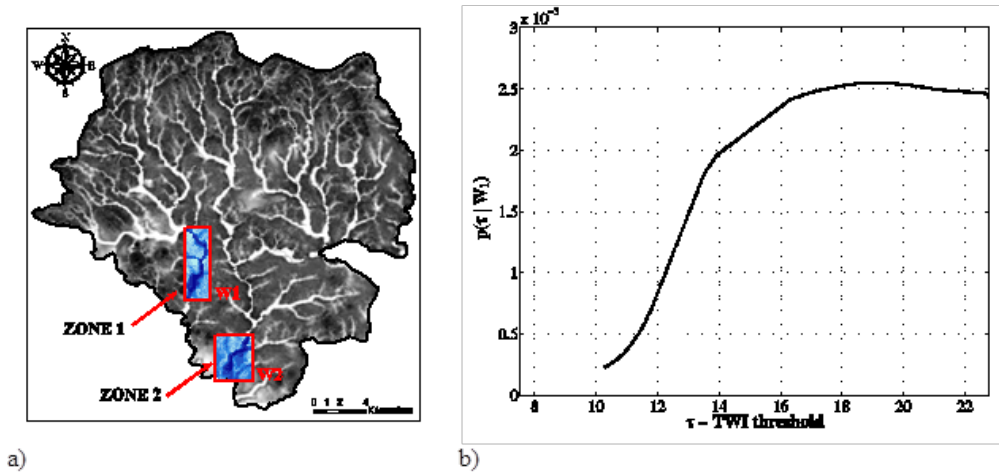


Figure 4.10 - a) Zones 1 and 2. b) $p(\tau|W_1)$:the posterior distribution calculated for the Zone1 and used as prior for Zone 2

The posterior distribution $p(\tau|W_1)$ obtained for Zone 1, can be used as prior distribution for Zone 2, (the procedure outlined in the previous section is equivalent to using a uniform distribution). In Figure 4.11 below, the results based on inundation profiles calculated for Zone 2 (part (a), reported in the

previous section) and the results based on inundation profiles calculated for Zone 1 and Zone 2 (part (b)) can be compared.

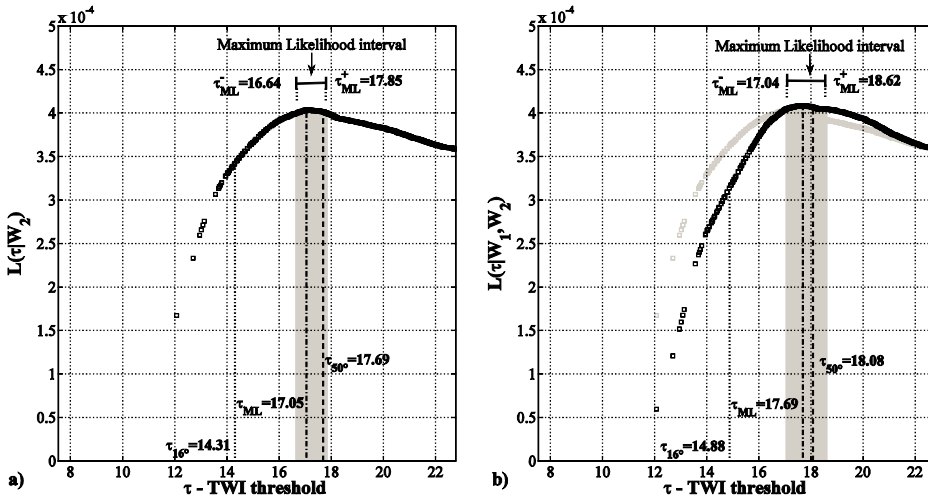


Figure 4.11 - a) the likelihood $L(\tau|W_2)$; b) the posterior distribution $p(\tau|W_1, W_2)$.

It can be observed that the statistics calculated for the *TWI* threshold do not change significantly by calibrating based on two spatial windows W_1 and W_2 ; for example, the τ_{ML} changes from 17.1 to 17.7. However, considering both spatial windows for calibration, leads to slightly wider 99% maximum likelihood interval for τ .

4.5 The case of Dar es Salaam

4.5.1. Delineation of flood-prone areas for Dar es Salaam using the topographic wetness index (TWI)

The topographic wetness index is calculated in the GIS framework by applying Eq. (4.1) and based on the digital elevation model of the city (Year: 2008, vertical resolution: 10 meters, reduced to 2 meters through the spatial interpolation). Figure 4.12 illustrates the resulting *TWI* map for Dar. It can be observed that the *TWI* values vary between 10.34 and 22.78; in particular, largest *TWI* values can be spotted around the natural water channels.

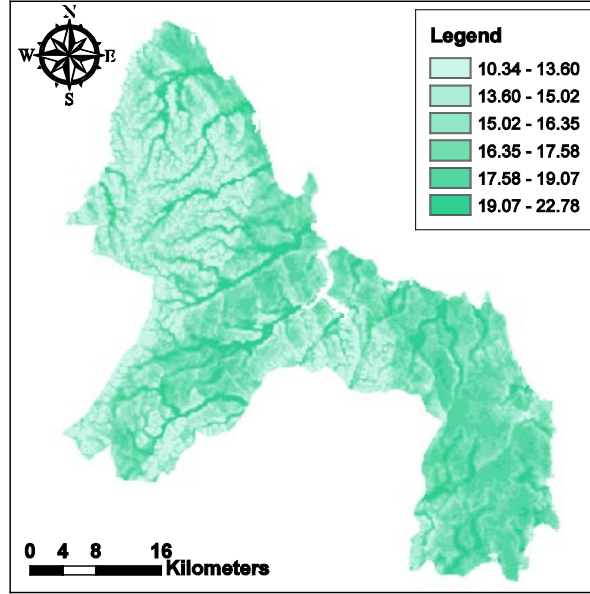


Figure 4.12 - TWI for Dar Es Salaam

4.5.2. *The inundation profile for Suna*

In order to calibrate the TWI threshold for Dar Es Salaam, the inundation profile for various return periods have been calculated for Suna located in between Ilala and Kinondoni districts. Suna results as flood-prone based on past flooding experiences. The inundation profile has been calculated by bi-dimensional simulation of flood volume propagation using the software FLO-2D (using historical rainfall records, the DEM, and the calculation of the hydrograph based on the curve number method) assuming a simulation time of 45 hours. The outcome of the flood propagation is illustrated in Figure 3.12 in terms of maximum flow depth h_{max} with reference to six considered return periods (TR 2, 10, 30, 50, 100 and 300 years).

4.5.3. *Maximum likelihood estimation of the flood-prone threshold*

In this section, it is demonstrated how the procedure described previously in the methodology can be applied in order to calculate the

likelihood of being flood prone as a function of the *TWI* threshold.

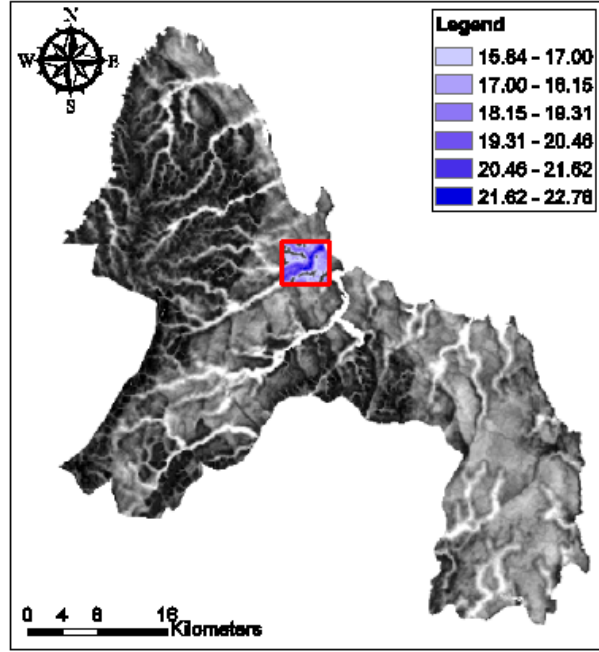


Figure 4.13 - The TWI and the spatial the window for hydraulic analyses at Suna

A spatial window identified as W with $A(W)$ around 27 km^2 is defined in the zone of Suna (Figure 4.13). For a return period $T_R=100$ years and for all the possible values of τ , the probability that a given zone is flood prone $P(FP | \tau)$ is calculated from Eq. (4.8) (based on meso-scale estimations) and is plotted in Figure 4.14 (a) (as the black dots). Moreover, the probability that a given point is inundated $P(IN | FP, \tau)$ given that it is already indicated as FP for a given value of τ is calculated from Eq. (4.6) (based on micro-scale estimations) and plotted in Figure 4.14 (a) (as the stars in gray). The probability that a given point is indicated both as flood prone (by the *TWI* method) and inundated (based on the hydraulic profile), $P(FP, IN | \tau)$ is calculated from Eq. (4.4) as the product of $P(FP | \tau)$ and $P(IN | FP, \tau)$ from Eq. (4.4) and plotted in Figure 4.14 (a) (as the circles in red). In a similar manner, the probability that a given point is not indicated as flood prone based on the *TWI* method is calculated as the complementary probability of being flood prone in Eq. (4.8) and plotted in

Figure 4.14(b) (as the black dots). The probability that a given zone is not indicated as inundated given that it is not flood prone for a given value of τ is calculated from Eq. (4.7) and is plotted as the gray stars in Figure 4.14 (b). Finally the probability that a given point is not inundated and not flood prone for a given value of τ , is calculated from Eq. (4.5) and plotted as the red circles in Figure 4.14 (b).

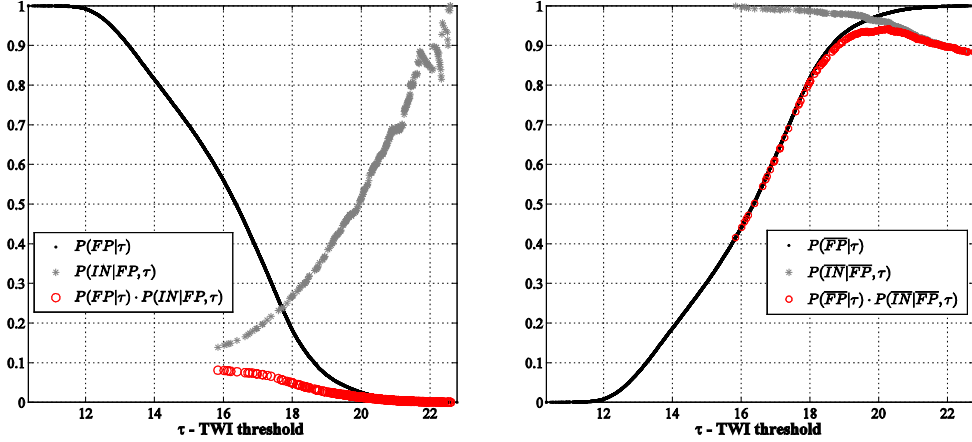


Figure 4.14 - a) Probability of being FP and IN given τ . b) Probability of being \overline{FP} and \overline{IN} given τ .

The likelihood function for window W at $T_R=100$ years is finally calculated from Eq. (4.2) by summing up the probability of being flood prone and inundated and the probability of not being flood prone and not being inundated for all possible τ values (i.e., summing up the curves illustrated by red circles in Figure 4.14 (a) and Figure 4.14 (b)). It is noteworthy that the probability $P(FP|\tau)$ and its complement are both defined in the domain of the threshold values ranging between 10.34 and 22.78 (the meso-scale estimations, Figure 4.12). Instead, the terms $P(IN|FP, \tau)$ and $P(\overline{IN}|\overline{FP}, \tau)$ are defined in the domain ranging between 15.84 and 22.78 (the micro-scale estimations, Figure 4.13).

The resulting likelihood function $L(\tau|W)$ is plotted in Figure 4.15 (a) as a

function of the TWI threshold τ . Consequently, the maximum likelihood estimate for τ (i.e., the value that corresponds to the maximum likelihood) can be identified as $\tau=19.53$. Furthermore, by identifying the τ values corresponding to 99% of the maximum likelihood value, it is possible to define a maximum likelihood interval, that varies between $\tau_{ML}=19.16$ and $\tau^+_{ML}=20.44$. That is, from a practical point of view, the information used for calibrating the TWI threshold lead to identifying a maximum likelihood interval [19.16, 20.44] for τ .

Recalling that the likelihood function also represents the probability density function (pdf) for τ , the cumulative distribution for τ can be calculated as the cumulative sum of the pdf. Figure 4.15 (b) illustrates the CDF for τ together with the threshold values corresponding to 16th and 50th percentiles of the probability distribution equal to 17.31, and 19.50, respectively.

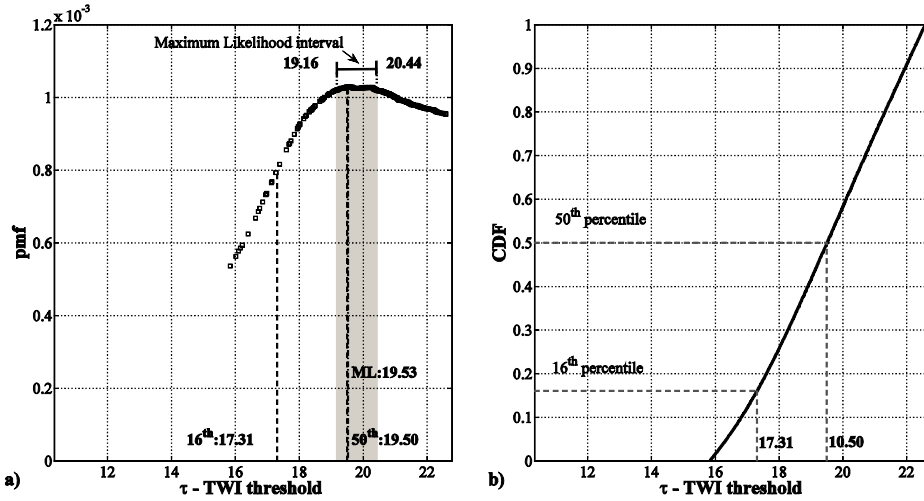


Figure 4.15 - a) The likelihood function $L(\tau|W)$ (also the probability density for τ); b) threshold CDF.

A basic and visual check of the accuracy of the results (within window W) can be performed by overlying the inundated zones (obtained from the hydraulic routine) and the TWI map for threshold values larger than the maximum likelihood estimate for τ denoted by τ_{ML} equal to 19.53 (i.e., $TWI > \tau_{ML}$). Figure 4.16 below illustrates for the local window W , the result of

overlaying of hydraulic profile and $TWI > \tau_{ML}$ for T_R of 100.

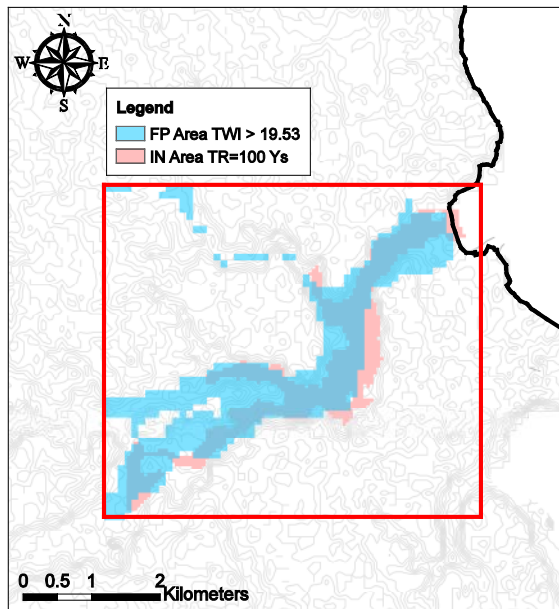


Figure 4.16 - Overlay of FP and IN areas for the spatial window W.

The maximum likelihood estimation procedure is repeated also for the other return periods for which the inundation profiles have been calculated. The results are illustrated in Figure 4.17 (a) and Figure 4.17 (b) as the likelihood function and the cumulative distribution function for τ , respectively. As it can be depicted from Figure 4.17 (a), the maximum likelihood estimate does not depend on the value of return period. Moreover, the cumulative distributions functions plotted for various return periods are almost identical. This is revealed also by examining the inundation profiles for various return periods in Figure 3.12. It can be observed that the delineation of the inundated areas is not sensitive to the return period (as opposed to the flood height that is sensitive to the return period).

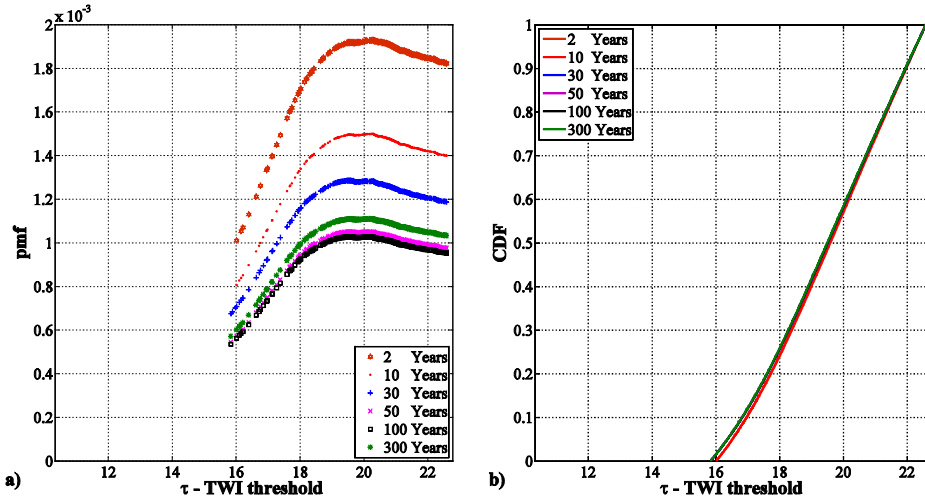


Figure 4.17 - a) The likelihood function $L(\tau|W)$. b) threshold CDF for different return periods.

The above-mentioned discussion can be summarized in the following table that reports various statistics of the threshold value τ : the maximum likelihood estimate (ML), the 16th and 50th percentiles for TWI threshold and the 99% maximum likelihood interval $[\tau_{ML}^-, \tau_{ML}^+]$ for various return periods.

T_R	τ_{ML}	τ_{16}	τ_{50}	τ_{ML}^-	τ_{ML}^+
2	20.28	17.44	19.59	19.40	20.81
10	20.28	17.42	19.57	19.24	20.60
30	20.17	17.32	19.51	19.17	20.57
50	19.53	17.31	19.51	19.16	20.46
100	19.53	17.31	19.50	19.16	20.44
300	19.53	17.30	19.50	19.12	20.40

Table 4.2 - The statistics for the TWI threshold distribution as a function of the return period

Hereafter in this work, maximum likelihood threshold (τ_{ML}) equal to 19.53, 16th percentile (τ_{16}) equal to 17.30, 50th percentile (τ_{50}) equal to 19.50 and the 99% maximum values interval $[19.12, 20.40]$, are adopted.

4.6 The case of Ouagadougou

On September 1, 2009, an unprecedented deluge of rain hit the capital city of Ouagadougou and resulted in wide-spread damage (destruction of buildings and infrastructure). More than 25 cm of rainfall in 12 hours turned the streets of Ouagadougou into fast-flowing rivers. The infrastructure were severely affected as the floods cut off electricity, fresh water and fuel supplies. The city is used to heavy seasonal rainfall but this was the worst flooding in 50 years. An estimated 109.000 people were left homeless. The areal extent of this flooding event is used, in the Bayesian framework described in this chapter, in order to delineate the flood-prone areas for Ouagadougou.

4.6.1. *Delineation of flood-prone areas for Ouagadougou using the topographic wetness index (TWI)*

The topographic wetness index is calculated in the GIS framework by applying Eq. (4.1) and based on the digital elevation model of the city (Vertical resolution: 3 meters). Figure 4.18 illustrates the resulting TWI map for Ouagadougou. It can be observed that the TWI values vary between 8 and 25; in particular, largest TWI values can be spotted around the natural water channels.

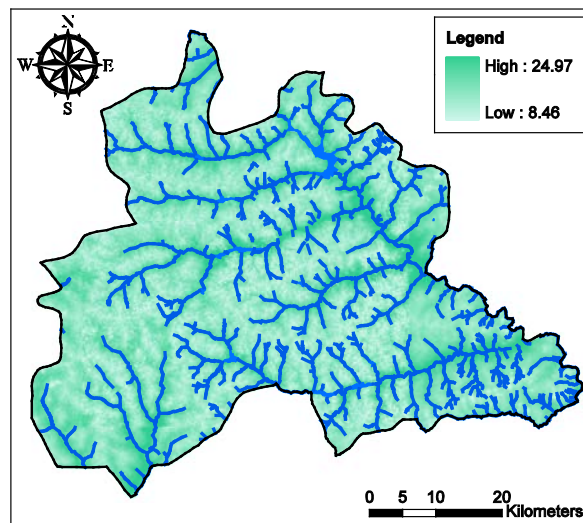


Figure 4.18 - TWI for Ouagadougou

4.6.2. The inundation profile

In contrast to the TWI thresholds calculated for Dar and Addis which were calibrated based on calculated inundation profiles, the threshold value for Ouaga is calibrated based on the inundated area of the 2009 flooding event (Figure 4.19).

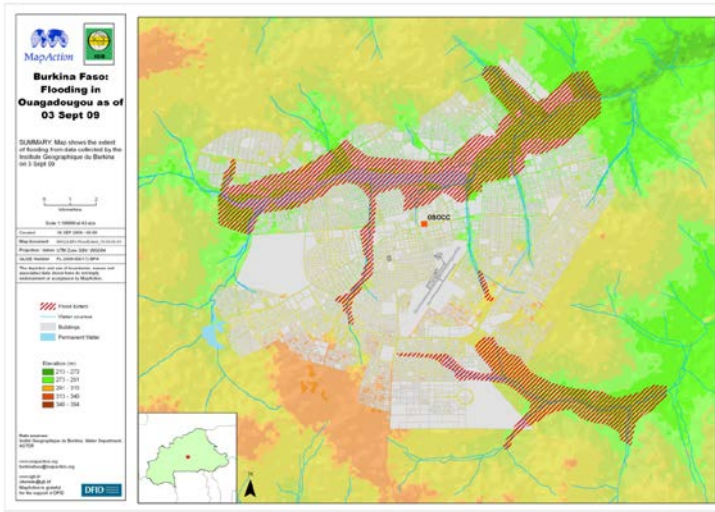


Figure 4.19 - Inundated area of in the September 2009 flooding event

Based on the information available at the internet site (<http://www.mapaction.org/map-catalogue/mapdetail/1719.html>), it was possible to geo-reference the previous image and generate a spatial dataset.

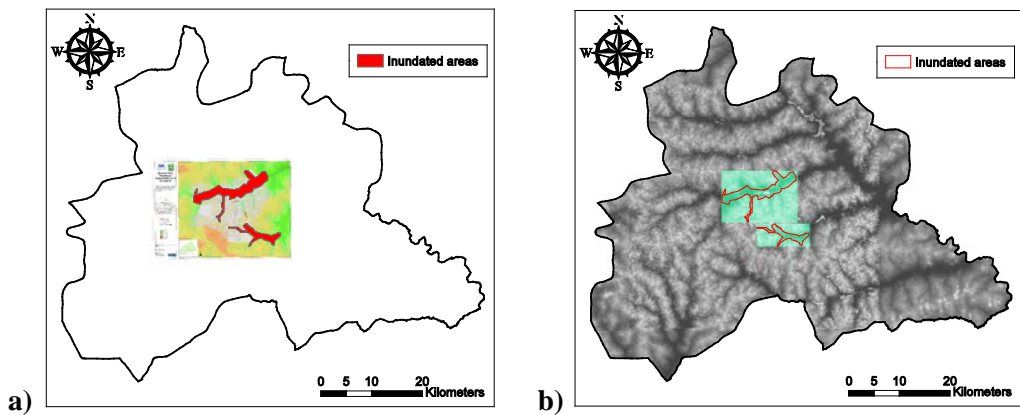


Figure 4.20 - a) Inundated areas after the 2009 events, b) Area 1 (the smaller) and Area 2 (the bigger)

As it can be depicted from Figure 4.20, two inundated areas are identified. In the following, the smaller area is called Area 1 and the bigger area is referred to as Area 2.

4.6.3. Maximum likelihood estimation of the flood-prone threshold

In this section, it is demonstrated how the procedure described previously can be applied in order to calculate the likelihood of being flood prone as a function of the TWI threshold. In this case, the Bayesian parameter estimation is adopted based on information from more than one spatial windows (see Section 4.3.3). In particular, the information acquired from the study of the Area 1 are used as a-priori information for the study of the Area 2.

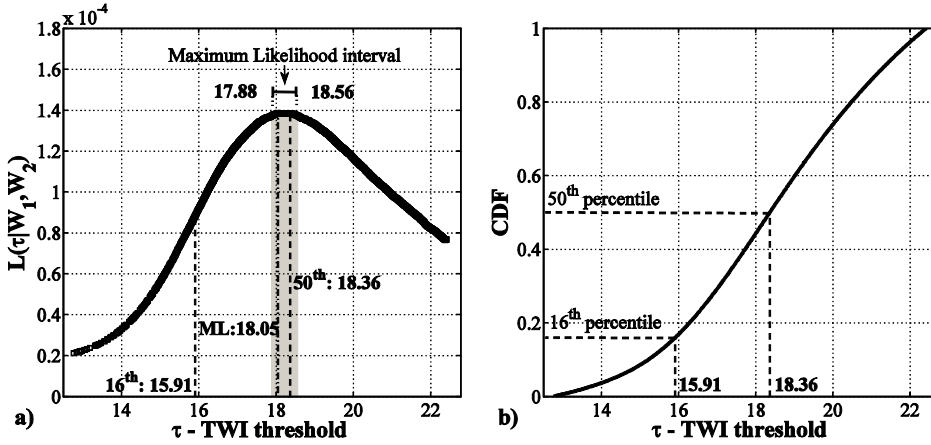


Figure 4.21 - The likelihood function $L(\tau|W_1, W_2)$, b) threshold CDF

Table 4.3 reports the threshold values that are calculated with the proposed procedure.

τ_{ML}	τ_{16}	τ_{50}	τ_{ML}^-	τ_{ML}^+
18.05	15.91	18.36	17.88	18.56

Table 4.3 - The statistics for the TWI threshold distribution for the case of Ouagadougou

It is possible to observe in Figure 4.22(a) that the TWI map with a threshold equal to the maximum likelihood TWI threshold τ_{ML} matches the spatial extent of the areas inundated by the 2009 flooding event. Moreover, the corresponding map of the flood-prone area for the entire city of Ouagadougou is shown in Figure 4.22(b).

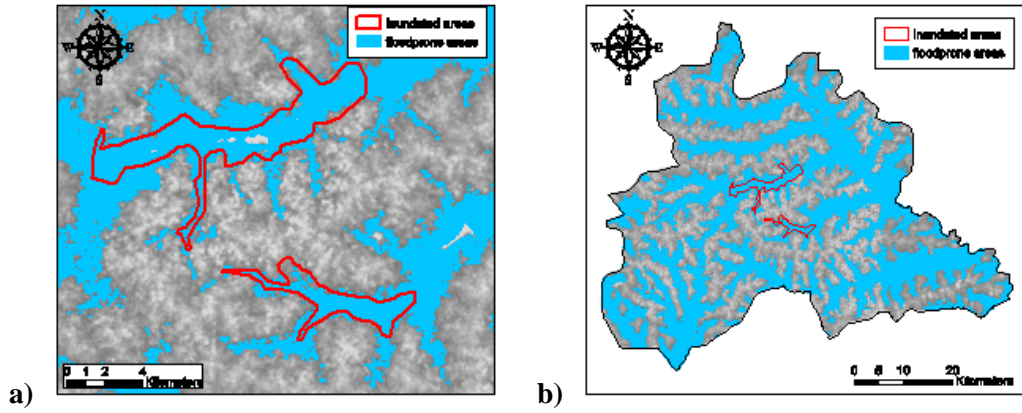


Figure 4.22 - a) Matching for the inundate areas, b) flood prone areas for the entire city.

References

1. Qin C.-Z., Zhu A.X., Pei T., Li B.-L., Scholten T., Behrens T., and Zhou C.-H., *An approach to computing topographic wetness index based on maximum downslope gradient*. Precision Agriculture, 2011. **12**(1): p. 32-43.
2. Manfreda S., Di Leo M., and Sole A., *Detection of Flood-Prone Areas Using Digital Elevation Models*. Journal of Hydrologic Engineering, 2011. **16**(10): p. 781-790.
3. Manfreda S., Sole A., and Fiorentino M., *Can the basin morphology alone provide an insight into floodplain delineation?* WIT Trans. Ecol. Environ, 2008. **118**: p. 47-56.
4. Kirkby M.J., *Hydrograph modelling strategies*, in *Progress in physical and human geography*, R.F. Peel, M.D. Chisholm, and a.P. Haggett, Editors. 1975: London. p. 69-90.
5. Manfreda S., Sole A., and Fiorentino M., *Valutazione del pericolo di allagamento sul territorio nazionale mediante un approccio di tipo geomorfologico*. 2007. **4**: p. 43-54.
6. Apel H., Aronica G.T., Kreibich H., and Thieken A.H., *Flood risk analyses – how detailed do we need to be?* Natural Hazards, 2008. **49**: p. 79-98.
7. Jaynes E.T., *Probability theory: The logic of science*. 2003: Cambridge university press.

Chapter 5

PORTFOLIO FLOOD VULNERABILITY ASSESSMENT

(FOR A PORTFOLIO OF INFORMAL SETTLEMENTS)

This chapter is dedicated to a novel probability-based methodology for flooding vulnerability assessment for a portfolio of buildings. A *portfolio* of buildings/components is a group of buildings/components with (almost⁷) uncorrelated structural response. A portfolio can be further sub-divided into various *classes* of buildings/components. A class of buildings/components can be defined as a homogenous group of buildings/components that have in common a set of basic criteria (e.g., building material, number of stories, roof material, ..., etc.). As a case-study, the methodology described in this section is applied to micro-scale vulnerability assessment of the informal settlements in Suna Subward, Dar es Salaam City. It turns out that the portfolio of informal settlements in a small area (micro-scale) can be characterized by a single class of buildings. However, the developed methodology is applicable in general to a portfolio of structures that is consisted of more than one classes of buildings.

The flood vulnerability for a class of structures is evaluated analytically by means of an efficient Bayesian simulation-based methodology. This methodology is based on a thorough characterization of the various sources of uncertainty⁸; such as, build-to-building variability within a given class, uncertainty in loading parameters, and uncertainty in material mechanical

⁷ Strictly speaking, the hydrodynamic performance of the buildings within a portfolio may reveal spatial correlations --due to dependence on maximum flow velocity.

⁸ Neglecting the uncertainties in the human response to flooding.

properties. The flood vulnerability for a class of structures is represented by the *fragility curve* (and its plus/minus one standard deviation confidence interval) for a given *limit state*. Furthermore, it is demonstrated how the fragility curves corresponding to the various classes identified within a portfolio can be combined in order to define the flooding fragility for a portfolio of structures for a prescribed limit state.

A hybrid definition is used for characterizing the limit states used in this work. That is, the limit states considered reflect not only the structural response of the buildings but also the content damage. In any case, the fragility curves are defined as the probability distributions (cumulative distribution function, CDF) for the critical water-height marking the threshold of the limit state under consideration. As a results, the critical water height values corresponding to prescribed limit states, may be obtained based on, structural analysis, geometrical characteristics and nominal values.

This chapter focuses on the damages induced by inland flooding events (e.g., riverine flood, flash floods and floods due to failure of drainage system). The latter occurs when there is an overflow of the stream channel, or breaching of a levee or a dam.

5.1 Flood damage typologies

According to [1] the damages induced by floods can be classified in two categories: *qualitative* and *quantitative*. The qualitative damages include human conditions like anxiety, mental suffering or inconvenience. On the other hand, the quantitative damages can be measured in economic terms. The latter can be subdivided in *indirect* and *direct* damages. The indirect damages can be quantified --in economic terms-- as a function of downtime and its consequent disruption of the economic and social activities. The direct damages are due to the interaction between the water flow and the physical system (i.e. structure, infrastructure, green space, etc.). This thesis focuses on this latter typology of damages.

In the recent years, increasing attention is focused on flooding risk

assessment. In fact, several publications discuss the consequences of flooding, such as loss of life [2], economic losses [3-5], and damage to buildings [6-10]. These research efforts have many aspects in common, such as a direct link between the flooding intensity and the incurred damage, and that they are based on real damage observed in the aftermath of the flooding event. In particular, the direct flooding damage to a physical systems may be classified by employing alternative *damage scales* consisting of discrete *damage states*. Kelman [11] has defined six damage states (from DS0 to DS5), classifying water interaction with the structure from no water contact to structural collapse or undermining of the foundation. Schwarz and Maiwald [9, 10] proposed a modified damage scale by removing the damage state zero DS0 (no water contact) and distinguishing between structural and non-structural damage.

On the other hand, many research efforts are starting to galvanize in the direction of proposing analytical models for flood vulnerability assessment taking into account the many sources of uncertainties. Nadal et al. [12] propose a stochastic method for the assessment of the direct impact of flood actions on buildings.

The direct flooding damage in buildings can be classified in three categories, namely, infiltration-seepage, material deterioration/erosion, and structural member failure.

5.1.1. Infiltration-seepage

If the building is not protected by a special flood-resistant barrier or if the foundation is on or under the ground level, water can easily reach into contact with the building. Once there is direct contact with the structure, water seepage and infiltration may take place through either insufficiently water-tight openings (e.g., doors, windows) or through non water-tight building material. Of course, water seepage/infiltration is a time-dependent process and the velocity of infiltration depends on the degree of water-tightness of openings/building material.

If water enters the buildings, the total hydrostatic pressure exerted on the

walls is going to be reduced and therefore the risk of wall failure becomes more remote. However the un-planned presence of water inside the building is going to lead the material deterioration and erosion, non sanitary living conditions, loss of functionality of the facilities anchored at the ground level (i.e. electrical and mechanical fittings), and even risk of drowning in water.

5.1.2. *Material deterioration/erosion*

Elongated contact with water is going to manifest itself either in the form of the physical loss of material volume (erosion), chemical reaction due to chloride content in the water (salinisation), and overall reduction in the material mechanical properties (loss of resistance). For example the vertical façade made up of earthen material and/or poor quality cement blocks are particularly vulnerable to material deterioration as a result of elongated contact with water. Generally speaking, if a building is not realized based on specific flood-resistant provisions, it can be particularly exposed to the undesirable effects of direct contact with water.

5.1.3. *Structural member failure (structural failure)*

The structural failure of supporting walls and slabs in a given section due to flooding pressure is more likely to take place due to a combination of the hydrostatic pressure, hydrodynamic pressure and debris impact, assuming that the walls are sufficiently anchored by the corners and that the openings are properly sealed. The structure is damaged beyond repair due to member failure when, for example, walls collapse, structure translates entirely [13], or the foundation is undermined. It is also important to note that material deterioration and erosion can also lead (indirectly) to structural failure in the form of the loss of vertical load bearing capacity.

5.2 The limit states

As mentioned before, in this work the fragility curves are evaluated analytically. Therefore, the structural limit states are used as a proxy in order to describe the various damage states in the structure. In this thesis, three discrete limit states are considered, namely, serviceability (SE), structural collapse (CO) and life safety (LS). The limit states defined herein are identified based on the corresponding critical water height threshold. This choice is further justified recalling that the flood height is used as the scalar interface variable for the integration of flooding hazard and vulnerability in Section 3.4. It should be mentioned that the choice of limit states in this work targets the informal settlements in particular.

5.2.1. *Serviceability (SE)*

This limit state is marked by the critical water beyond which the normal activities in the household is going to be interrupted, most probably due to water infiltration. For example, for informal buildings built on a raised foundation, one can assume that the critical serviceability water height is equal to the height of raised foundation above the ground level. For buildings constructed according to flood-resistant criteria, the critical water height related to serviceability can be as large as the critical height needed for exceeding the life safety or collapse limit state.

5.2.2. *Structural Collapse (CO)*

The structural collapse limit state consists in the breaking of the bearing structure, collapse of the walls, loss of support of the roof, or loss of loading bearing capacity of the building due to elongated contact with water or salinisation. Generally speaking, structural collapse entails the loss of vertical loading capacity in the structure.

5.2.3. *Life Safety (LS)*

This limit state marks the ultimate state of the structure in which the

lives of the inhabitants is going to be in danger. This can be caused either due to the infiltration of water inside the building (with the increasing risk of drowning in water), or the structural collapse. Therefore, the life safety limit state --as defined in this work-- is a hybrid limit state related to damage to both structural/non-structural elements and also to the exposed content. As a results, as it will be demonstrated later in more details, evaluation of the critical water height corresponding to life safety limit state is based on both quantified structural analysis and also on nominal critical flooding height values established based on the expert judgment or literature (see for example [2]).

5.3 Methodology

5.3.1. *Spatial delineation of the portfolio and its resolution*

The methodology developed in this chapter for portfolio vulnerability assessment to flooding is particularly suitable for detailed micro-scale evaluations (e.g., in a neighborhood) in GIS framework. However, it can be potentially extended to meso-scale evaluations. The spatial delineation of the portfolio is an essential first step in such a procedure. Figure 5.1 demonstrates the spatial components of the portfolio vulnerability assessment.

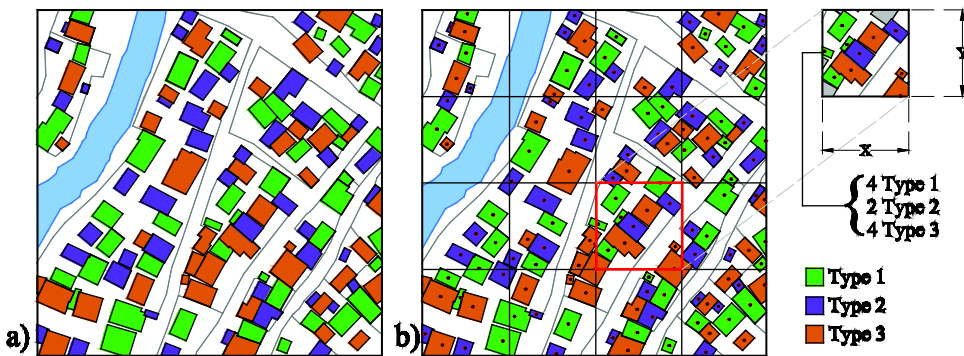


Figure 5.1 - a) The frame delineating the spatial extension of the portfolio;
b) Division of the portfolio frame into spatial units

The frame in Figure 5.1 (a) delineates the spatial boundaries of the portfolio of structures to be analyzed; meanwhile, Figure 5.1 (b) demonstrates further division of the portfolio into smaller spatial units. As it can be observed from the figures, each spatial unit may consist of various buildings classes. In this work, a mono-class (single) spatial unit of scale 1:5000 (micro-scale, a neighborhood) has been considered.

5.3.2. Portfolio vulnerability/fragility formulation

The flood vulnerability/fragility⁹ for a spatial unit within a portfolio for a given limit state (ls) can be calculated as the linear combination of the fragility curves corresponding to the various building classes/types and weighted in proportion to the number of buildings in each class within the spatial unit in consideration:

$$P(ls|h_f) = \sum_{i=1}^k P(ls|h_f, Class_i) \cdot P(Class_i) = \sum_{i=1}^k P(ls|h_f, Class_i) \cdot \frac{N_{Class_i}}{N} \quad (5.1)$$

where $P(ls|h_f)$ is the structural vulnerability/fragility for limit state expressed as the conditional probability of exceeding the limit state ls given a specific flooding height value h_f ; k is number of various building classes considered in the spatial unit; $P(ls|h_f, Class_i)$ is the structural fragility for i -th Class; N is the total number of structures within the spatial unit; and N_{Class_i} is the number of structures that belong to the i -th typology. In this chapter, the procedure for evaluating the structural fragility for a given building class is described in detail.

⁹ In this work, the terms vulnerability and fragility are used interchangeably. However, the term fragility refers to the graphical representation of vulnerability in terms of fragility curves.

5.4 Vulnerability assessment for a single building class

The schematic diagram in Figure 5.2 illustrates the vulnerability assessment procedure of a class of buildings for a prescribed limit state.

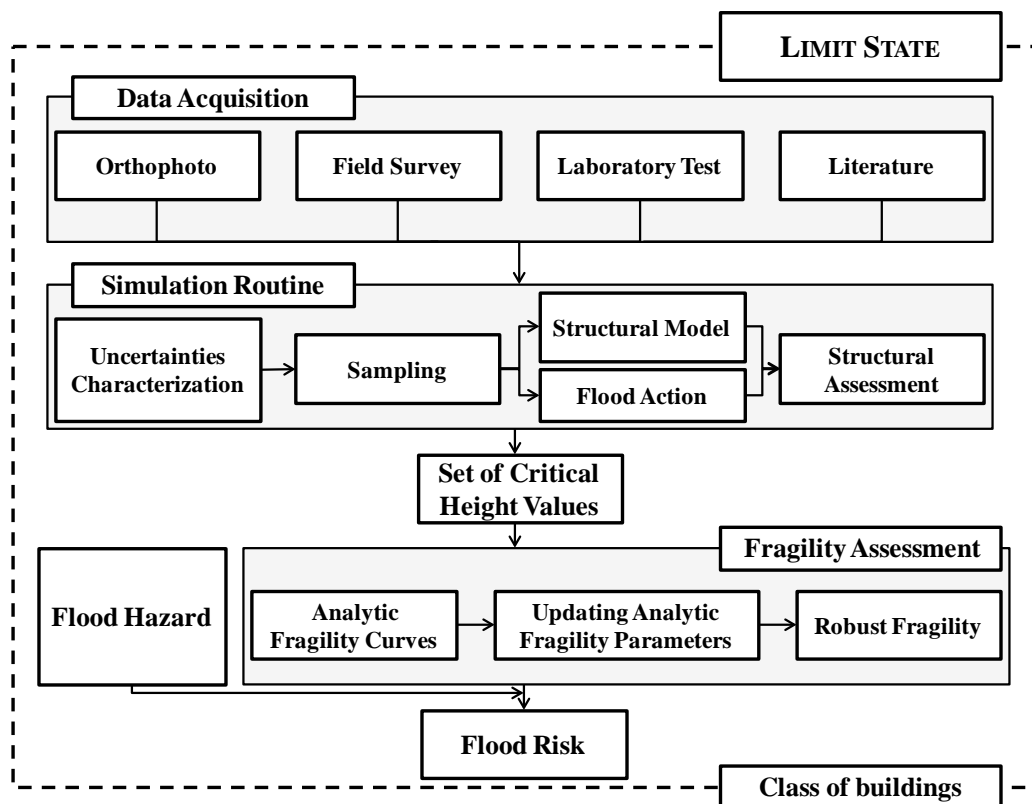


Figure 5.2 - The schematic diagram of the procedure used for the assessment of the vulnerability of the portfolio of structures.

It can be observed that the procedure is divided into three distinct modules: data acquisition, simulation and fragility assessment. Each of these modules is going to be explained herein.

5.4.1. Data acquisition

Data acquisition can be considered the first step in the procedure employed herein for the assessment of the flood vulnerability for a class of

buildings. Ideally, it is desirable to conduct an exhaustive field survey and map out the structural details for all the buildings in the class of structures considered. In the same manner, it is desirable to conduct laboratory tests, that mimic the construction materials and techniques in the field, in order to evaluate the construction materials mechanical properties. In this work --in lieu of exhaustive field surveys and case-specific laboratory tests-- a mix of alternative data sources has been exploited; namely, orthophotos, sample field surveys and literature results.

5.4.2. The simulation routine

Herein, an efficient simulation-based procedure is employed that relies on a small number of Monte Carlo simulations (e.g., in the order of 20-50). The final output of the simulation is a set of critical height values calculated for various realizations of the uncertain parameters θ . Each realization of the vector θ is sufficient to uniquely define the structural model and loading. In the following, the various steps followed in this simulation procedure is described. This simulation routine uses the logic-tree approach in order to propagate the discrete binary uncertain variables. Organization of the binary variables in a logic-tree, in addition to being an efficient visual representation, facilitates the definition of a correlation structure between various uncertain (binary) variables.

5.4.2.1 Characterization of the uncertainties

In general, the uncertainties in the vulnerability assessment problem can be attributed to the following sources:

- *In-complete information:* For example, lack of case-specific laboratory tests on material properties and their deterioration as a result of the elongated contact with water. Even in the presence of tests and material properties, some information is going to be missing with regard to inter-building variability of material mechanical properties.
- *Building-to-building variability:* The fragility curve for a specific structural class is needs to reflect the building-to-building variability in construction

details and geometric configuration. Strictly speaking, if an exhaustive detailed survey of all the buildings within the portfolio is performed, this category reflects the variability rather than uncertainty. However, it is usually not feasible to perform such an exhaustive survey on all the buildings within the portfolio.

Let vector $\underline{\theta}$ denote the set of uncertain parameters taken into account in the evaluation of structural fragility. These uncertain parameters reflect the building-to-building variability within the class, the loading and the mechanical material properties. The vector $\underline{\theta}$ can be sub-divided into two categories: discrete binary uncertain variables (uncertain logical statements) and continuous uncertain variables.

Discrete binary uncertain variables/logic statements: Table 5.1 reports the list of discrete binary uncertain variables/logic statements considered in the procedure.

Presence of raised-foundation / Platform	<i>PL</i>
Presence of Barrier	<i>Ba</i>
Are the doors sufficiently water-proof	<i>DS</i>
Are the windows sufficiently water-proof	<i>WS</i>
Is There a door in the wall panel	<i>D</i>
Are there windows in the wall panel	<i>W</i>
Are there signs of material degradation	<i>DG</i>
Does water-born debris hit the structure	<i>DI</i>

Table 5.1 - Discrete binary uncertain variables considered in the procedure

Examples of the uncertain binary variables considered are, presence of a raised foundation (platform) *PL*, presence of a barrier *Ba*, water-tightness of the door *DS*, water-tightness of the windows *WS*, presence of visual signs of degradation in the building *DG*, and if the water-borne debris is going to hit

the structure DI^{10} . Also the presence of openings (doors D and windows W) in the model wall panel is randomized. This is due to fact that in the specific building wall hit first by the flood (and its angle) are assumed to be unknown.

Continuous uncertain variables: The continuous uncertain variables considered in the procedure can be classified into three categories: (1) parameter related to building geometry (Table 5.2); (2) parameter related to the mechanical material properties (Table 5.3); (3) parameter related to the structural loading.

L (m) - wall length
H (m) - wall height
t (m) - wall thickness
L_w (m) - window length
H_w (m) - window height
H_{wfb} (m) - window rise
L_d (m) - door length
C_d (m) - corner length
H_f (m) - foundation rise
H_b (m) - barrier height

Table 5.2 - The continuous uncertain parameters: building geometry

In the first category, parameters such as structural height, wall thickness, window length and height, window height from the bottom, door length, distance between the corners and the openings, the foundation (platform) height. As far as it regards the second category, parameters such as elastic modulus (E), shear elastic modulus (G) (or alternatively the Poisson ratio (ν)), compressive strength (f_m), shear strength(τ), flexural strength (f_n) for the wall panels are considered.

¹⁰ Note that this binary variable is related to flooding action due to debris impact. The debris impact is described in the section on flood action. The probability that debris is going to hit the structure is evaluated qualitatively (is not based on observed damage).

f_m (MPa) - compression strength
τ_0 (MPa) - shear strength
f_{fl} (MPa) - flexural strength
E (MPa) - linear elastic modulus
G (MPa) - shear elastic modulus
γ (kN/m ³) - self weight

Table 5.3 - The continuous uncertain parameters: material mechanical properties

Ideally, input statistics related to structural material properties should be obtained based on the results of case-specific laboratory tests. The laboratory tests are aimed to mimic the construction materials and relevant techniques used in the field, in order to evaluate the main mechanical characteristics of the wall material. In lieu of case-specific laboratory tests, existing literature results can be used. If only scarce information is available on material properties, the uniform distribution can be used in the range between the minimum and maximum values of the interested parameters.

The third category of uncertain parameters considered is the uncertain loading parameters. In particular, the spatial variability in parameters a and b related to the hydro-dynamic flood loading profile have been considered. These parameters describe the flooding velocity as a power-law function ($a \cdot h^b$) of flooding height at a given point, as demonstrated in Chapter 3. Herein, the parameter a is assumed to be fully correlated with b --through the calculated height/velocity pairs. Thus, in order to simulate the pair of parameters (a , b), only parameter b is simulated.

Logic-trees: Logic-tree [14] is an efficient and visual method for modeling the joint probability distribution for several discrete uncertain variables represented as logic statements. A logic tree is consisted of *nodes*, *branches* and *paths*. Each node represents a logic statement (e.g., given value of an uncertain parameter). Each branch in a logic-tree represents the degree of belief (conditional probability) for the logic statement in the destination node given all the statements corresponding to the nodes along the path leading to (and

including) the node in the origin of the branch. For example, In Figure 5.3, the degrees of belief or the conditional probability values are written in grey characters on the corresponding branch ($|$, reads as *given* or *conditional on*). Each path in a logic-tree is consisted of nodes and branches that connect them; where the nodes belong to progressively increasing levels within the tree. The degree of belief in a path (or the joint probability for the specific values of the corresponding uncertain parameters) is equal to the product of the probabilistic corresponding to the branches that construct the path. Finally, for any vertical cut to the tree, the sum of the degrees of belief for all the paths trimmed by the cut should be equal to unity. That is, the paths trimmed by vertical cuts represent mutually exclusive and collectively exhaustive logic statements.

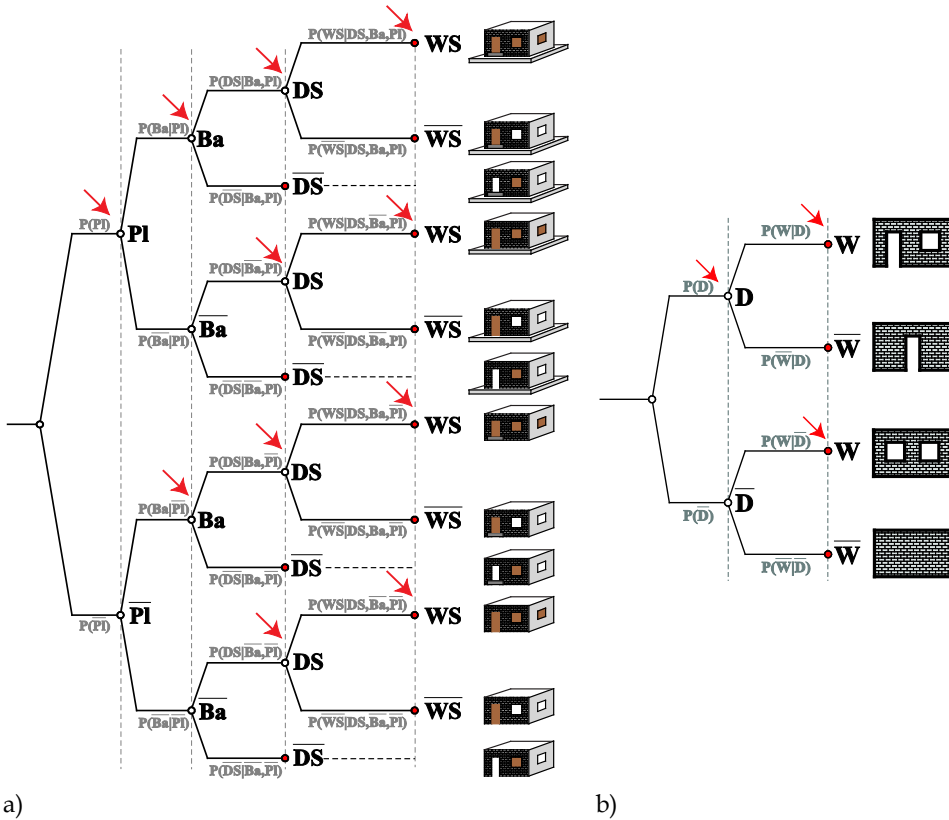


Figure 5.3 - a) logic tree for the waterproofness, b) logic tree for the modeling generation.

Estimating the logic-tree probabilities/degrees of belief: the operative way to assess the conditional probability/degree of belief for each node of the logic tree, consists in cataloging of the survey information, following the conditions imposed by path leading to the node in question. The conditional probabilities corresponding to each branch can be constructed by classifying progressively the building survey results based on the logical value (truth value) of each binary statement (see Table 5.5 as an example). This provides the possibility to take into account the correlation between uncertain parameters/logic statements. The input data necessary for a binary uncertain parameter/logic statement denoted as BV is the number r of surveyed buildings for which the logic statement is TRUE out of number n of all the buildings surveyed. Therefore, the probability π that BV is true can be calculated as a complete Beta-function [15]:

$$p(\pi | r, n) = \frac{(n+1)!}{r!(n-r)!} \pi^r (1-\pi)^{n-r} \quad (5.2)$$

where $p(\pi | r, n)$ denotes the probability distribution for the degree of belief in statement BV given r "success" out of a total of n . The probability π can be estimated in three different ways (a) the expected value $(r+1)/(n+2)$, (b) the maximum likelihood r/n or (c) sampling from the full probability distribution. As an example, the logical statement DG describes the existence of visual signs of degradation in the building. The probability $\pi(\text{DG})$ can be calculated from Equation (5.2) based on the proportion of buildings that reveal signs of degradation. If variable DG is TRUE in a given realization of vector $\underline{\theta}$ the material mechanical properties are going to be reduced by a prescribed percentage (e.g., 75%).

5.4.2.2 Flood Action

In this work, the direct structural damage induced by flooding is assumed to be due to hydrostatic and/or hydrodynamic pressure, and to the accidental action induced by the impact of waterborne debris [16].

The hydro-static pressure: The hydro-static pressure $p_{hs}(z)$ is governed by Stevin's law, and can be calculated through the following relation:

$$p_{hs}(z) = \gamma_w \cdot (H - z) \quad (5.3)$$

where γ_w is the specific weight of water, z is the abscissa measured from the bottom of the structure and H is the flooding height. It should be noted that the special case in which the foundation is under the ground level is not considered; in that case, hydrostatic pressure due to the soil column should also be considered.

The hydro-dynamic pressure: The hydrodynamic actions can be induced due to both flow velocity and also due to transient water level (i.e., waves). However, in an urban context, the hydrodynamic actions due to velocity of the flow seem to be more critical, as also shown in [17]. The force induced by a water flow with velocity v and flow discharge Q can be calculated as:

$$S_{hd}(z) = C_d \cdot \rho_w \cdot Q \cdot v \quad (5.4)$$

where C_d is the drag coefficient (typically ranges between 1.2 and 2.0 according to [18]), and ρ_w is the mass density of the water ($\rho_w = \gamma_w/g$, with g gravity acceleration). Thus, the hydro-dynamic pressure at height z from the ground can be derived as:

$$p_{hd}(z) = C_d \cdot \rho_w \cdot v^2(z) \quad (5.5)$$

where $v(z)$ is the flow velocity at height z . Consequently, the hydrodynamic pressure distribution is directly related to the velocity profile along the height. In lieu of detailed hydraulic calculations, the distribution of velocity along the height can be obtained based on simplified assumptions. Figure 5.4 below illustrates a typical representation of the velocity profile along a vertical surface. It can be observed that the maximum velocity is reached somewhat

below the water surface.

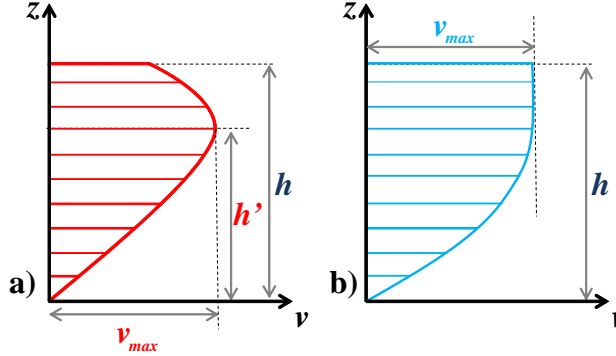


Figure 5.4 - a) velocity profile along the height, b) approximate velocity profile

In this work, an approximate velocity profile along the structural height is assumed as illustrated in Figure 5.4(b). This consists in adopting a parabolic profile that reaches the maximum velocity at the flow surface with a vertical slope. The approximate parabolic profile can be written as a function of the flooding height:

$$\frac{v(z)}{v_{max}} = -\left(\frac{z}{h}\right)^2 + 2 \cdot \left(\frac{z}{h}\right) \quad (5.6)$$

As shown in Chapter 3, the relation between maximum flooding velocity and maximum flooding height at any given point within the zone of interest is approximated with a power-law relation (of the form $v_{max} = a \cdot h_{max}^b$). This power-law fit helps in transforming an otherwise vector-based risk assessment using $\mathbf{H} = [h_{max}, v_{max}]$ as the hazard/fragility interface variable to a scalar risk assessment problem using only h_{max} as the interface variable.

The flood pressure profile: The flood pressure profile is calculated as the sum of the hydrostatic and hydrodynamic pressure profiles, at a given height from the ground level. Figure 5.5 below illustrates the total pressure acting on the wall panel (the right-hand column) and its break-down into hydro-static and hydro-dynamic components for a set of increasing flooding heights and for

two alternative combinations of the pair of parameters (a and b), namely (0.3, 1.15) and (1.5, 1.15). These two pairs of values are representative of two points with low flood velocity and height, and high flood velocity and low flooding height, respectively.

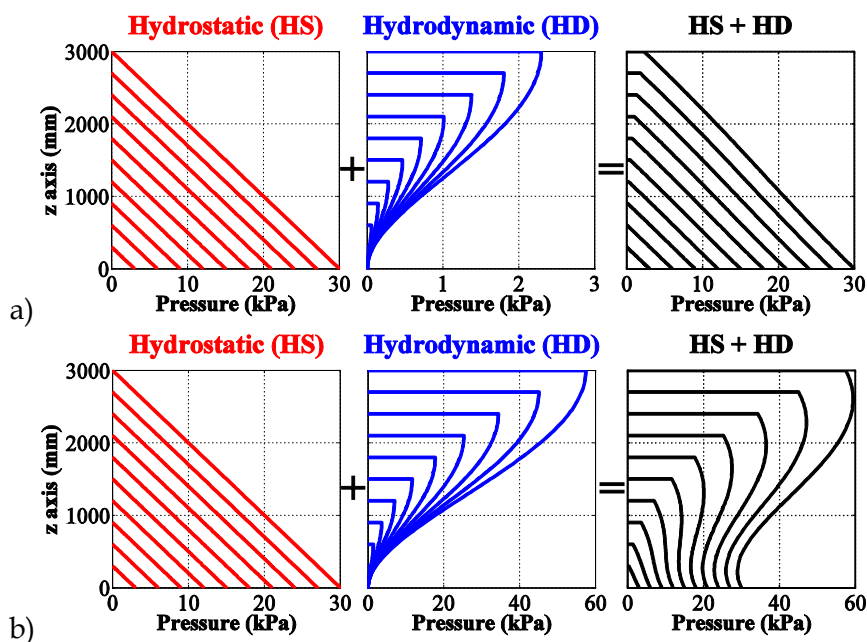


Figure 5.5 - Break-down of the flood pressure profile into hydro-static and hydro-dynamic components for two different pairs of parameters: (a) low flooding height and low velocity; (b) low flooding height and high velocity

It can be observed that the contribution of hydro-dynamic pressure is significant for the case shown in Figure 5.5(b), with small flooding height and large flooding velocity. Generally speaking, the hydrodynamic pressure can be more significant for flood velocity values larger than 1 m/s.

Accidental debris impact: Once the velocity profile is known, it is possible to calculate the debris impact forces. There are alternative formulations for the calculation of the impact magnitude (FEMA 1995, NAASRA 1990, AASHTO 1998) -- leading to substantially equivalent results in the case of tree-trunk impact. In this work the approach outlined in FEMA (1995) has been adopted

to calculate the debris impact. The debris impact (F_{DI}) can be calculated through the following relation:

$$F_{DI} = \frac{W_D \cdot v_D}{g \cdot t} \quad (5.7)$$

where W_D is the debris weight; v_D is the debris velocity (assumed that the debris is waterborne, $v_D=v_{max}$); g is the gravity acceleration; and t is impact duration. Within the simulation procedure, both the fact that the debris hits the structure or not and the horizontal position of the point of impact along the wall (in case the impact takes place) are randomized. In case the randomized position of impact coincides with a water-tight opening (door or window), the resultant force is translated to boundaries of the opening.

5.4.2.3 The structural modeling

Alternative structural analysis procedures for calculating the structural response to flooding actions can be found in the literature. In this section, some these procedures are outlined.

The arching analysis [19], based on the identification of compression iso-static lines, is generally used to study the out of plane response of well-confined masonry panels. This type of analysis is not suitable when there are openings in the wall panel.

An alternative approach is based on elastic analysis of mono-dimensional [20] or bi-dimensional elements [21], up to the formation of the first crack. In the first case, the bearing structure is modeled through a mono-dimensional element representative of a generic column or of a strip of a wall. Rigid end-zones might also be used to model the zone of higher stiffness concentration (intersection with other elements). In the second case the walls can be modeled through shell elements with specific boundary restraints (on one or more sides). In both cases, closed-form solutions exist for the internal stresses. However the modeling is very simplistic, because the openings are neglected. Nevertheless, the internal stress solutions can become quite

involved for complicated pressure profiles.

The limit analysis [22] can also be applied for modeling of structural response, both to perform mono-dimensional (i.e., the formation of plastic hinges) and also bi-dimensional-analysis (i.e., the yield lines or fracture lines). Strictly speaking, this theory is not appropriate for fragile modes of failure. Nevertheless, it is used for fragile systems, making appropriate assumptions about the failure mechanism [23]. In case of fracture line analysis, it is also possible to take into account the effect of openings.

This work employs an elastic finite element model (FEM) in open-source software OpenSees [24]. Employing FEM provides the possibility of modeling the real geometry of the structure, taking into account the openings and irregularities. The structural models developed herein are consisted of two-dimensional elastic shell finite element panels with openings (considered as voids). Three types of transversal boundary condition restraints are considered: (a) fixed end; (b) hinged; (c) free. For example, if a good transversal connection between two orthogonal walls is verified, wall panel with fixed-end restraints can be used. Based on the uncertain parameters related to the geometrical configuration of the buildings, four different types of structural models are generated. These models are distinguished based on the type, number and relative positioning of openings (door and windows). Figure 5.6 below illustrates various configurations generated in the simulation procedure.

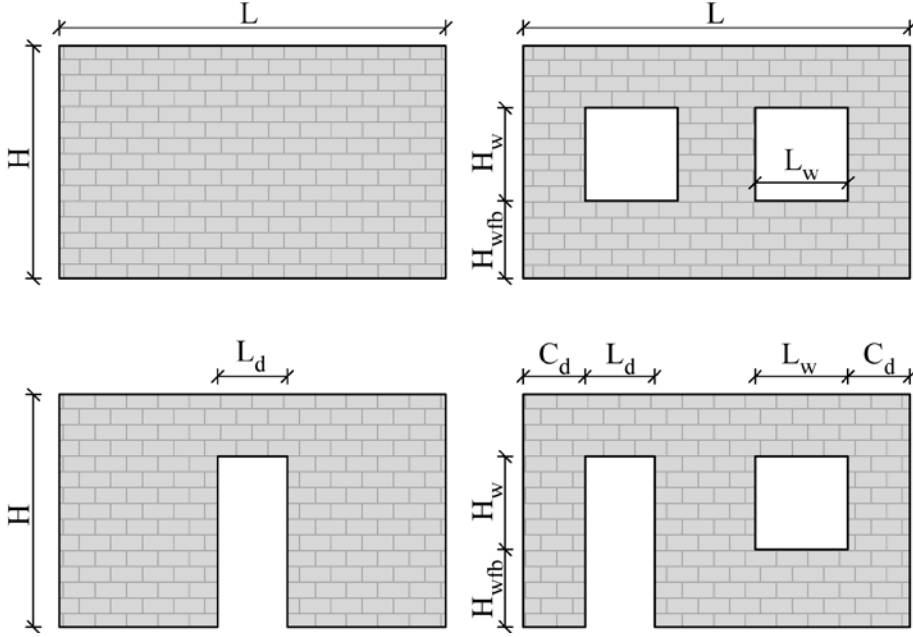


Figure 5.6 - Various structural configurations considered in the analysis (the number of the openings is randomized based on the wall length).

Safety checking: The structural assessments for each (increasing) flooding height considered, consists of checking whether the section force D exceeds the corresponding section capacity C for the critical sections. For all the identified zones of stress concentration (described in detail in the next paragraph) and for each water height level, safety-checking is performed in terms of both shear force and out-of-plane bending moment. It should be noted that safety-checking for bending moment is differentiated with respect to horizontal and vertical sections, due to the presence of axial forces. Denoting the flexural strength of a horizontal section by ($M_{Rd,H}$); the flexural strength of a vertical section by ($M_{Rd,V}$); and the shear strength by (V_{Rd}):

$$V_{Rd} = A_{\text{section}} \cdot \tau_0 \quad (5.8)$$

$$M_{Rd,H} = \frac{N \cdot t}{2} \cdot \left(1 - \frac{N}{0.85 \cdot f_m \cdot A_{\text{section}}} \right) \quad (5.9)$$

$$M_{Rd,V} = \frac{f_{fl} \cdot H_{\text{section}} \cdot t^2}{6} \quad (5.10)$$

where $A_{section}$ is the area of the section/sub-section; $H_{section}$ is the height of the section/sub-section, and N is the axial force acting on the section/sub-section. The formula for shear strength neglects interactions between shear/axial forces. The flexural strength for a horizontal section/sub-section in Eq. (5.9) is calculated assuming that the bending moment strength is reached by exceeding the ultimate compression strength. This is while the flexural strength for a vertical section/sub-section in Eq. (5.10) is calculated by assuming that the out-of-plane bending moment strength is reached by exceeding the ultimate tensile strength.

Calculating the critical demand-to-capacity ratio: An iterative procedure is followed for the identification of the zones high stress concentration by searching through prescribed critical sections. Figure 5.7 below illustrates various critical sections (highlighted) identified in relation to structural configuration and geometry.

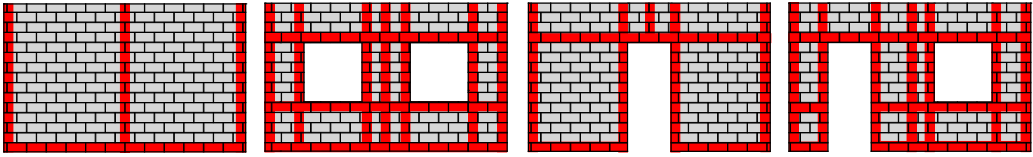


Figure 5.7 - Zones of panel in which is searched the critical section.

Zones of high stress concentration may be verified due to, debris impact, asymmetric boundary conditions, and geometrical configurations/presence of openings. Strictly speaking, local stress concentrations do not necessarily translate into global failure mechanisms; however, – in lieu of more accurate information – they can be considered as precursors to failure for a brittle structure. For each critical section i considered, the zone(s) of high stress concentration are identified by: (a) discretizing in smaller *sub-sections* (e.g., with a discretization step of 25 cm); (b) calculating the demand to capacity ratio (for both flexure and shear), for each sub-section j of the critical section considered, denoted by D_{ji}/C_{ji} . This is done in an exhaustive manner considering all the possible sub-sections; (c) defining the zone(s) of high stress concentration as those having the largest demand to capacity ratio $\max_j D_{ji}/C_{ji}$.

In this manner, it is possible to determine, for each water height level h , the critical demand to capacity ratio as the demand to capacity ratio $Y(h)$ that takes the structure closer to the onset of specified limit state [25]:

$$Y(h) = \max_i \max_j \frac{D_{ji}}{C_{ji}} \quad (5.11)$$

For each Monte Carlo realization of the structural model identified by vector $\underline{\theta}$, a value for the critical water height $h_{cr}(\underline{\theta})$ is obtained, for a given limit state, defined as $Y(h_{cr}(\underline{\theta}))=1$. The dependence of critical water-height on $\underline{\theta}$ is dropped for convenience hereafter.

5.4.2.4 Determining the critical water height

For each limit state considered, the simulation procedure provides a set of critical water height values as described in the previous section.

Serviceability: It is assumed that the serviceability limit state is exceeded if the water infiltrates inside the building. Thus, for each structural model and loading identified by the simulation realization $\underline{\theta}$, the critical water height corresponding to the limit state of serviceability is obtained based on the geometrical configuration (e.g., presence of a barrier or a raised foundation) and the overall water-tightness of the structure (established based on the water-tightness of doors and windows). The schematic table in Figure 5.8 demonstrates the different h_{cr} assigned based on structural configuration and water-tightness. Colored doors and windows are water-tight. Conversely, white doors and windows are not water-tight.

Structural Collapse: For each simulation realization identified by vector of uncertain parameters $\underline{\theta}$, the critical flooding height for the limit state of collapse is determined based on safety-checking in various control sections strategically located in the wall corners or close to the openings (described in detail in previous section). It should be noted that if the structure does not reach the onset of collapse limit state through the incremental flood loading analysis, a *sentinel value* (a large number) is assigned to the critical height. The

schematic table in Figure 5.8 summarizes various situations that may arise for different simulation realizations with the following symbols:

- A. Considering only hydrostatic loading along the height of the structure;
- B. Considering only hydrostatic loading up to the windows' level;
- C. Considering only hydrostatic loading up to the height of the barrier
- D. Assigning a sentinel value (a very large number) as the critical height;
- E. Considering hydrostatic, hydrodynamic and probably debris impact¹¹ actions along the height of the structure;
- F. Considering hydrostatic, hydrodynamic, and eventually debris impact actions up to the height of the windows (for higher elevations the hydrostatic pressure is neglected). Note that the loading on the windows is not considered in this particular case since they are not water-tight (as can be seen in the figure).
- G. Considering only hydrodynamic action (eventually accompanied by debris impact) along the height of the structure, unloading the openings (since they are not water-tight);

¹¹ Recall that debris impact is considered with a given probability described in the section on binary variables.

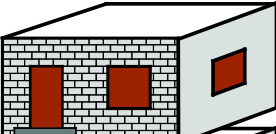
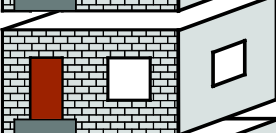
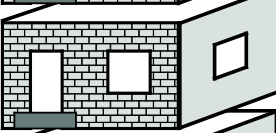
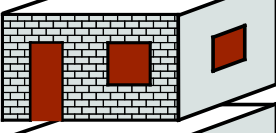
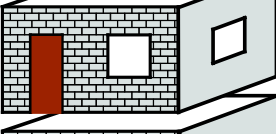
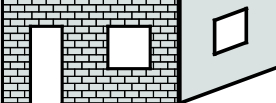
Configuration	Serviceability	Collapse		Life Safety	
		HS	HS+HD	HS	HS+HD
	sentinel value	A	E	$h_{collapse}$	$h_{collapse}$
	$H_{wfb} (+H_f)$	B	F	$\begin{matrix} \min \\ h_{collapse} \\ h_{nominal} \end{matrix}$	$\begin{matrix} \min \\ h_{collapse} \\ h_{nominal} \end{matrix}$
	$H_b (+H_f)$	C	G	$\begin{matrix} \min \\ h_{collapse} \\ h_{nominal} \end{matrix}$	$\begin{matrix} \min \\ h_{collapse} \\ h_{nominal} \end{matrix}$
	sentinel value	A	E	$h_{collapse}$	$h_{collapse}$
	$H_{wfb} (+H_f)$	B	F	$\begin{matrix} \min \\ h_{collapse} \\ h_{nominal} \end{matrix}$	$\begin{matrix} \min \\ h_{collapse} \\ h_{nominal} \end{matrix}$
	$0 (+H_f)$	D	G	$\begin{matrix} \min \\ h_{collapse} \\ h_{nominal} \end{matrix}$	$\begin{matrix} \min \\ h_{collapse} \\ h_{nominal} \end{matrix}$

Figure 5.8 - Evaluation of critical flooding height in various situations corresponding to possible Monte Carlo extractions

Life Safety: As mentioned before, the life safety limit state is a hybrid limit state that combines structural collapse considerations and life-safety considerations due to presence of water. In fact, for each simulation realization identified by vector θ , the critical water height is calculated as the more critical between (i.e., the minimum value) critical value calculated for the limit state of collapse and a prescribed nominal value marking a life-threatening water level inside the building. Figure 5.8 reports the various situations that may arise during the simulation process --as a function of building geometry and water-tight properties.

The nominal life-threatening water height: This nominal value depends on many factors, namely, presence/absence of flood warning systems, building type, community preparedness, flood risk governance, and demographical aspects (e.g., the children and the elderly are more vulnerable). A recent study [2] demonstrates that, for flooding with rapidly rising water level, flooding height of around 1.5 m corresponds to a 50% mortality rate (i.e., 50% of the exposed people risk their life). In this work, a nominal flooding height value of 1m is chosen that, according to the above-mentioned study, corresponds to a mortality rate of about 10%¹².

5.4.3. *The fragility assessment*

The simulation procedure leads to set of critical height values corresponding to each simulation realization. At this stage, one could already construct a fragility curve based on the (empirical) distribution of the critical height values. However, given the many sources of uncertainty present in the vulnerability assessment problem, it is desirable construct an analytic probability model based on the set of critical height values. This probability model would also lead to establishing a plus/minus one standard deviation confidence interval (as a function of the number of simulations) around the expected value of plausible analytic fragility curves called herein as *robust fragility curve* [26, 27]. In the following, the various steps leading to the estimation of robust fragility curves are described.

5.4.3.1 *The analytical fragility curve*

For each limit state considered, the simulation procedure provides a set of critical water height values as described in the previous section. These critical water height values are used then as data in order to calculate, using Bayesian parameter estimation [28], the posterior probability distribution for

¹² Assuming that an informal settlement is likely to have poor flooding emergency preparedness. This assumption is validated to a large degree for the zone of the case-study.

the parameters of prescribed analytic fragility functions. Finally, the robust fragility [26, 27] is calculated as the expected fragility based on the posterior probability distribution calculated for the parameters of the prescribed analytic fragility functions. Note that this posterior probability distribution can be interpreted as degrees of belief in the analytic fragility model that is defined based on a specific set of parameters. Three analytical fragility models are adopted herein, corresponding to each of the three limit states considered:

$$(SE) \quad F(h_f | \pi_0, \eta_{SE}, \beta_{SE}) = P(h_{SE} \leq h_f) = \pi_0 \cdot \Phi\left(\frac{\ln \frac{h_f}{\eta_{SE}}}{\beta_{SE}}\right) + (1 - \pi_0) \cdot I_0(h_f) \quad (5.12)$$

$$(CO) \quad F(h_f | \eta_{CO}, \beta_{CO}) = P(h_{CO} \leq h_f) = \Phi\left(\frac{\ln \frac{h_f}{\eta_{CO}}}{\beta_{CO}}\right) \quad (5.13)$$

$$(SL) \quad F(h_f | \pi, \eta_{SL}, \beta_{SL}) = P(h_{SL} \leq h_f) = \pi \cdot \Phi\left(\frac{\ln \frac{h_f}{\eta_{SL}}}{\beta_{SL}}\right) + (1 - \pi) \cdot I(h_f) \quad (5.14)$$

where parameters π_0 , η_{SE} and β_{SE} reported after the conditioning sign ($|$) are the three parameters that define the analytic probability distribution/fragility function for the serviceability (SE) limit state; $1 - \pi_0$ is the probability that the serviceability critical height is equal to zero; η_{SE} and β_{SE} are median and logarithmic standard deviation for the critical water height given that the critical water height is greater than zero for (SE). Meanwhile, for the collapse (CO) limit state, only two parameters denoted by η_{CO} and β_{CO} are defined as the median and logarithmic standard deviation for the critical water height, respectively. $1 - \pi$ is the probability that the life safety (LS) critical water height is equal to a nominal prescribed value; η_{SL} and β_{SL} are respectively the median and the logarithmic standard deviation for the critical water height given that the critical water height is assigned nominally; $\Phi(\cdot)$ denotes the standard

Gaussian (Normal) cumulative probability distribution and $I_0(h_f)$ and $I(h_f)$ are index functions defined as follows:

$$(SE) \quad I_0(h_f) = \begin{cases} 0 & \text{if } h_f = 0 \\ 1 & \text{if } h_f > 0 \end{cases} \quad (5.15)$$

$$(LS) \quad I(h_f) = \begin{cases} 0 & \text{if } h_f \leq h_{nominal}(LS) \\ 1 & \text{if } h_f > h_{nominal}(LS) \end{cases} \quad (5.16)$$

where $I_0(h_f)$ and $I(h_f)$ depict two step functions identified respectively by zero (Figure 5.9a) and the nominal water height ($h_{nominal}(LS)$) (Figure 5.9d). Note that the derivative I functions is equal to the Dirac delta function at $h=0$ and $h=h_{nominal}(LS)$.

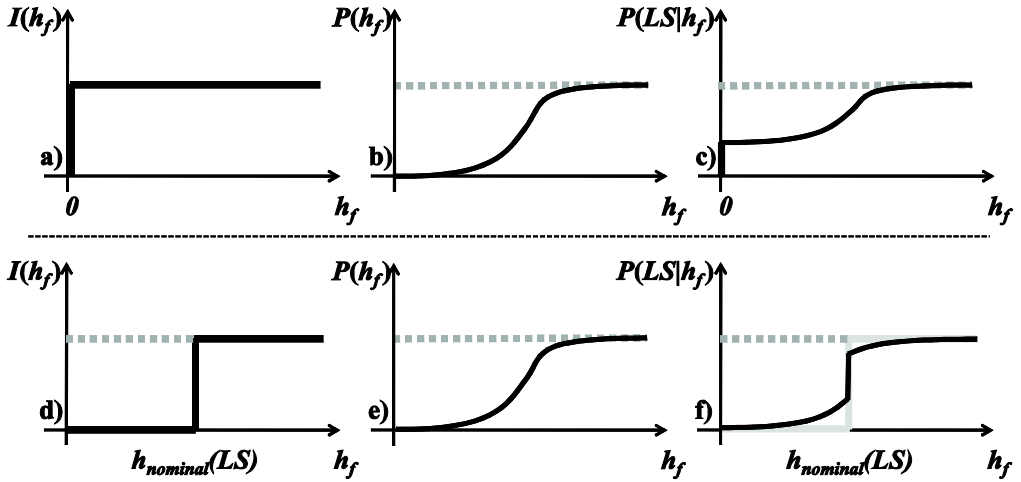


Figure 5.9 - schematic diagrams of: a) step function for SE; b) the Lognormal CDF for SE; c) the three-parameter CDF for SE; d) step function for LS; e) the Lognormal CDF for SL; f) the three-parameter CDF for SL

The analytical fragility model proposed in Eq. (5.12) and Eq. (5.14) can be interpreted as an application of the total probability theorem [29] on the two mutually exclusive outcomes marked by probabilities π_0 and π . The probability distributions in Eqs. (5.12) and (5.14) are also known as the *three-parameter* distributions [29, 30] which are bi-modal probability density functions

(PDF)/cumulative distribution functions (CDF) expressed as a linear combination of a Lognormal PDF/CDF and a Dirac delta function/step function. In particular, the three-parameter cumulative distribution function expressed in Eq. (5.12) and illustrated in Figure 5.9 (c) is a linear combination (with weight π_0) of the step function $I_0(h_f)$ depicted in Figure 5.9 (a) and the Lognormal CDF depicted in Figure 5.9 (b). In a similar manner, the three-parameter cumulative distribution function expressed in Eq. (5.14) and illustrated in Figure 5.9 (f) is a linear combination (with weight π) of the step function $I(h_f)$ depicted in Figure 5.9 (d) and the Lognormal CDF depicted in Figure 5.9 (e).

5.4.3.2 Updating analytical fragility parameters

Denoting the parameters of the analytic fragility function as $\chi = [\eta, \beta]$ for the collapse limit state and $\chi = [\pi, \eta, \beta]$ for the other two limit states, the joint probability distribution for the vector of parameters χ can be denoted as $p(\chi)$. Using Bayesian updating, the probability distribution $p(\chi)$ for the parameters of the fragility function can be updated using formulas described in [28] based on the set of critical height values obtained from simulation. The updated probability distribution can be denoted as $p(\chi | \mathbf{H}_c)$ where \mathbf{H}_c is the vector of n critical height values obtained through n simulations. Below, the Bayesian updating procedure used for updating the parameters of the three-parameter distribution (used for limit states SE and LS) is described. The bi-parametric updating procedure for the CO limit state can be considered a special case.

Assuming independence between the pair (η, β) and π , the term $p(\chi | \mathbf{H}_c)$, can be written as:

$$p(\chi | \mathbf{H}_c) = p(\eta, \beta | \mathbf{H}_c) \cdot p(\pi | \mathbf{H}_c) \quad (5.17)$$

where $p(\eta, \beta | \mathbf{H}_c)$ denotes the joint probability density distribution for parameters η and β given the vector of critical height values \mathbf{H}_c , and can be written as [28]:

$$p(\eta, \beta | \mathbf{H}_c) = k \beta_{\mathbf{H}_c}^{-(n+1)} \cdot \exp \left[-\frac{\nu s^2 + n \left(\log \eta_{\mathbf{H}_c} - \overline{\log \mathbf{H}_c} \right)^2}{2 \beta_{\mathbf{H}_c}^2} \right] \quad (5.18)$$

where k is a normalization factor; n is the number of simulations; $\nu=n-1$ is the degree of freedom; $\overline{\log \mathbf{H}_c}$ is the sample average for $\log \mathbf{H}_c$, and νs^2 is sum of the squares of the residuals calculated based on the sample average value.

The term $p(\pi | \mathbf{H}_c)$ can be calculated from the complete-Beta function represented in Eq. (5.2), replacing n by the number of simulations and r by the number of simulations in which the critical height value is not assigned nominally.

5.4.3.3 The robust fragilities

Finally, the robust fragility is calculated as the expected value of the analytic function $F(h_f | \chi)$ in Eq. (5.12), Eq. (5.13) or Eq. (5.14), over the entire domain of vector χ and according to the updated joint probability distribution $p(\chi | \mathbf{H}_c)$:

$$F(h_f | \mathbf{H}_c) = E[F(h_f | \chi)] = \int_{\Omega} F(h_f | \chi) \cdot p(\chi | \mathbf{H}_c) \cdot d\chi \quad (5.19)$$

where $E[.]$ is the expected value operator and Ω is the domain of the vector χ . The variance σ^2 in fragility estimation can be calculated as:

$$\sigma^2[F(h_f | \chi)] = E[F(h_f | \chi)^2] - E[F(h_f | \chi)]^2 \quad (5.20)$$

where $E[F(h_f | \chi)]^2$ can be calculated from Eq. (5.19) replacing $F(h_f | \chi)$ with $F(h_f | \chi)^2$.

Simulation-based calculation of the robust fragility: Monte Carlo simulation can also be used for calculating the robust fragility from integral in Equation

(5.19). This consists of generating N various realizations of vector χ based on the posterior probability distribution $p(\chi|\mathbf{H}_c)$. This leads to generation of N plausible fragility curves. The statistics of these curves (e.g., mean, standard deviation, various percentiles) can then be calculated from the generated fragility curves. In particular, the 16%, 50% (median), and 84% fragility curves can be obtained this way. Hereafter, the 16%, 50% and 84/ fragility curves are going to be referred to as the *robust fragility curves*.

Simulating χ based on its probability distribution $p(\chi|\mathbf{H}_c)$, assuming independence between the couple (η, β) and π , entails separate simulation of (η, β) and π . In order to simulate the pair (η, β) according to its distribution $p(\eta, \beta|\mathbf{H}_c)$, β is first simulated from its marginal distribution $p(\beta|\mathbf{H}_c)$:

$$p(\beta|\mathbf{H}_c) = k' \beta_{H_c}^{-(\nu+1)} \cdot \exp\left[-\frac{\nu s^2}{2\beta_{H_c}^2}\right] \quad (5.21)$$

Conditioning on the simulated value β , η is then simulated based on the conditional probability density function $p(\eta|\beta, \mathbf{H}_c)$:

$$p(\eta|\beta, \mathbf{H}_c) = \frac{1}{\eta} \cdot \left(\frac{2\pi \cdot \beta_{H_c}^2}{n}\right)^{-0.5} \cdot \exp\left[-\frac{n}{2\beta_{H_c}^2} \cdot \left(\log \eta_{H_c} - \overline{\log \mathbf{H}_c}\right)^2\right] \quad (5.22)$$

As mentioned above, π can be simulated from its marginal distribution (Equation 5.2).

5.5 Application: the case of Suna, Dar es Salaam

The probability-based methodology presented in this chapter for vulnerability assessment for a class of structure is applied to a portfolio of informal settlements located in Suna Subward, Dar es Salaam City. The informal settlements located in this neighborhood reveal similar characteristics. For instance, they are all one-storey buildings, use cement stabilized bricks as wall material, and have a roof system made up of corrugated iron sheets and wooden/iron beams. Moreover, the houses in this neighborhood, have similar geometrical patterns (the so-called Mozambique-style housing). As common adapting strategies, a significant portion of the inhabitants tend to build a barrier in front of the door or to build the house on a raised foundation (platform). The windows and doors are generally not water-tight.

5.5.1. *Data acquisition*

The portfolio of informal settlements in Suna is identified by overlaying the map of the case-study areas with flood profiles depicted in Figure 3.5. The GIS-based boundary recognition procedure (described in Chapter 2) provides the plan dimensions for each building in the portfolio of buildings considered. A sample field survey on 100 buildings is conducted by the Institute of Human Settlements Studies (IHSS), Ardhi University, Dar es Salaam. It can be observed that buildings have more-or-less similar characteristics in terms of construction material used for walls and roof. Almost all of the buildings seem to constructed with 460x230x125 mm cement blocks; wooden or iron beams are used as roof beams covered by corrugated iron sheets. Moreover, the blocks are systematically placed in such a way that the wall thickness observed throughout the surveyed buildings is around 140 mm (including the width of the plaster, if present). Two types of doors have been used in the area, wooden doors and iron doors. While the former seem to be quite ineffective in preventing infiltrations, the latter seems to be able to prevent water-seepage. In general, given the warm climate, the windows are without glass and are

covered by wired net or sheets of plastic which seem quite ineffective in preventing infiltrations. As adaptation strategies, the use of cement barriers or cement raised foundation/platforms can be identified.

The material mechanical properties are based on existing literature for cement hollow bricks with a voids percentage between 45% and 65% are reported in Table 5.4

Material Type	f_m		τ_0		E		G		γ (kN/m ³)
	(MPa)		(MPa)		(MPa)		(MPa)		
	Min - Max		Min - Max		Min - Max		Min - Max		
Hollow space 45% - 65%	1.5	2.0	0.095	0.12	1200	1600	300	400	12
Hollow space < 45%	3.0	4.4	0.18	0.24	2400	3520	600	880	14

Table 5.4 - Cement stabilized blocks available in literature [31]

5.5.2. The characterization of uncertainties

Discrete binary uncertain variables/logic statements: Table 5.5 reports the list of discrete binary uncertain variables/logic statements considered and the related input of the procedure. Examples of the uncertain binary variables considered are, presence of a raised foundation or presence of a platform (*PI*), presence of a barrier (*Ba*), water-tightness of the door (*DS*), water-tightness of the windows (*WS*), and presence of a visual degradation in the building. It can be noted that also the presence of openings in the model wall panel is randomized. This is due to fact that for the procedure, the specific building wall hit first by the flood (and its angle) are assumed to be unknown. The vulnerability assessment module uses the logic-tree approach in order to propagate the uncertainties in discrete binary uncertain variables listed in Table 5.5. One of the advantages of organizing the binary variables in a logic-tree is the possibility to define the correlation between various uncertain variables. Such correlation structure can be observed in the way the survey data is progressively classified in Table 5.5 below.

n° OF SURVEYED BUILDINGS	100
n° of buildings with visual degrading DG	0
n° of buildings with <i>Pl</i>	30
n° of buildings with <i>Ba</i> given <i>Pl</i>	10
n° of buildings with <i>Ba</i> given not <i>Pl</i>	50
n° of buildings with <i>DS</i> given <i>Pl</i> and <i>Ba</i>	5
n° of buildings with <i>DS</i> given <i>Pl</i> and not <i>Ba</i>	15
n° of buildings with <i>DS</i> given not <i>Pl</i> and <i>Ba</i>	30
n° of buildings with <i>DS</i> given not <i>Pl</i> , not <i>Ba</i>	8
n° of buildings with <i>WS</i> given <i>Pl</i> , <i>Ba</i> , and <i>DS</i>	2
n° of buildings with <i>WS</i> given <i>Pl</i> , not <i>Ba</i> , and <i>DS</i>	5
n° of buildings with <i>WS</i> given not <i>Pl</i> , <i>Ba</i> , and <i>DS</i>	10
n° of buildings with <i>WS</i> given not <i>Pl</i> , not <i>Ba</i> , and <i>DS</i>	3
n° OF SURVEYED WALLS	400
n° of walls with <i>D</i>	100
n° of walls with <i>W</i> given <i>D</i>	80
n° of walls with <i>W</i> given not <i>D</i>	200

Table 5.5 - Structural detailing parameters expressed as discrete binary uncertain variables

Estimating the logic-tree probabilities/degrees of belief: The probability π that each logical statement reported in Table 5.5 is TRUE can be calculated from the complete-Beta function in Equation (5.2), based on n field survey sheets (r is the number of survey sheets for which the binary variable/logical statement in question is TRUE). These probability/degrees of belief are going to be used next in the simulation routine. As much as it regards the estimation of π , there are three possibilities: a) using the mode of the distribution in Eq. (5.24): $\pi = r/n$; b) using the expected value $\pi = (r+1)/(n+2)$, or c) sampling directly from the probability distribution.

For instance, Figure 5.10 below shows the probability of having the raised platform, according to the data shown in Table 5.5.

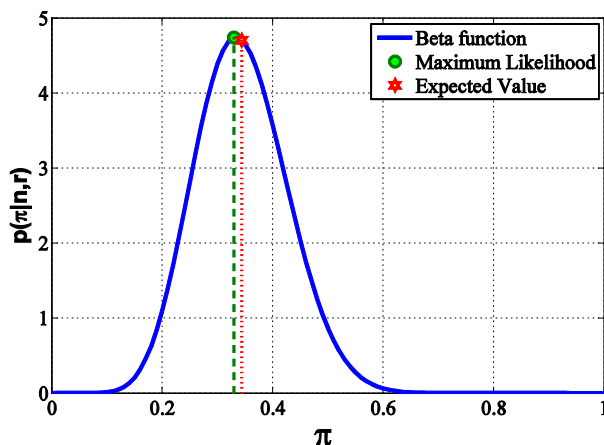


Figure 5.10 - Three alternative possibilities for estimating the probability that the building has a raised platform: the entire distribution, the maximum likelihood estimate and the expected value

Continuous uncertain variables: Table 5.6, Table 5.7 and Table 5.8 list the continuous uncertain variables considered. It can be observed that the continuous variables considered can be classified into two categories: (1) parameters related to the building geometry; (2) parameters related to the mechanical material properties; (3) parameters related to the modeling of flood action.

Geometrical property	Distribution type	Mean	Standard Deviation
		Min	Max
L (m) - wall length	Normal	11.17	3.39
H (m) - wall height	Uniform	2.50	3.50
t (m) - wall thickness	deterministic	0.125	0.00
L_w (m) - window length	Uniform	0.80	1.20
H_w (m) - window height	Uniform	0.80	1.00
H_{wfb} (m) - window rise	Uniform	0.80	1.20
L_d (m) - door length	Uniform	0.80	1.20
C_d (m) - corner length	Uniform	0.80	0.90
H_f (m) - foundation rise	Normal	0.45	0.15
H_b (m) - barrier height	Uniform	0.10	1.00

Table 5.6 - Continuous uncertain parameters related to building geometry

In lieu of case-specific laboratory tests, existing literature results is used for the mechanical properties of cement-stabilized bricks. No correlation among the parameters has been considered. Uniform distribution is used when data is available only on the range of a variable (i.e., a lower and an upper bound). Wall thickness is assumed to be deterministic and equal to the thickness of the cement bricks (125mm). The parameters of the Normal probability distributions for the height of the raised platform or the barrier are obtained based on the histogram of the observed data from the survey results.

Mechanical properties	Distribution type	Mean Min	Standard Deviation Max
f_m (MPa) - compression strength	Uniform	1.50	2.00
τ_0 (MPa) - shear strength	Uniform	0.095	0.12
f_{β} (MPa) - flexural strength	Uniform	0.14	0.40
E (MPa) - linear elastic modulus	Uniform	1200	1600
G (MPa) - shear elastic modulus	Uniform	500	667
γ (kN/m ³) - self weight	Uniform	11	13

Table 5.7 - Continuous uncertain parameters related to material mechanical properties (cement-stabilized bricks)

Loading parameter	Distribution type	Median	Standard Deviation
b	Lognormal	1.57	0.54
a	Fully correlated with $b^{(13)}$		

Table 5.8 - Continuous uncertain parameters related to loading parameters

5.5.3. Preliminary analysis results

Before showing the results of the complete simulation procedure, the fragility curves for the four wall typologies/configurations taken into account

¹³ b is sampled from a marginal probability distribution fitted to various (a, b) data pairs calculated based on the inundation profile. Therefore, after simulating b from its probability distribution, the closest (a, b) pair is taken.

in this thesis are demonstrated in this section. For each wall typology (i.e., without openings, with windows and doors, with only windows, and with only a door) and given that the building is sufficiently water-tight, all other uncertain variable in the vector θ are simulated based on $n=50$ Monte Carlo simulations. The resulting fragility curves for the limit state of collapse are then calculated based on different wall boundary conditions and flood loading combinations.

In Figure 5.11, the fragility curves for the collapse limit state, for the above-mentioned four wall typologies are plotted. The wall boundary conditions correspond to good foundation-wall connection (fixed-end) and moderate transversal connection with the other walls (hinged). Three different loading combination are taken into account: hydrostatic (HS), hydrostatic and hydrodynamic (HS+HD) and hydrodynamic with debris impact (HS+HD+DI), plotted as, blue solid line, red dashed line and green dotted line, respectively.

For the case study area, flooding velocity is not so high as to influence the structural response. Therefore, the fragility curves for the hydrostatic only and hydrostatic plus hydrodynamic loads are quite similar. This is due the fact that the flooding height/velocity relationship for most of points in Suna, resemble points P1 and P3 shown in Figure 3.4 in Chapter 3. To have a significant difference between the loading combinations HS and HS+HD, the height/velocity relationship should resemble point P2.

It can be observed that debris impact leads to significantly higher fragility values, in the presence of openings. However, for a solid wall with no openings, the three loading combinations lead to similar fragility values. The presence of openings seems to have undesirable effects on structural performance due to both local stress concentrations close to the openings and also eventual reduction in the resisting section.

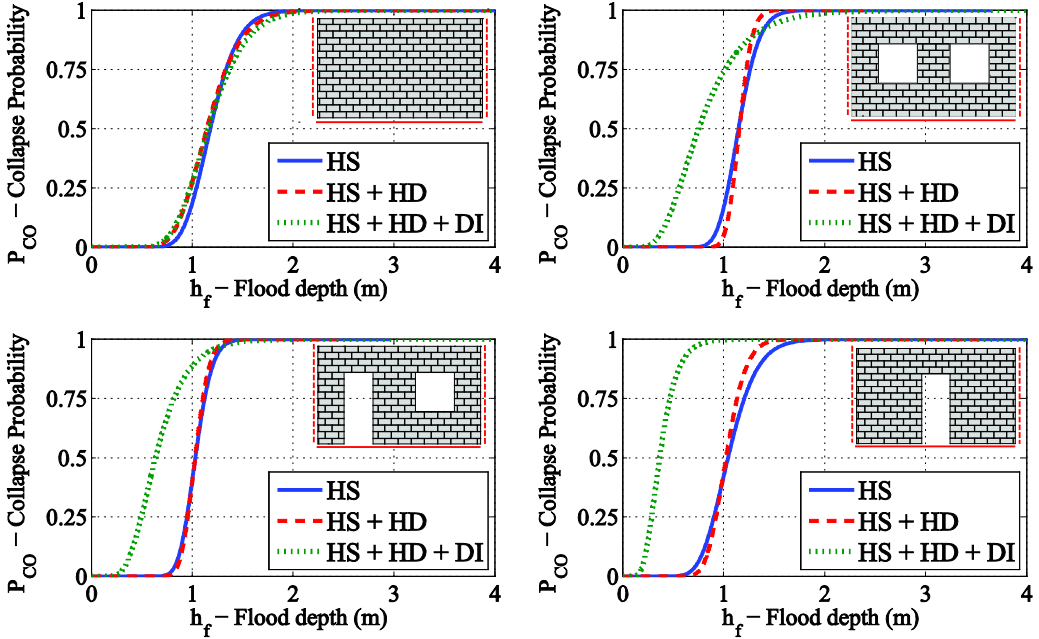


Figure 5.11 - Fragility curves for the four wall typologies and three loading combinations: hinged on the sides

In Figure 5.12 the fragility curves for the same four wall typologies and three loading combination are demonstrated; the only difference is that the walls are modeled as fixed on the sides. Overall, the trend in the fragility curves is very similar to Figure 5.11. However, the fragility values are higher with respect to the corresponding cases with hinged sides. This can be justified by hypothetically higher stress concentration around the restrained sides. Since in the case study area (Suna), the transverse connection between the walls does not seem satisfactory, the hinged assumption (Figure 5.11) seems more plausible.

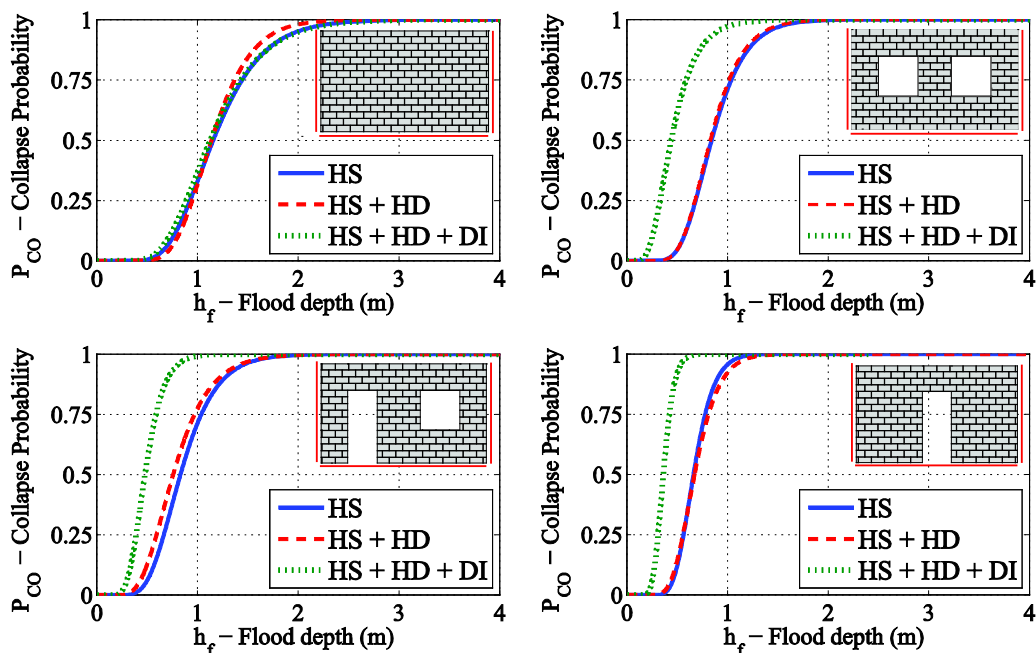


Figure 5.12 - Fragility curves for the four wall typologies and three loading combinations: fixed in the sides

In order to demonstrate the potential significance of the hydrodynamic loading, fragility curves for the same wall configurations (with hinged sides) and loading combinations as above are plotted in Figure 5.13, for flooding height/velocity relation similar to point P2 in Figure 3.4. It can be observed that in this situation, the fragility curves corresponding to HS+HD and HS+HD+DI are quite similar.

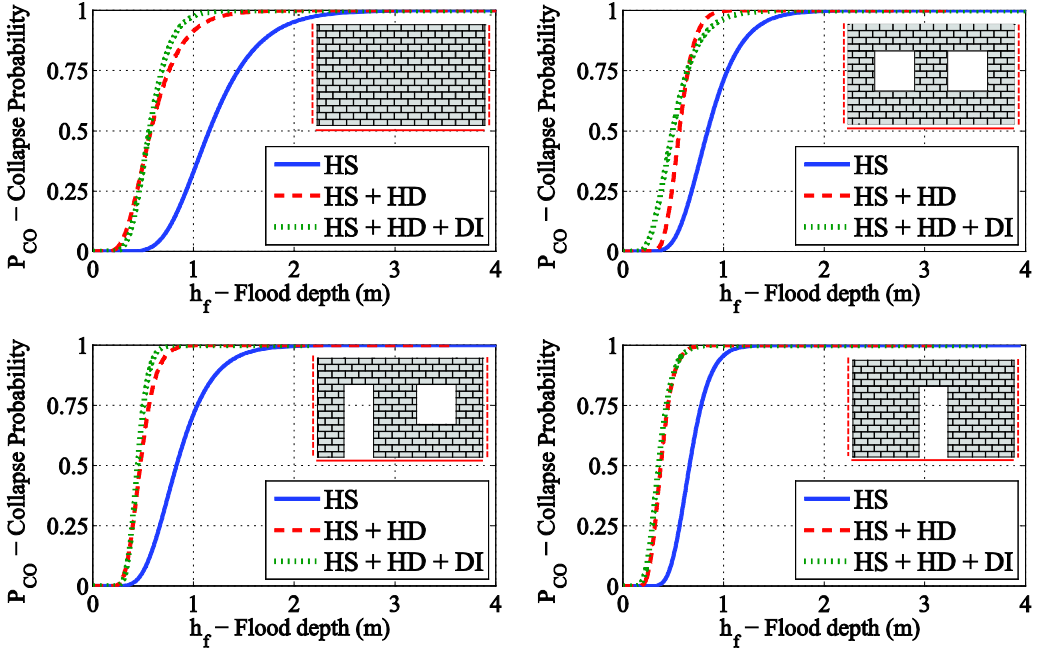


Figure 5.13 - Fragility curves for the four wall typologies and three loading combinations: hinged on the sides, considering the flooding height/velocity relationship similar to point P2 in Figure 3.4

5.5.4. Numerical results

In this section, the robust fragility curves for the three limit states SE, CO and SL are discussed. These fragility curves are calculated by following the full simulation procedure based on the vector of uncertain parameters θ , reported in Table 5.5, Table 5.6, Table 5.7 and Table 5.8. The probabilities/degrees of belief associated to the binary uncertain parameters/logic statements are both estimated as the maximum likelihood and also sampled directly from the corresponding probability distribution (as in Equation 5.2).

Maximum likelihood estimate: The robust fragility curves for the three limit states in question are calculated based on 20 extractions. The percentile fragility curves are calculated by using the simulation-based procedure described in Section 5.4.3.3. The thin gray curves are 100 simulated plausible fragility curves; the thick red line is the median fragility; and the thick dashed

black curves are the 16th and 84th percentile fragility curves, respectively.

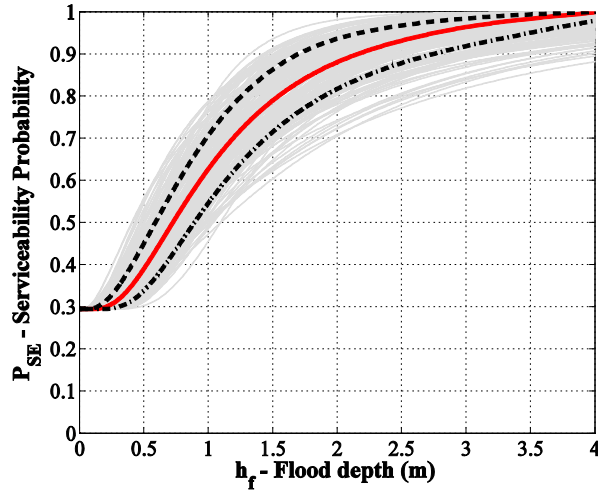


Figure 5.14 - The robust fragility curves (SE)

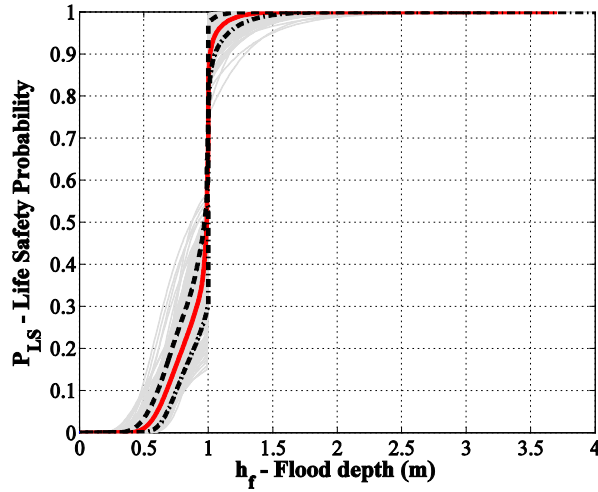


Figure 5.15 - The robust fragility curves (LS)

In Figure 5.16, the robust fragility curves for the limit state of collapse are shown. Moreover, the empirical CDF obtained based on 200 simulations (the blue jagged curve) is also plotted. It can be observed that the empirical fragility based on 200 simulations is well-contained by the 16th-84th percentile

fragilities based on 20 simulations.

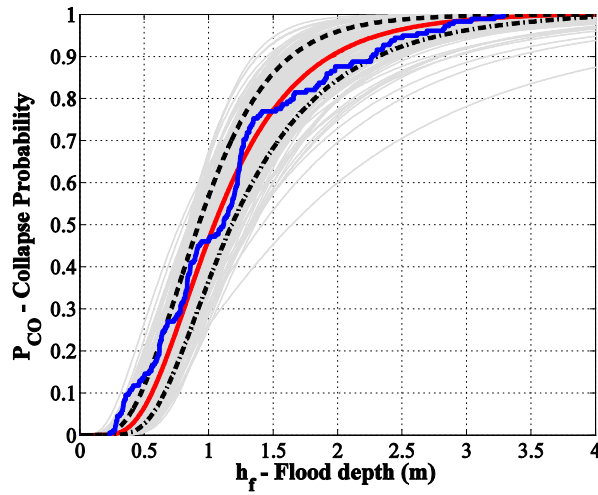


Figure 5.16 - The robust fragility curves (20 simulations) and the empirical fragility curve calculated based on 200 simulations (CO)

Simulating from the entire distribution: The robust fragility curves for the three limit states defined before obtained based on 20 extractions are shown in the following. The resulting fragility curves (represented by thin grey, thick red and thick dashed black lines) are defined in the previous paragraph.

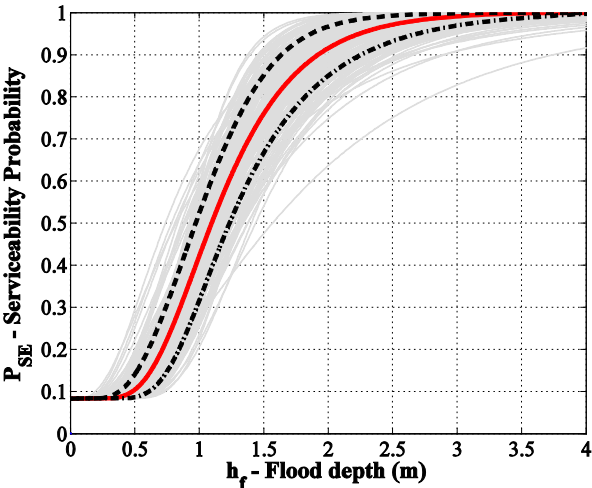


Figure 5.17 - The robust fragility curves (SE): sampling from the full distribution

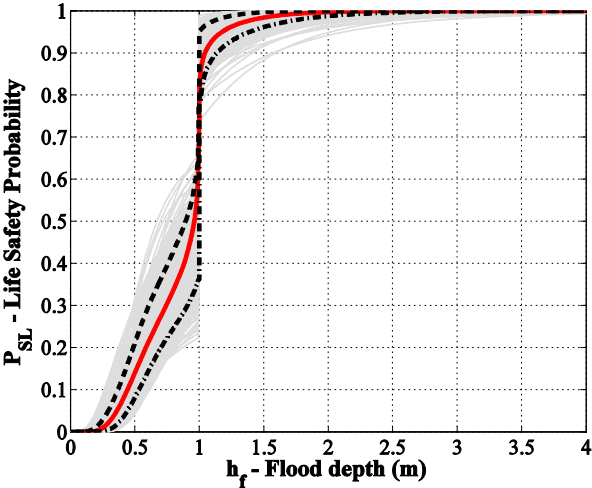


Figure 5.18 - The robust fragility curves (SL): sampling from the full distribution

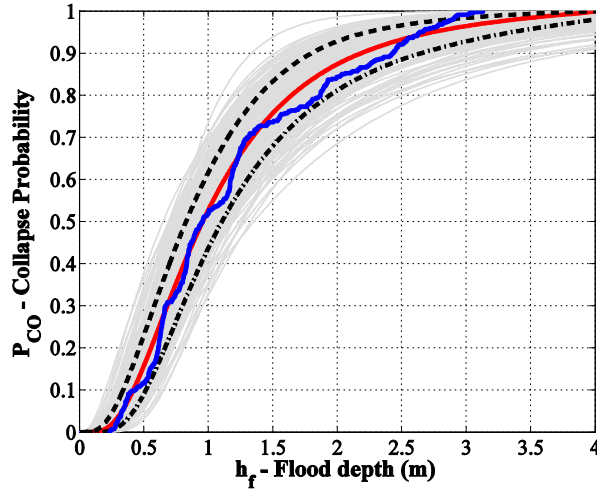


Figure 5.19 - The robust fragility curves (sampling from the full distribution, 20 extractions) and the empirical fragility curve calculated based on 200 simulations (CO)

In Figure 5.20, it can be observed that the fragility curves obtained by sampling the probabilities from the entire distribution have larger dispersion with respect to those calculated based on the maximum likelihood estimates for collapse and life safety limit states. It should be noted that the initial step in the fragility curves for serviceability in Figure 5.20(a) represent roughly the percentage of simulations for which the critical water height is equal to zero (i.e., combination of no raised platform, no barrier, and wooden non water-tight doors). This percentage can be highly sensitive to the number of simulations (compare for example Figures 5.20(a) and Figure 5.21, the only difference is the number of extractions). Therefore, the fragility curve for serviceability should be ideally calculated with a large number of simulations. This is feasible, considering that the critical height values for serviceability are "assigned" (not calculated by structural analysis) based on structural configuration and water-tight properties.

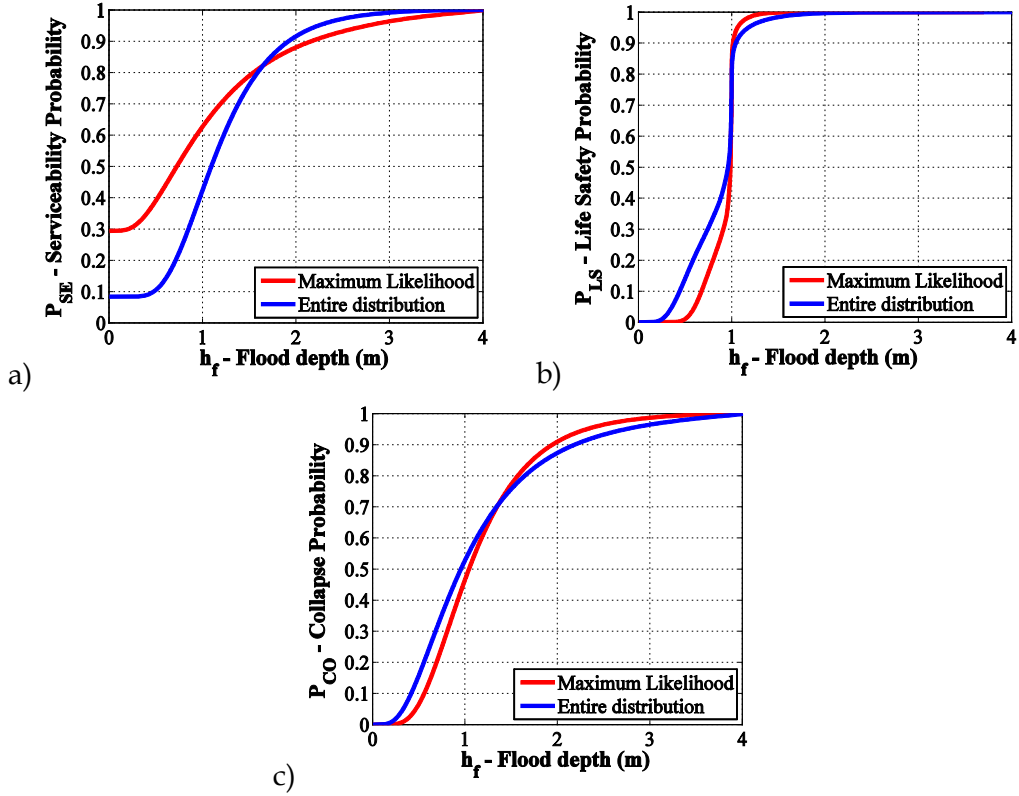


Figure 5.20 - Overlay of the median fragilities for the three limit states considered for the two typology of extraction

In order to study the effect of number of simulations, the robust fragility curves for the three limit states in question, are obtained based on 50 extractions, by sampling the probability values (for the binary variable) directly from their probability distributions. The results are plotted in Figure 5.21, Figure 5.22 and Figure 5.23.

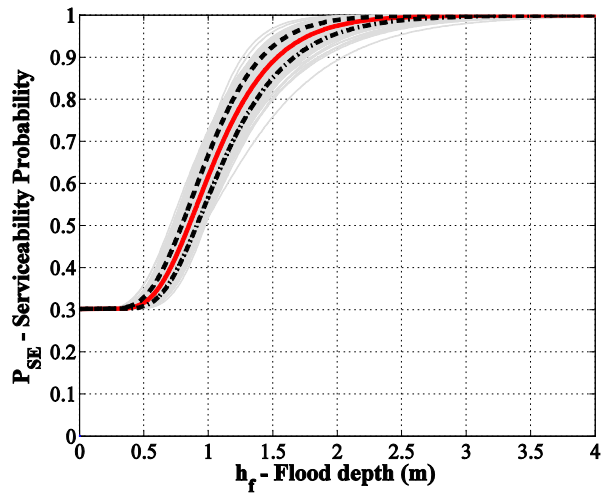


Figure 5.21 - The robust fragility curves (SE): sampling from the full distribution, 50 extractions

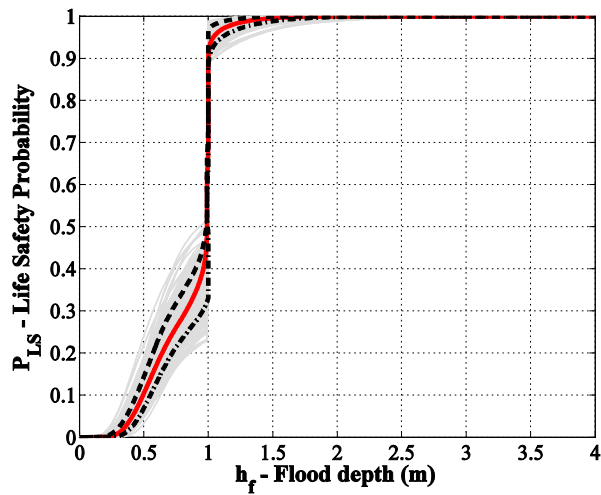


Figure 5.22 - The robust fragility curves (SL): sampling from the full distribution, 50 extraction

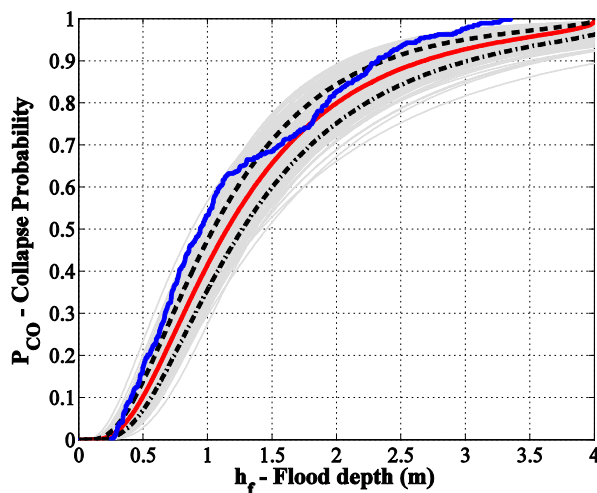


Figure 5.23 - The robust fragility curves (sampling from the full distribution, 50 extractions) and the empirical fragility curve calculated based on 500 simulations (CO)

In Figure 5.23 for the collapse limit state, the empirical fragility curve (blue jagged line) is obtained based on 500 simulations. It can be observed that the simulated (plausible) fragility curves are less dispersed (with respect to the previous case with 20 extractions) and manage to capture the fragility curve obtained based on 500 simulations. This is interesting since the simulated curves (grey lines) are obtained (easily and quickly) by sampling from the updated probability distribution $p(\chi|H_c)$ (Equations 5.21 and 5.22). Meanwhile, obtaining the empirical fragility curve based on 500 simulation is quite time-consuming and involves 500 times the number of water height levels finite element structural analyses --around 10 times the number of analyses for the robust fragility curves in this case.

References

1. Dutta D. and Tingsanchali T., *Development of loss functions for urban flood risk analysis in Bangkok*, in *2nd International Conference on New Technologies for Urban Safety in Mega Cities of Asia*. 2003: University of Tokyo, Japan. p. 229-238.
2. Jonkman S.N., Vrijling J.K., and Vrouwenvelder A.C.W.M., *Methods for the estimation of loss of life due to floods: a literature review and a proposal for a new method*. *Natural Hazards*, 2008. **46**: p. 353-389.
3. Pistrika A., *Flood Damage Estimation based on Flood Simulation Scenarios and a GIS Platform*, in *EWRA 7th International Conference "Water Resources Conseroancy and Risk Reduction Under Climatic Instability"*. 2009: Limassol, Cyprus. p. 419-427.
4. Pistrika A. and Tsakiris G., *Flood risk assessment: A methodological framework*, in *Water Resources Management: New Approaches and Technologies*. European Water Resources Association, Chania, Crete-Greece. 2007.
5. Pistrika A.K. and Jonkman S.N., *Damage to residential buildings due to flooding of New Orleans after hurricane Katrina*. *Natural Hazards*, 2009. **54**: p. 413-434.
6. Smith D., *Flood damage estimation- A review of urban stage-damage curves and loss functions*. *Water S. A.*, 1994. **20**(3): p. 231-238.
7. Chang L., Kang J., and Su M., *Depth-Damage Curve for Flood Damage Assessments Industrial and Commercial Sectors*, in *4th IASME/WSEAS Int. Conference on Water resources, Hydraulics & Hydrology*. 2009: Cambridge, UK.
8. Kang J., Su M., and Chang L., *Loss functions and framework for regional flood damage estimation in residential area*. *Journal of Marine Science and Technology*, 2005. **13**(3): p. 193-199.
9. Schwarz J. and Maiwald H., *Empirical vulnerability assessment and damage for description natural hazards following the principles of modern macroseismic scales*, in *14th WCEE - World Conference of Earthquake Engineering*. 2012: Lisboa, Portugal.
10. Schwarz J. and Maiwald H., *Damage and loss prediction model based on the vulnerability of building types*, in *4th International symposium of Flood Defence*. 2008: Toronto, Canada.
11. Kelman I., *Ph.D Thesis: Physical flood vulnerability of residential properties in coastal, eastern England*. 2002, University of Cambridge.
12. Nadal N.C., Zapata R.E., Pagán I., López R., and Agudelo J., *Building damage due to riverine and coastal floods*. *Journal of Water Resources Planning and Management*, 2009. **136**(3): p. 327-336.
13. Black R.D., *Flood proofing rural residences*. 1975: Department of Agricultural Engineering, Cornell University.
14. Faber M.H., *Statistics and Probability Theory: In Pursuit of Engineering Decision Support*. Vol. 18. 2012: Springer.
15. Jaynes E.T., *Probability theory: The logic of science*. 2003: Cambridge university press.
16. Kelman I. and Spence R., *An overview of flood actions on buildings*. *Engineering Geology*, 2004. **73**(3): p. 297-309.

17. Roos W., Waarts P., and Vrouwenvelder A., *Damage to buildings*. Delft Cluster paper, 2003.
18. FEMA, *Manual Coastal Construction*. 2000, Federal Emergency Management Agency: Washington, D.C.
19. McDowell E.L., McKee K.E., and Sevin E., *Arching action theory of masonry walls*. J. Struct. Div, 1956. **82**(2): p. 915.
20. Timoshenko S. and Young D.H., *Engineering Mechanics*. 4th ed. 1956: McGraw-Hill.
21. Timoshenko S. and Woinowsky-Krieger S., *Theory of plates and shells*. 2nd ed. 1959: McGraw-Hill.
22. Massonnet C.E., Olszak W., and Phillips A., *Plasticity in structural engineering: fundamentals and applications*. 1979: Springer.
23. Martini K. *Finite element studies in the two-way out-of-plane failure of unreinforced masonry*. in *Proceedings of the 6th National Conference on Earthquake Engineering*. 1998. Seattle, Washington.
24. McKenna F., Fenves G., and Scott M., *OpenSees: Open system for earthquake engineering simulation*. Pacific Earthquake Engineering Center, University of California, Berkeley, CA., <http://opensees.berkeley.edu>, 2006.
25. Jalayer F., Franchin P., and Pinto P., *A scalar damage measure for seismic reliability analysis of RC frames*. *Earthquake Engineering & Structural Dynamics*, 2007. **36**(13): p. 2059-2079.
26. Jalayer F., Elefante L., Iervolino I., and Manfredi G., *Knowledge-based performance assessment of existing RC buildings*. *Journal of Earthquake Engineering*, 2011. **15**(3): p. 362-389.
27. Papadimitriou C., Beck J.L., and Katafygiotis L.S., *Updating robust reliability using structural test data*. *Probabilistic Engineering Mechanics*, 2001. **16**(2): p. 103-113.
28. Box G.E.P. and Tiao G.C., *Bayesian Inference in Statistical Analysis*, ed. W. Interscience. 1992: John Wiley & Sons, Inc.
29. Benjamin J.R. and Cornell C.A., *Probability, Statistics, and Decision for Civil Engineers*. 1970: McGraw-Hill, New York.
30. Shome N., *Probabilistic seismic demand analysis of nonlinear structures*. RMS Program. 1999, Stanford University.
31. DeRisi R., Jalayer F., Iervolino I., Kyessi A., Mbuya E., Yeshitela K., and Yonas N., *Guidelines for vulnerability assessment and reinforcement measures of adobe houses*, deliverable in CLUVA project - Climate Change and Urban Vulnerability in Africa. 2012. Available from: http://www.cluva.eu/deliverables/CLUVA_D2.4.pdf. Data last access: 01/01/2013.

Chapter 6

URBAN FLOOD RISK ASSESSMENT

This chapter is dedicated to flood risk assessment in the urban areas in a bi-scale approach. On one hand, risk assessment in the *micro-scale* is discussed. This involves calculating various risk metrics, by integrating micro-scale flooding hazard (see Chapter 3) and portfolio vulnerability (see Chapter 5), for different points of interest. On the other hand, a meso-scale approach to risk assessment is presented. The *meso-scale* flood risk assessment is finalized towards the delineation of flood-prone areas, the identification of urban flooding hot-spots, and evaluating the potential exposure to risk. In the following, both approaches are described.

6.1 Meso-scale flood risk assessment

Urban hot spots can be defined as the zones likely to be exposed to climate-related extreme events such as flooding. Arguably, identifying urban flooding hot spots is one of the first steps in an integrated methodology for urban planning and risk management. The delineation of urban hotspots does not only provide useful information for policy makers but it can also be useful as supporting information for indicating future urban dynamics and trends. Figure 6.1 illustrates a schematic representation of an urban hot spot identified as R (standing for risk) as an area in which high probability of occurrence of climate related events identified as H (standing for hazard) coincides with areas of high vulnerability identified as V (such as sensitive buildings or major roads).

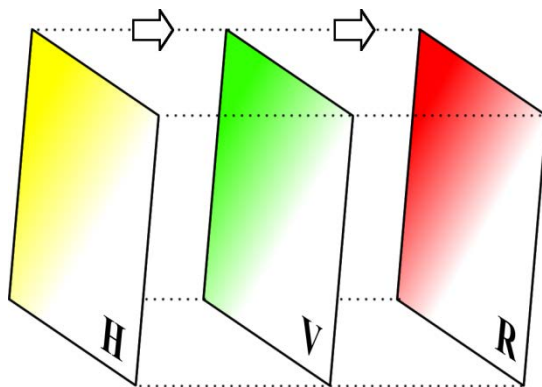


Figure 6.1 - Hazard (H), Vulnerability (V) and Risk (R), the concept of an urban hot-spot.

This work employs three GIS-based frameworks for identifying the urban hot spots for residential buildings and urban corridors (i.e., major roads). This is performed by overlaying a map of potentially flood prone areas (identified by the topographic wetness index, TWI), a map of urban morphology types (UMT) classified as residential or as urban corridors, and a geo-spatial census dataset for demographic information (e.g., population density). The topographic wetness index [1] allows for the delineation of a portion of a hydrographic basin potentially exposed to flood inundation by identifying all the areas characterized by a topographic index that exceed a given threshold.

The urban morphological types [2, 3] (see Chapter 2) form the foundation of a classification scheme which brings together facets of urban form and function. Once an appropriate UMT classification scheme is established for a particular study area, individual UMT units can be delineated using aerial photography and other geospatial data sources. UMT units are often mapped at a 'meso'-scale (i.e. between the city level and that of the individual units). This makes them a suitable basis for the spatial analysis of cities.

The TWI threshold is calibrated within the basin through a Bayesian parameter estimation framework shown in Chapter 4. In particular, the Bayesian parameter estimation enables a probabilistic characterization of the

threshold by calculating the complementary probability of false delineation of flood prone zones as a function of various threshold values. For a given return period, the probability of false delineation is calculated as the sum of the probability of indicating a zone flood prone, while it is not indicated as such by the inundation profile, and the probability that a zone is indicated as not flood prone but indicated as flood prone by the inundation profile. Applying the above-mentioned procedure, taking into account all available information on the inundation profiles for various zones within the basin, leads to a probability distribution for the TWI threshold value. It should be mentioned that the flood prone areas identified herein are not differentiated with respect to the spatial variation in flooding hazard within the area. A recent work by Degiorgis et al. [4] employs pattern classification techniques for the delineation of flood-prone areas and hazard graduation within these areas based on remote-sensed data.

In the next step, the urban residential flooding hot spots are determined in the GIS environment by overlaying the map of TWI and the UMT units classified as residential for various percentiles of the TWI threshold. Additional information related to exposure such as population density and demographic information can be integrated by overlaying geo-spatial datasets created based on Census data. Differences in exposure characteristics can be assessed for a range of different residential types, including for example between condominium/multi-storey, single storey stone/concrete and areas predominantly associated with informal constructions. For each percentile value considered, the delineated flood-prone residential areas and the number of people potentially affected to flooding are calculated.

6.1.1. The case of Addis Ababa

The urban morphology types for Addis Ababa are classified and delineated based on aerial photos acquired in December 2010. Below in Figure 6.2, the high level UMT map for Addis Ababa is shown.

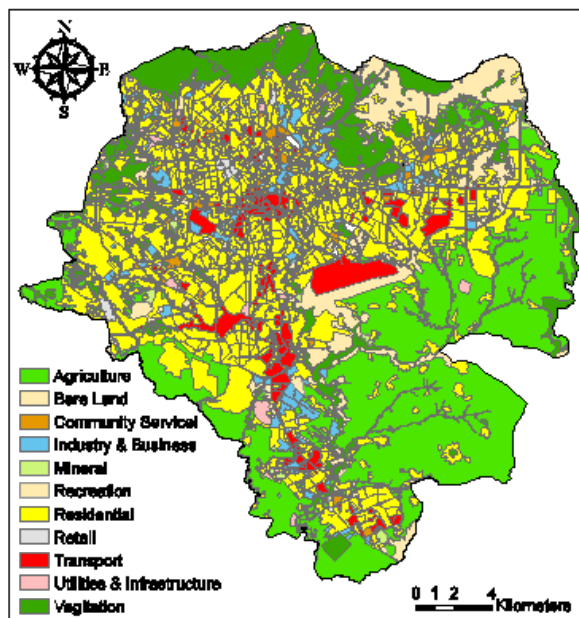


Figure 6.2 - High level UMT map for Addis Ababa (2011)

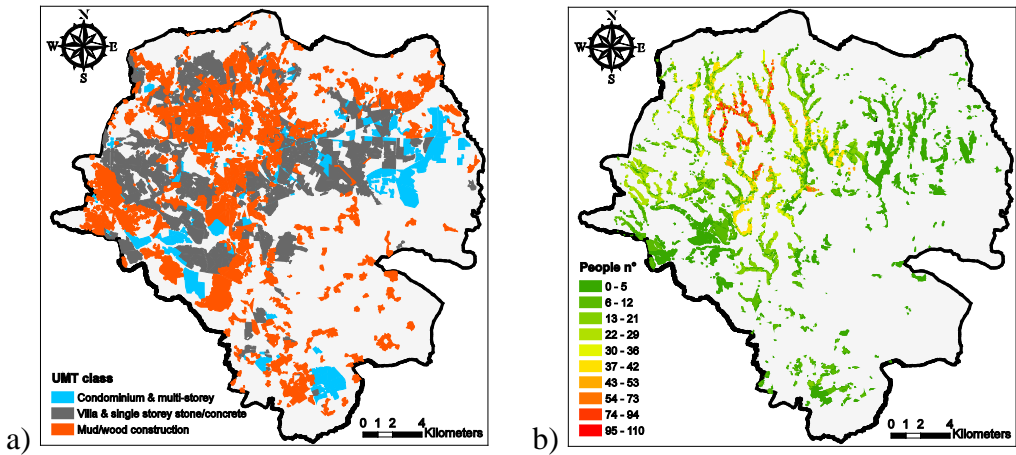
There is a large area devoted to agriculture (Figure 6.2). In 2006, field crops alone made up over one quarter of the area of the Addis Ababa study area, by far the largest area associated with a single sub-UMT category [5]. Around one third of the city is associated with UMT's classified as residential; among which, the mud/wood construction has the largest proportion (46%). About 3.4% of the city area is covered by major road corridors (i.e. with a width bigger than 15m). Although there is some evidence of an urban core, the UMT map provides further evidence of Addis Ababa's multi-nucleated character [6]. There is a large proportion of bare land (9%); at least some of which is likely to be associated with future urban development. More detailed information about the identification of UMT sub-categories and the delineation of the UMT units for the city of Addis Ababa is available in [5].

Identification of urban hotspots by overlaying the TWI, UMT and Census datasets: Three spatial datasets, namely, the map of flood prone areas, the

urban morphology units classified as residential or major road corridors, and 2007 geo-spatial Census dataset for Addis Ababa have been overlaid in order to estimate flood exposure to flooding expressed as the estimated number of affected people.

The residential UMT: The spatial units characterized as residential cover about 35% of the entire city surface; in which about 46% of the population is concentrated. This category is further divided in three sub-categories: a) condominium and multi-storey buildings (covering 5.3% of the city surface and containing 4 % of the population), b) villa and single storey stone/concrete buildings (covering 13.3% of the city surface and containing 16% of the population), and c) mud and wood construction (covering 16.1% of the city surface and containing 26% of the population).

Figure 6.3 illustrates the delineated urban hotspots (the colored zones), obtained by overlaying the UMT, the TWI, and the geo-spatial dataset on population density obtained from the City census (2007), for different estimates of TWI threshold.



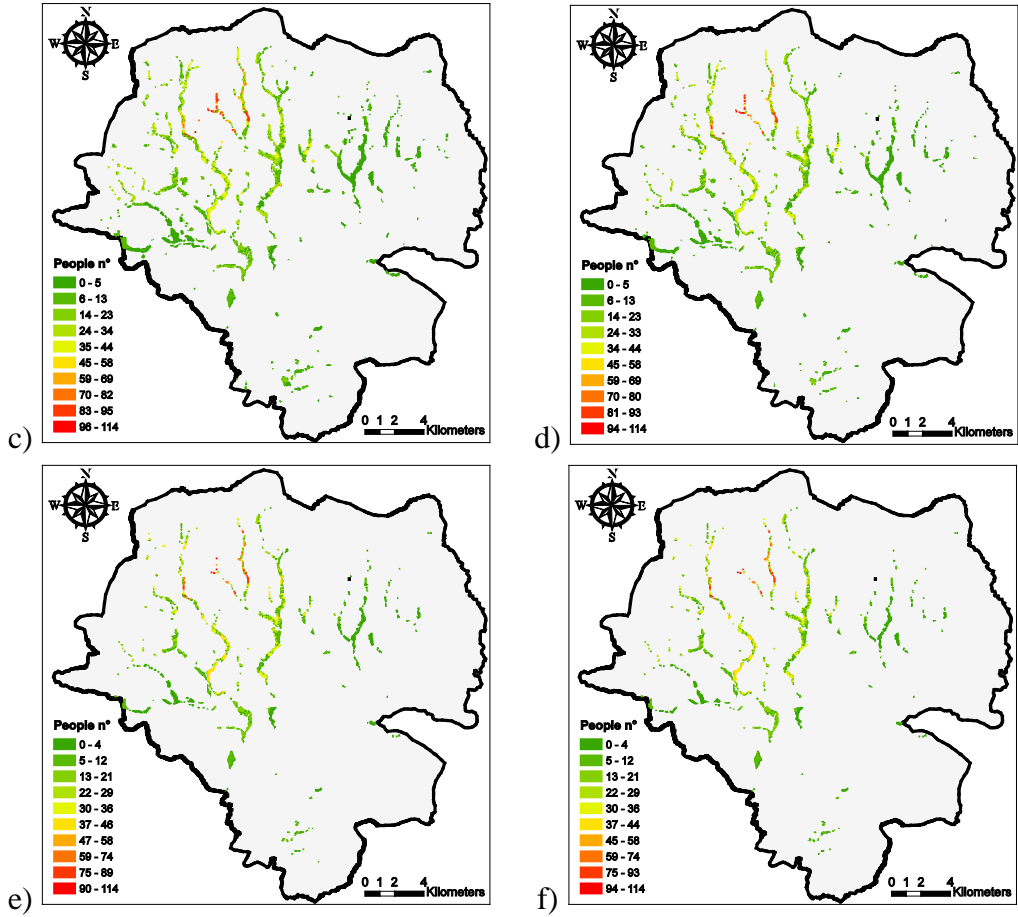


Figure 6.3 - The urban residential flood hot spots delineated for different TWI thresholds: a) residential area, b) 16th percentile, c) τ_{ML}^- , d) maximum likelihood, e) 50th percentile, f) τ_{ML}^+ .

Table 6.1 below demonstrates the percentage of residential area affected by flooding (the areal extent of hot spots illustrated in Figure 6.3 normalized by total residential area) and the percentage of people that live in the residential area affected (estimated population normalized by total population in the residential area), for different estimates of the TWI threshold.

% of Residential	τ_{ML}	τ_{16}	τ_{50}	τ_{ML}^-	τ_{ML}^+
Area	4.6%	22.2%	3.07%	6.0%	2.7%
People	6.0%	26.9%	3.7%	7.1%	3.3%

Table 6.1 - Exposure to flooding risk in terms of the estimated percent of residential area and people affected by flooding

As shown in Figure 6.4, the functional relationship between the TWI threshold and the number of affected people is monotonically decreasing. Therefore, based on the invariance property of percentiles [7] when the mapping function is monotonically increasing or decreasing, the 16th percentile of the TWI threshold translates into 84th percentile of the number of affected people and vice versa¹⁴.

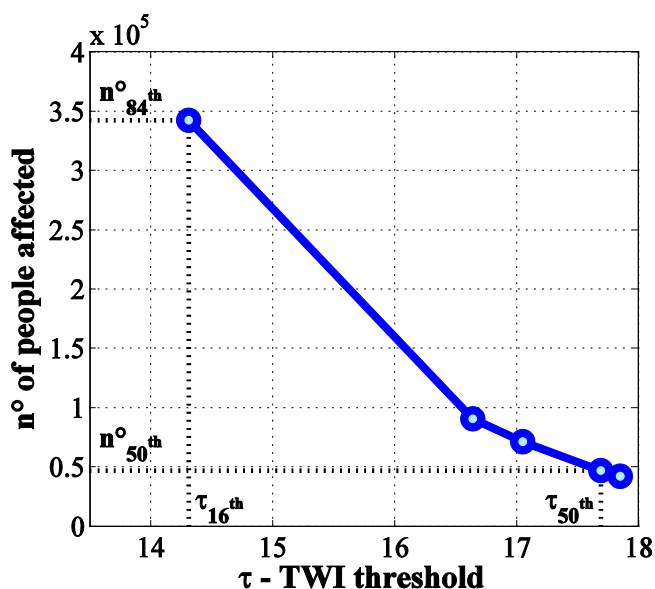


Figure 6.4 - TWI threshold - number of people

¹⁴ Assuming that the estimation of the TWI threshold is the only source of uncertainty.

Table 6.2 shows that the percentages of the total Addis Ababa population affected by floods associated with τ_{50} and τ_{16} range from 1.7% to 12.5%. This can be interpreted as the 50th and 84th percentiles of the ratio of number of people (in the residential areas) potentially affected by flooding to the total city population.

% of City	τ_{ML}	τ_{16}	τ_{50}	τ_{ML}^-	τ_{ML}^+
People	2.6%	12.5%	1.7%	3.3%	1.5%

Table 6.2 - Exposure to flooding risk in terms of the estimated percent of residential people affected by flooding respect to the entire city population

Discussion: The pie chart shown in Figure 6.5 below illustrates the percentage breakdown of the areal extent of the residential flood hot spots (corresponding to τ_{ML} equal to 17.05) in terms of different residential subclasses; namely, a) condominium/multi-storey, b) single storey stone/concrete and c) mud/wood construction.

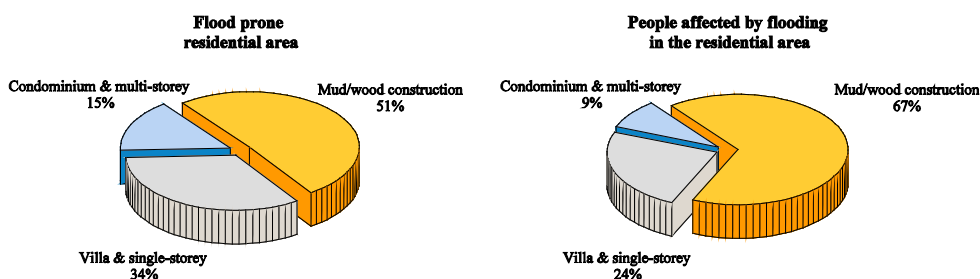
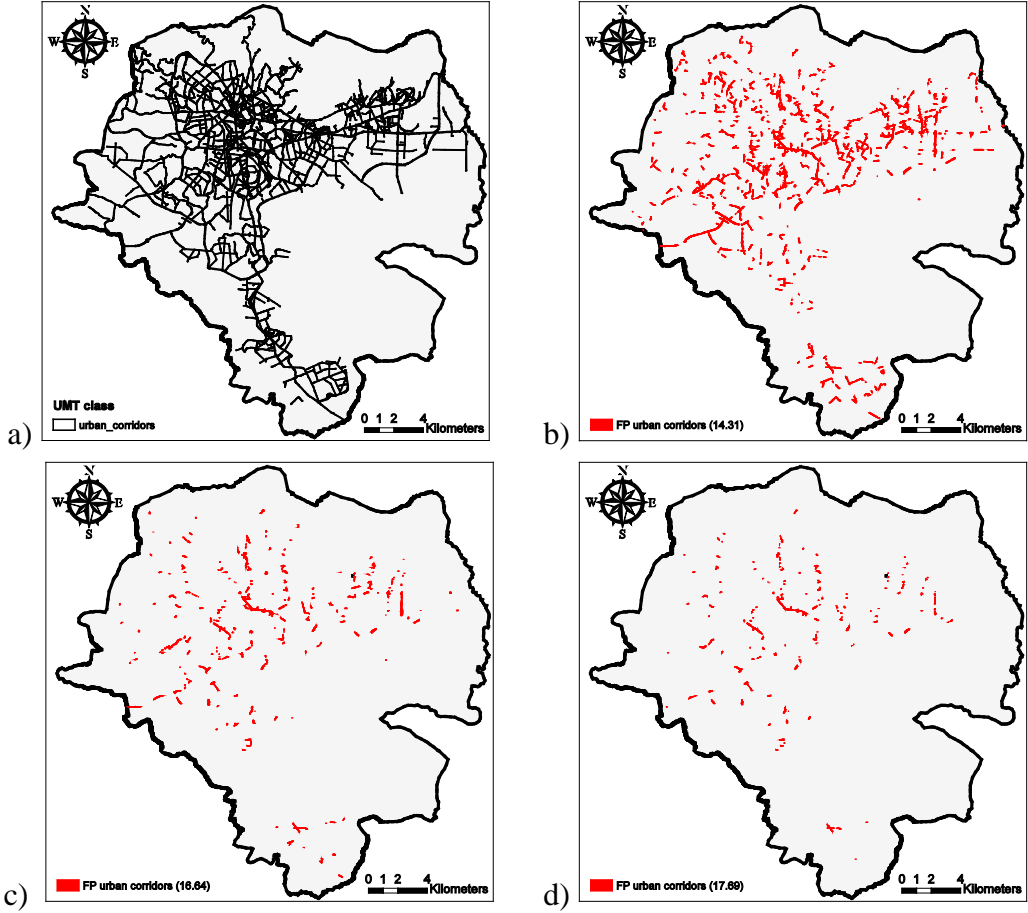


Figure 6.5 - Breakdown of the residential hot-spot in terms of flood prone residential area and people affected by flooding in the residential area.

It can be observed that 67% of the population in the flood prone residential area lives in mud and wood constructions (constituting 51% of the total residential area). These constructions are particularly vulnerable to flooding.

The major road corridors UMT: The UMT class "major road corridors" covers about 3.4% of the whole city surface. Below in Figure 6.6, the delineated urban road corridor hotspots (the red zones) are shown for different estimates of TWI threshold.



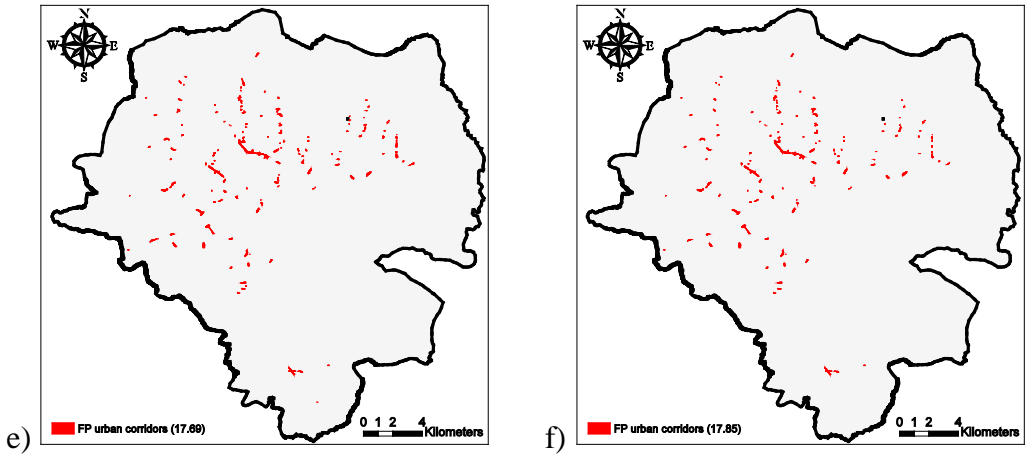


Figure 6.6 - The urban corridor hot spots for flooding delineated for different TWI thresholds: a) residential area, b)16th percentile, c) τ^-_{ML} , d)maximum likelihood, e) 50th percentile, f) τ^+_{ML} .

Table 6.3 below reports the percentage of roads affected by flooding (estimated as the extent of red hot spots illustrated in Figure 6.6 normalized by total urban corridors area) for different estimates of the TWI threshold.

% of Urban	τ_{ML}	τ_{16}	τ_{50}	τ^-_{ML}	τ^+_{ML}
Corridors Area	5.2%	23.4%	3.4%	6.9%	2.9%

Table 6.3 - Exposure assessment in terms of urban corridors

6.1.2. The case of Dar es Salaam

The urban morphology types for Dar es Salaam are classified and delineated based on aerial photos acquired in December 2010. Below in Figure 6.7, the high level UMT map for Dar is shown.

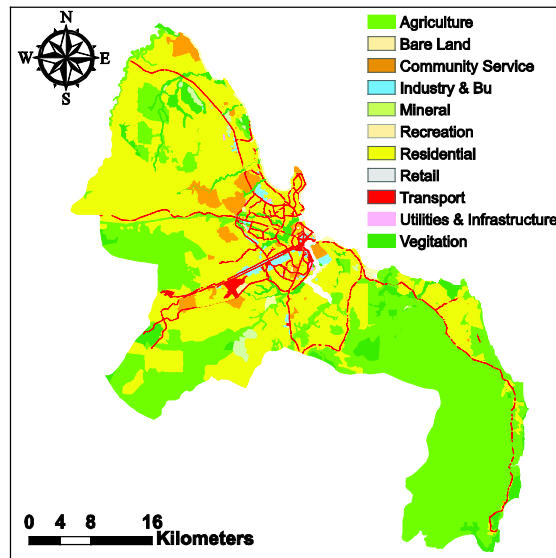


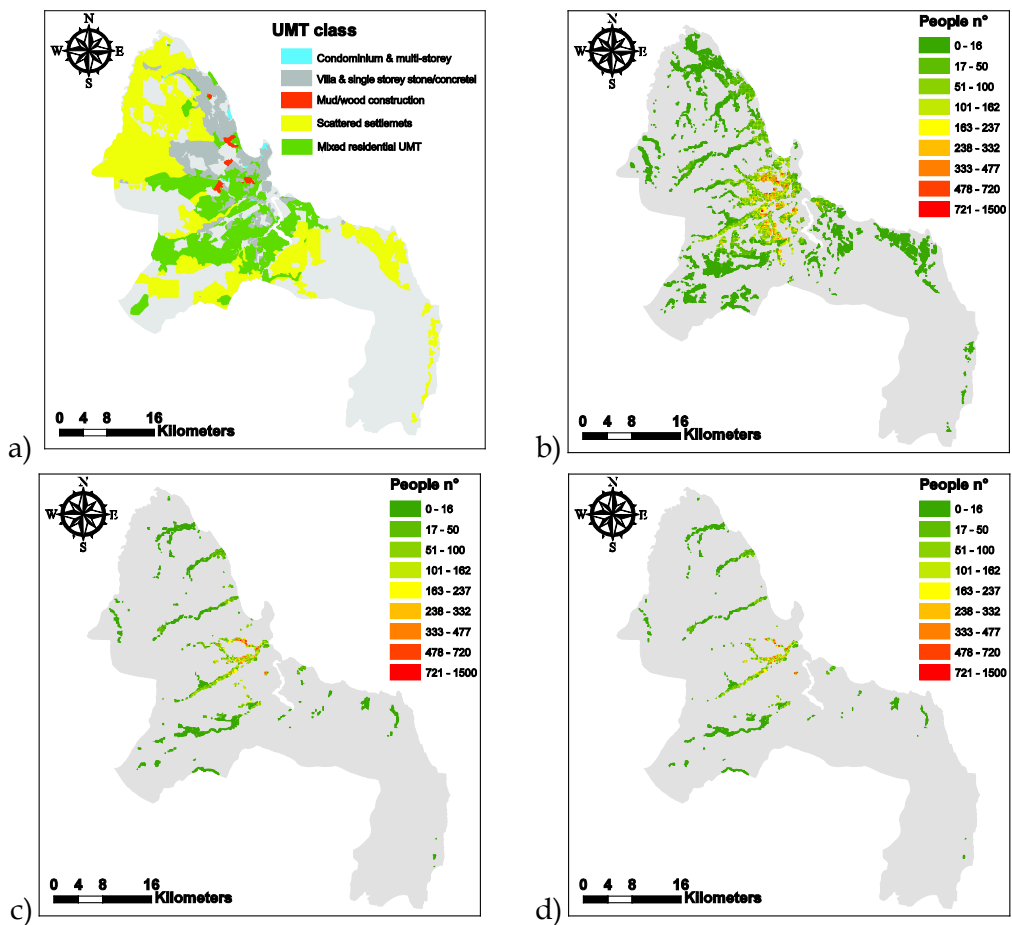
Figure 6.7 - High level UMT map for Dar es Salaam.

Identification of urban hotspots by overlaying the TWI and UMT datasets: The urban hot spots can be delineated by overlaying the flood prone areas and the urban morphology units classified as residential or major road corridors. Furthermore, integrating information from census results and/or field surveys/interviews, it will be also possible to estimate the exposure to flooding expressed as the estimated number of affected people.

The residential UMT: The spatial units characterized as residential cover about the 47% of the entire city surface; in which about the 60% of the population is concentrated. This category is further divided in five sub-categories: a) condominium and multi-storey buildings (cover the 0.2% of the city surface and contain the 0.5 % of the population), b) villa and single storey stone/concrete buildings (cover the 7.8% of the city surface and contain the

17% of the population), c) mud and wood construction (cover the 0.4% of the city surface and contain the 2% of the population), d) scattered settlements (cover the 25% of the city surface and contain the 5.3% of the population) and e) mixed residential (cover the 13% of the city and contain the 36% of the population).

Figure 6.8 illustrates the delineated urban hotspots (the colored zones), obtained by overlaying the UMT and the TWI datasets, for different estimates of TWI threshold.



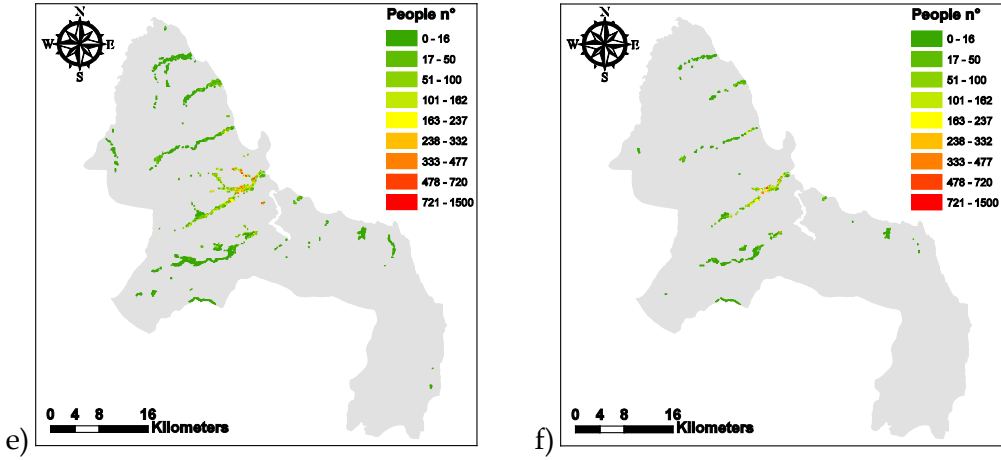


Figure 6.8 - The urban residential hot spots for flooding delineated for different TWI thresholds: a) residential area, b) 16th percentile, c) τ_{ML}^- , d) maximum likelihood, e) 50th percentile, f) τ_{ML}^+ .

Furthermore, the information on population density obtained from the city Census is integrated in order to estimate the number of affected people by flooding for different statistics of the TWI threshold. Table 6.4 below demonstrates the percentage of residential area affected by flooding (the areal extent of hot spots illustrated in Figure 6.8 normalized by total residential area) and the percentage of people that live in the residential area affected (estimated population normalized by total population in the residential area), for different estimates of the TWI threshold.

% of Residential	τ_{ML}	τ_{16}	τ_{50}	τ_{ML}^-	τ_{ML}^+
Area	3.45%	23.08%	3.53%	4.93%	1.31%
People	6.35%	37.76%	6.48%	9.14%	2.44%

Table 6.4 - Exposure to flooding risk in terms of the estimated percent of residential area and people affected by flooding

It can be noted that the percentages of people affected to flooding for Dar es Salaam in correspondence to τ_{50} and τ_{16} varies in the interval [1.48%, 22.91%]

of the total Dar es Salaam population. This¹⁵ can be interpreted as the 50th and 84th percentiles of the number of people (in the residential areas) affected to flooding.

% of City	τ_{ML}	τ_{16}	τ_{50}	τ_{ML}^-	τ_{ML}^+
People	3.85%	22.91%	3.93%	5.54%	1.48%

Table 6.5 - Exposure to flooding risk in terms of the estimated percent of residential people affected by flooding respect to the entire city population

Discussion: The pie chart shown in Figure 6.9 below illustrates the percentage break-down of the residential hot spots areal extent (corresponding to τ_{ML} equal to 19.53) in terms of different residential sub-classes; namely, a) condominium/multi-storey, b) single storey stone/concrete and c) mud/wood construction, d) scattered settlement and e) mixed residential.

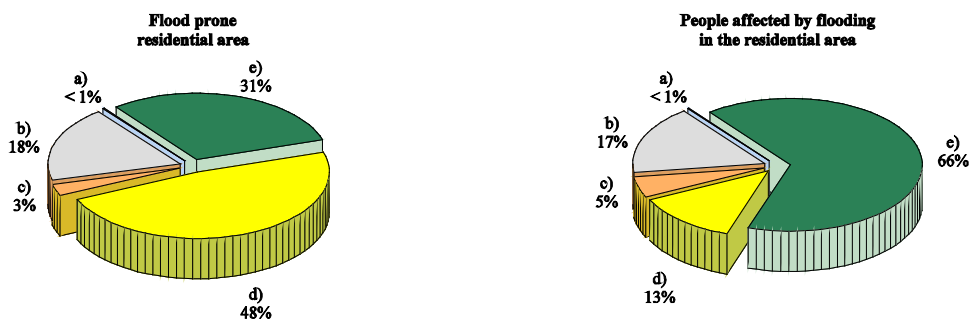


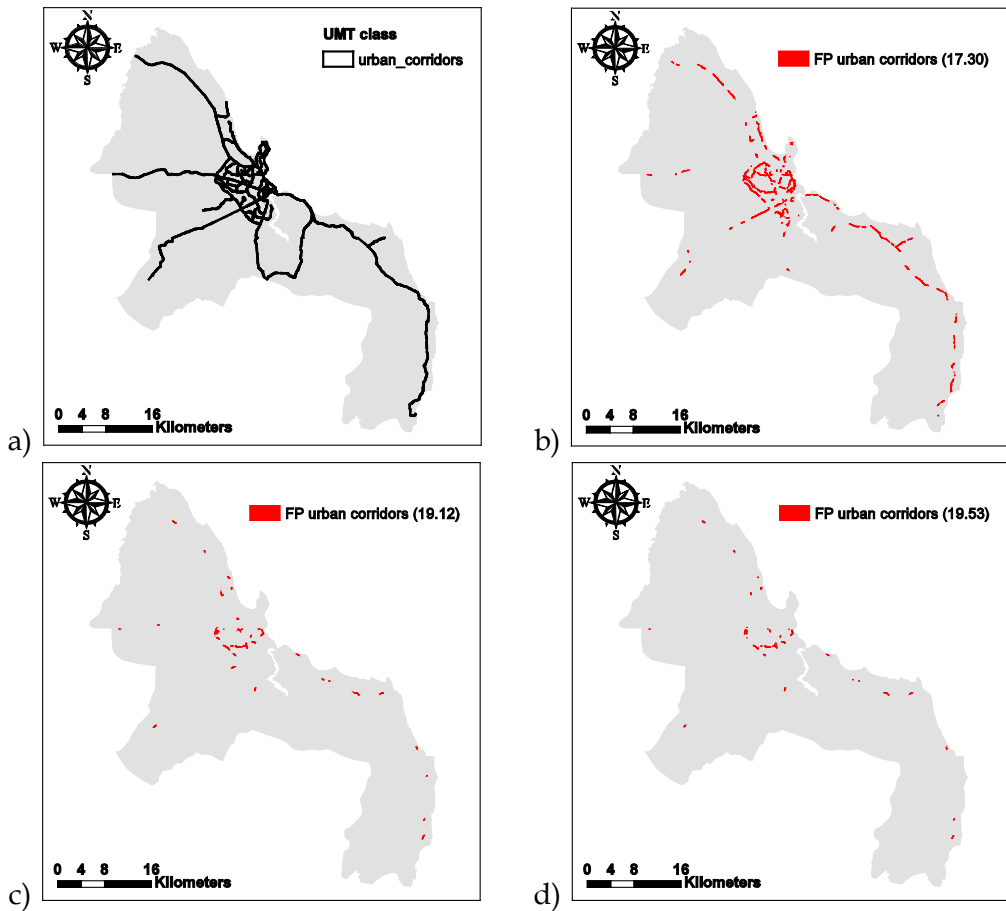
Figure 6.9 - Breakdown of the residential hot-spot in terms of flood prone residential area and people affected by flooding in the residential area.

It can be observed that around 66% of the population in the flood prone residential area lives in residential types labeled as mixed. This residential type constitutes around 31% of the flood-prone residential buildings. On the other

¹⁵ If the process of calculating the number of affected people is strictly monotonic, the percentiles of threshold value would be translated directly into the same percentiles for the estimated number of people.

hand, around 50% of the flood-prone buildings belong to the scattered settlements category which have house around 13% of the flood-prone population.

The major road corridors UMT: The UMT class "major road corridors" covers about 0.5% of the whole city surface. Below in Figure 6.10 - , the delineated urban road corridor hotspots (the red zones) are shown for different estimates of TWI threshold.



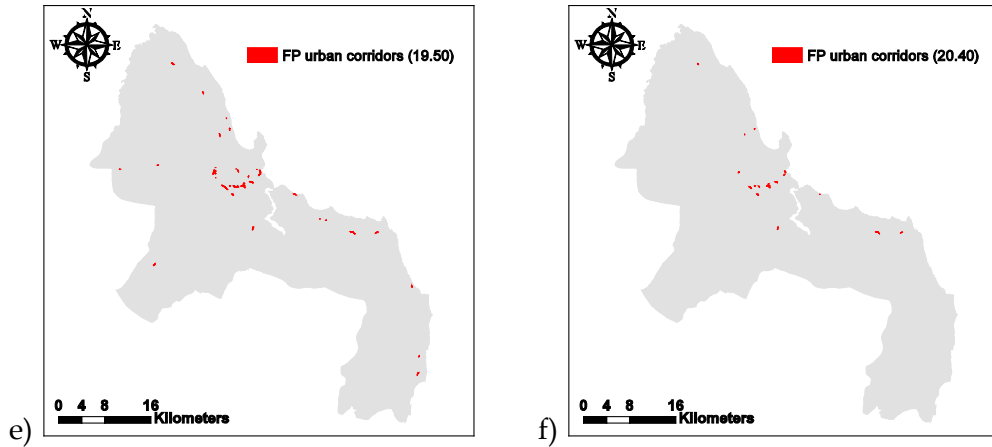


Figure 6.10 - The urban corridor hot spots for flooding delineated for different TWI thresholds: a) residential area, b) 16th percentile, c) τ_{ML}^- , d) maximum likelihood, e) 50th percentile, f) τ_{ML}^+ .

Table 6.6 below reports the percentage of roads affected by flooding (estimated as the extent of red hot spots illustrated in Figure 6.10 normalized by total urban corridors area) for different estimates of the TWI threshold.

% of Urban Corridors Area	τ_{ML}	τ_{16}	τ_{50}	τ_{ML}^-	τ_{ML}^+
	3.80%	29.81%	3.93%	5.87%	1.54%

Table 6.6 - Exposure assessment in terms of urban corridors

It can be observed that around 66% of the population in the flood prone residential area lives in residential types labeled as mixed. This residential type constitutes around 31% of the flood-prone residential buildings. On the other hand, around 50% of the flood-prone buildings belong to the scattered settlements category that hosts around 13% of the flood-prone population.

6.1.3. Summary and remarks on meso-scale flood risk assessment

Urban flood hot spots for residential buildings and urban corridors (major roads) are delineated by overlaying three GIS-based datasets, namely, the topographic wetness index (TWI), the urban morphology types (UMT), and

the population density. The flood prone areas based on the TWI method are identified by delineating the areas distinguished with a TWI larger than a certain threshold. This threshold can be calibrated based on available information, such as inundation profiles calculated for a certain area within the basin. A probabilistic GIS-based method is used for calculating the maximum likelihood estimate and the 16th and 50th percentiles for the TWI threshold based on available inundation profiles. Bayesian parameter estimation is used to evaluate the threshold based on inundation profiles calculated for more than one area within the basin. The flood prone areas delineated for various threshold statistics (e.g. ML, 16th percentile) are then overlaid with the UMT units identified as residential and major road corridors in order to identify the urban hot spots and the areal extent of the UMT units affected by flooding. Integrating the population density geo-spatial dataset as a third layer, leads to estimation of the number of people affected by flooding¹⁶.

This methodology is applied to delineate urban hotspots for flooding for the cities of Addis Ababa and Dar es Salaam. The resulting likelihood function for the TWI threshold reveals an interval in which it reaches its maximum value and remains more-or-less invariable -- referred to as the 99% maximum likelihood interval. The maximum likelihood estimate seems to be insensitive to the return period corresponding to the inundation profile used for calibrating the TWI. In other words, for the case of Little Akaki in Addis and Suna in Dar, the spatial extent of the inundation profiles does not change much as a function of the return period. On the other hand, the inundation heights are quite sensitive to the return period. Incorporating the inundation profiles calculated for two different zones seems not to affect the maximum likelihood estimate significantly, although it leads to wider 99% maximum likelihood intervals. Differences in exposure characteristics have been assessed for a

¹⁶ It should be noted that the meso-scale calculations do not take into account the spatial correlations in flooding propagation. Therefore, the estimated number of affected people is more strictly the estimated number of people who live in potentially flood prone residential areas.

range of different residential types.

In particular, referring to Addis Ababa, it can be seen that the mainly mud and wood construction category comprises around half (50%) of the total land area associated with residential buildings that are located in the flood prone areas in Addis. A disproportionate amount of the population – around two-thirds (67%) - is estimated to live within these areas of flood-prone mud and wood dwellings. The overall impact of flooding in these zones is likely to be disproportionately large as a result of the susceptibility to damage of the building stock and the likelihood that inhabitants have high social vulnerability, e.g. in terms of available resources to cope with floods. It is estimated that between around 1.7% (50th percentile) and 12.5% (16th percentile) of the total population of Addis may be affected by flooding. Further, between 3.4% (50th percentile) and 24.4% (16th percentile) of the total area of major urban roads is estimated to be affected by flooding which is likely to affect response and recovery activity and the everyday activities of all in the city, whether directly impacted or not. In acting on these results, it is important to emphasize that uncertainty in the TWI threshold leads to considerable difference in the estimated areal extent of affected areas and consequently the exposure to flooding. The probabilistic methodology presented in this paper can be used also to estimate the TWI threshold based on maps of flood prone areas based on previous flooding events.

Arguably, urban hot spot identification can be considered as one of the fundamental initial steps in strategic urban planning, helping to establish zones of high hazard-exposure and through combination with other data, such as UMT maps and other demographic geo-spatial datasets, identify those zones which are also likely to see disproportionate impacts due to the characteristics of local neighborhoods. In addition to forming the basis of current and retrospective assessments, this information can also be used in order to predict future urban trends and development scenarios.

It would be interesting to explore the possibility of further developing the presented methodology for the identification of the urban hot spots in order to take into account: (a) spatial variation of flooding hazard within the

flood prone areas; (b) variation of vulnerability within residential UMT spatial units.

6.2 Micro-scale flood risk assessment

Micro-scale flood risk assessment can be summarized in a single equation (Eq. (6.1)), where λ_{LS} denotes the risk expressed as the mean annual rate of exceedance of a given limit state (LS). The limit state refers to a threshold (e.g., critical water height $h_{f,c}$, critical velocity $v_{f,c}$) for a structure, beyond which, it no longer fulfills a specified functionality. $\lambda(h_f)$ denotes the mean annual rate of exceedance of a given flooding height h_f at a given point in the considered area. $P(LS | h_f)$ denotes the flooding fragility for limit state LS expressed in term of the probability of exceeding the limit state threshold.

$$\lambda_{LS} = \int_{h_f} P(LS | h_f) \cdot |d\lambda(h_f)| \cdot dh_f \quad (6.1)$$

It should be noted that the flooding fragility embodies both the uncertainties in mechanical material properties and the building-to-building variability in features relevant to flooding. The risk λ_{LS} is calculated in terms of the mean annual frequency of exceeding the limit state LS for each node of the lattice covering the zone of interest by integrating fragility $P(LS | h_f)$ and the (absolute value of) hazard increment $|d\lambda(h_f)|$ over all possible values of flooding height. The mean annual frequency of exceeding the limit state λ_{LS} is later transformed into the annual probability of exceeding the limit state assuming a homogenous Poisson process as a model for occurrence of limit-state-inducing events.

In this thesis, as shown in Chapter 3, the limit state threshold is specified based on the critical flood height. That is, the limit state threshold can be defined as the critical water height, beyond which the structure exceeds the limit state in question. It is helpful in this context to consider the critical water height as a proxy for the structural capacity for the specified limit state.

It should be noted that Eq. (6.1) manages to divide the flood risk assessment procedure in two main modules, namely, the hazard assessment

module which leads to the calculation of the mean annual frequency $\lambda(h_f)$ of exceeding a given flooding height h_f and the vulnerability assessment module which leads to the calculation of the flooding fragility curve in terms of the probability of exceeding specified limit state $P(LS|h_f)$.

Figure 6.11 demonstrates a flow chart of the proposed procedure for micro-scale flood assessment. As it can be seen in the flowchart, historical rainfall data is transformed into rainfall probability curves. This information together with detailed topography of the area, geology maps and land-use maps are then used in order to evaluate the basin hydrograph and to develop the flooding hazard maps (i.e., inundation scenarios for various return periods). The vulnerability of the portfolio of structures (e.g., informal settlements) is then evaluated in terms of fragility functions for a specific limit state, based on orthophotos of the area, sample in-situ building survey and laboratory tests for mechanical material properties. Finally, the flooding risk map is obtained by integrating the flooding hazard map and the fragility functions.

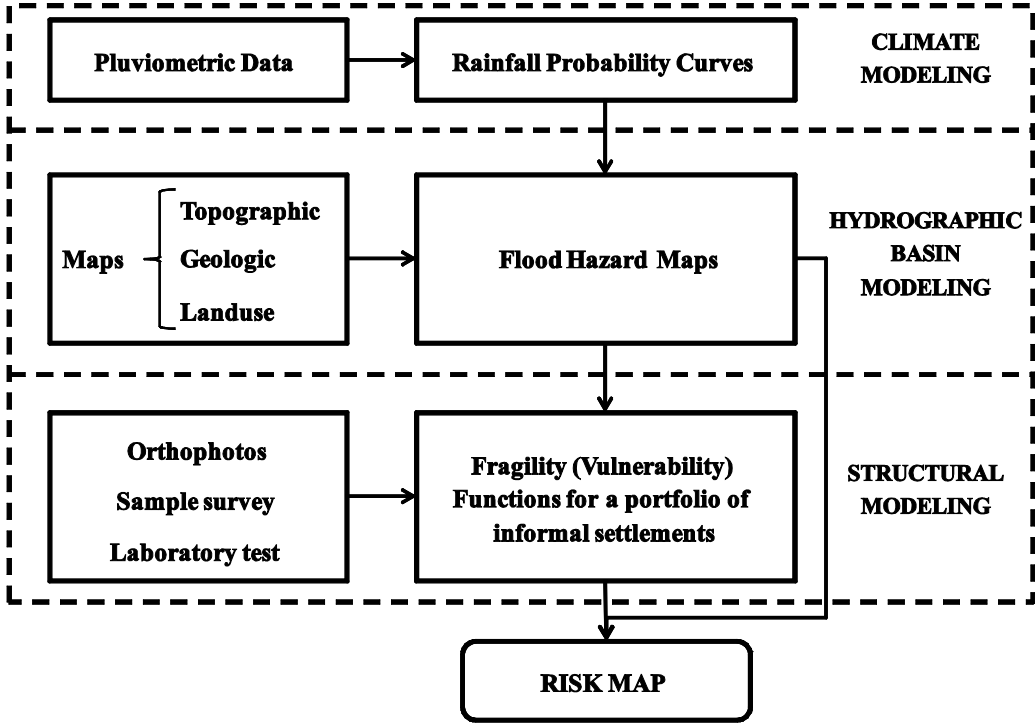


Figure 6.11 - Flow-chart representation of the micro-scale flood risk assessment methodology (special application to a portfolio of informal settlements).

As it can be observed, the proposed methodology integrates climate modeling, hydrographic basin modeling and structural fragility modeling in order to generate the risk map for the zone of interest.

6.2.1. Risk assessment

Point estimates of the flooding risk can be obtained by integrating the robust fragility for the class of structures and the flood hazard in Eq. (6.1). In this case, the flooding risk is expressed in terms of the mean rate of exceeding the structural limit state (i.e., exceeding the critical flooding height corresponding to the limit state in question) for a given point. The annual probability of exceeding a limit state $P(LS)$, assuming a homogeneous Poisson process model with rate λ_{LS} , can be calculated as:

$$P(LS) = 1 - \exp(-\lambda_{LS}) \quad (6.2)$$

The exposure to risk can be quantified by calculating the total expected loss or the expected number of people affected for the portfolio of buildings.

6.2.2. Expected loss

The expected repair costs¹⁷ (per building or per unit residential area), $E[R]$, can be calculated as a function of the limit state probabilities and by defining the damage state i as the structural state between limit states i and $i+1$:

$$E[R] = \sum_{i=1}^{N_{LS}} [P(LS_{i+1}) - P(LS_i)] \cdot R_i \quad (6.3)$$

where N_{LS} is the number limit states that are used in the problem in order to discretize the structural damage; R_i is the repair cost corresponding to damage state i ; and $P(LS_{N_{LS}+1}) = 0$.

6.2.3. Expected number of people affected

The expected number of people affected by flooding can also be estimated as a function of the limit state probabilities from Eq. (6.3) replacing R_i by the population density (per house or per unit residential area).

6.2.4. The case of Suna in Dar es Salaam

The proposed methodology for micro-scale flood risk assessment is applied to a portfolio of informal settlements in Suna sub-ward, Dar es Salaam (see Chapters 3 and 5). The rain-fall curves (IDF curves, see Chapter 3) are obtained based on both historical precipitation data and also down-scaled climate projections for a given scenario (RCP8.5). The vulnerability of the selected portfolio of informal buildings in Suna is represented by the robust fragility curves (16th, 50th and 84th percentiles) calculated in the previous

¹⁷ It should be mentioned that, in principle, the expected loss should also take into account the contribution of the costs related to the down-time, end of life and maintenance.

chapter. These fragility curves are calculated based on 20 Monte Carlo extractions (estimating the probabilities by simulating from their distributions, see Chapter 5 for detailed explanation). Figure 6.12 superimposes the robust fragility curves (life safety, SL) with the flooding hazard curves calculated at the centroid of each building considered --considering historical rainfall data.

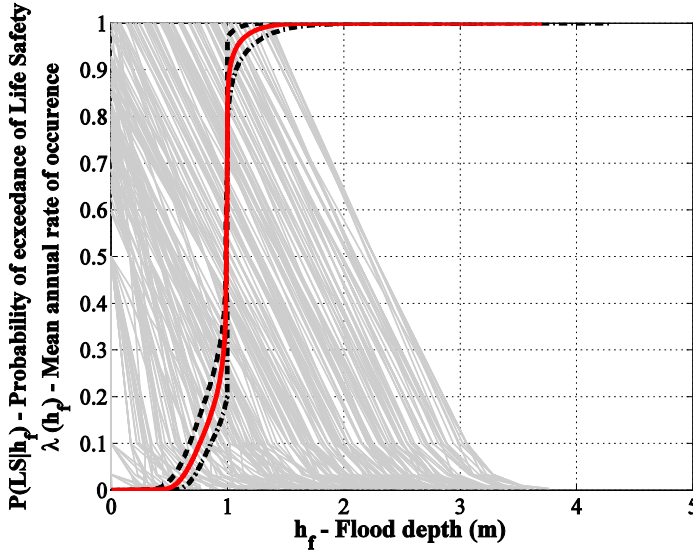


Figure 6.12 - Superposition of robust fragility curves and flooding hazard curves (SL, historical data)

Finally the flooding risk can be calculated by integrating the fragility and the hazard as stated in Eq. (6.1). The risk evaluated in terms of mean annual rate of exceeding the life safety limit state for the case study area is reported in Figure 6.13.

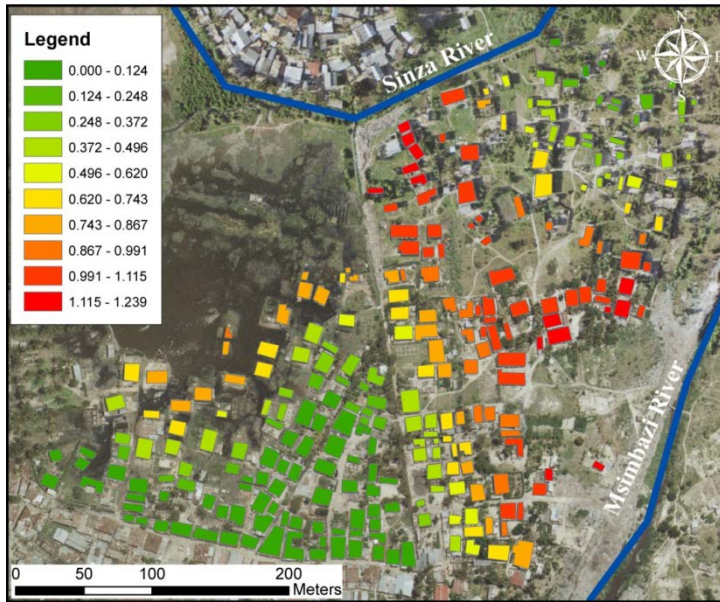


Figure 6.13 - The mean annual rate of exceeding the life safety limit state, Suna Subward (historical rainfall data)

It can be observed that many structures have a annual frequency of exceeding the critical flood height larger than one. This indicates that on average, assuming that the structure is going to be reconstructed each time that it is collapsed, the structure is going to collapse more than once a year due to flooding. This is consistent with the high flooding values expected, as showed in Figure 3.12 in Chapter 3. For example, the flooding height corresponding to a return period of 2 years is around 2.5 meters. The annual probability of exceeding the life safety limit state is calculated from Eq. (6.2) and plotted in Figure 6.14.

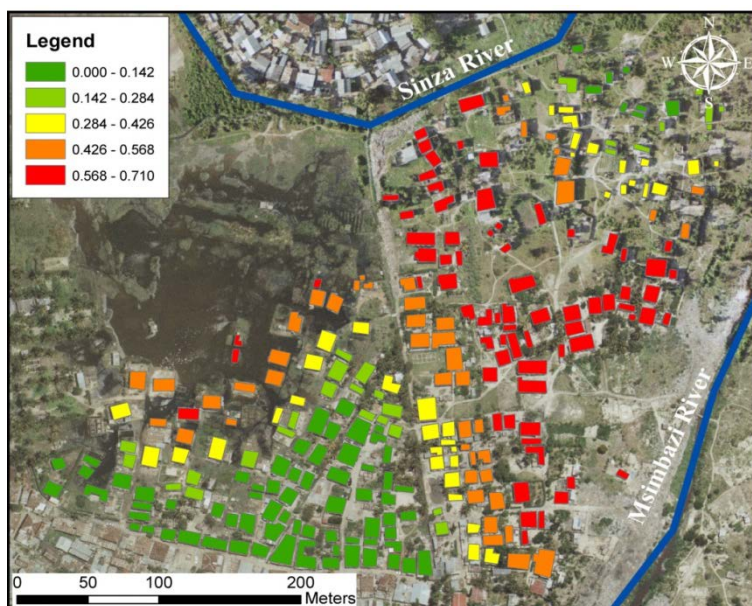


Figure 6.14 - Annual probability of exceeding the critical flooding height for Suna sub-ward (historical rainfall data).

Finally, the total annual expected replacement costs is calculated from Eq. (6.3) summed up over all the buildings within the portfolio of structures -- considering only the life safety limit state. In this case, the repair cost per unit area corresponding to the life safety limit state is assumed to be equal to the replacement/reconstruction costs of 5\$/m². The total area of the buildings within the portfolio is already calculated through the ortho-photo boundary-recognition. The total annual expected replacement cost normalized by the total cost of reconstruction of the entire portfolio is equal to 35%.

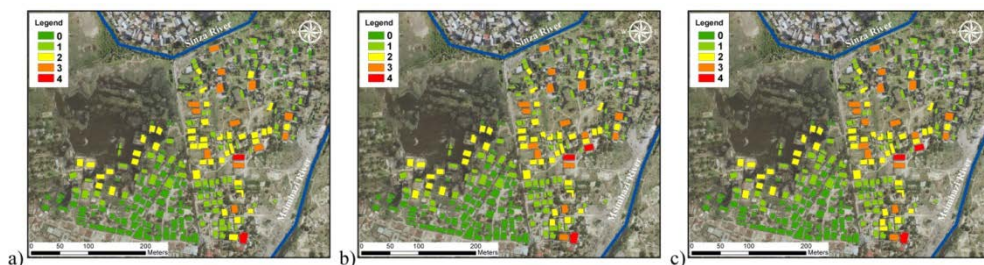


Figure 6.15 - Expected number of people affected by flooding in a year corresponding to a) Fragility- σ b) Fragility and c) Fragility+ σ .

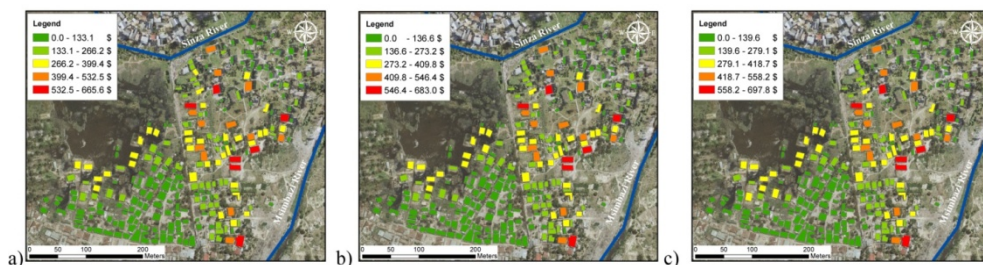


Figure 6.16 - Expected annual replacement costs per building relative to a) Fragility- σ b) Fragility and c) Fragility+ σ (Suna Subward, historical rainfall data).

Assuming a population density of 0.03 per unit area, the expected number of people endangered by flooding in one year is calculated to be 227 over 658, this is equal to 35% of the total estimated number of people living in the case-study area. In Figure 6.15 and Figure 6.16, the results in terms of expect number of people endangered and expected replacement costs are shown, respectively, considering the uncertainties in the fragility assessment. Neglecting other sources of uncertainties (e.g., the modeling uncertainties related to hazard estimation, the uncertainties in estimating the exposure), the expected replacement costs are estimated be variable between 33% (corresponding to fragility - σ) to 36% (corresponding to fragility + σ) of the total exposure in the interested area.

Using climate projections instead of historical data (for calculating IDF curves, hazard curves in Figure 3.6), exposure to flooding estimated by the (normalized) expected replacement costs changes from 35% to 30%. This indicates an overall decrease in flooding risk for Suna Subward based on climate projections. However, it should be emphasized that these results do not take into the future change in land-use as a result of rapid urbanization.

References

1. Qin C.-Z., Zhu A.X., Pei T., Li B.-L., Scholten T., Behrens T., and Zhou C.-H., *An approach to computing topographic wetness index based on maximum downslope gradient*. Precision Agriculture, 2011. **12**(1): p. 32-43.
2. Pauleit S. and Duhme F., *Assessing the environmental performance of land cover types for urban planning*. Landscape and Urban Planning, 2000. **52**: p. 1-20.
3. Gill S.E., Handley J.F., Ennos A.R., Pauleit S., Theuray N., and Lindley S.J., *Characterising the urban environment of UK cities and towns: A template for landscape planning*. Landscape and Urban Planning, 2008. **87**: p. 210-222.
4. Degiorgis M., Gnecco G., Gorni S., Roth G., Sanguineti M., and Taramasso A.C., *Classifiers for the detection of flood-prone areas using remote sensed elevation data*. Journal of Hydrology, 2012. **470-471**: p. 302-315.
5. Cavan G., Lindley S., Yeshitela K., Nebebe A., Woldegerima T., Shemdoe R., Kibassa D., Pauleit S., Renner R., Printz A., Buchta K., Coly A., Sall F., Ndour N.M., Ouédraogo Y., Samari B.S., Sankara B.T., Feumba R.A., Ngapgue J.N., Ngoumo M.T., Tsalefac M., and Tonye E., *Green infrastructure maps for selected case studies and a report with an urban green infrastructure mapping methodology adapted to African cities, deliverable in CLUVA project - Climate Change and Urban Vulnerability in Africa*. 2012. Available from: http://www.cluva.eu/deliverables/CLUVA_D2.7.pdf. Data last access: 01/01/2013.
6. Nyarirangwe M., *The impact of multi-nucleated city morphology on transport in Addis Ababa in Managing Ethiopian Cities in an Era of Rapid Urbanisation*, M.P. van Dijk and J. Fransen,, E.U. BV, Editor. 2008.
7. Jaynes E.T., *Probability theory: The logic of science*. 2003: Cambridge university press.

Chapter 7

VISK: A GIS-COMPATIBLE PLATFORM FOR MICRO-SCALE ASSESSMENT OF FLOODING RISK IN URBAN AREAS

Evaluation of the vulnerability of buildings in urban areas to flooding is a fundamental step in flooding risk mitigation. In this chapter, a new GIS-compatible computer platform and matlab-based graphical user interface is presented: VISK, "Visual Vulnerability & Risk", flooding module. This platform performs detailed (micro-scale) flood risk assessment for building stock with more-or-less similar characteristics. The GIS compatibility allows for graphical processing of both input and output to the program, providing an efficient visualization of flooding risk. At the core of the this platform lies the comprehensive probability-based algorithm for the assessment of the vulnerability of a class of buildings to flooding, already defined in Chapter 5. This Bayesian algorithm is based on assigning prescribed analytic uni- and bi-modal probability distributions for characterizing the flooding structural fragility functions. This allows for efficient evaluation of structural fragility based on a small number of (around 20-50) Monte Carlo simulations. The fragility calculations are performed on a bi-dimensional finite-element structural model considering the openings (door and windows) constructed using open-source software Opensees. The uncertain structural modeling parameters are characterized through, orthophoto recognition, sample in-situ building survey, laboratory test results for material mechanical properties and literature survey. Finally, the risk map is generated by integrating the flooding hazard and fragility taking into account additional information on the exposure (e.g., repair costs, population density, etc.). The results can be

visualized both in a detailed building-to-building scale (of potential interest to single house-holds) or as overall estimates for the entire area (of interest to policy makers).

7.1 Introduction to framework

Delineation of flood prone areas and the evaluation of the vulnerability of buildings in the urban areas to flooding are fundamental steps in taking adaptive measures for flooding risk. This demands cross-cutting scientific and technical support from different disciplines, such as but not limited to, climate modeling, hydraulic engineering, structural engineering, risk modeling and urban policy making. In recent years, increasing attention is focused on flooding risk assessment, just think to HAZUS [1, 2], that defines a general methodological approach to flood risk assessment.

In this context, development of tools that allows for quantifying flooding risk efficiently and with sufficient accuracy is essential. These methods serve as technical support to the stakeholders and policy makers, for flood risk mitigation, emergency preparedness, response and recovery, both in short- and long-term.

In this work, a new software tool for flood risk assessment for individual buildings is presented. VISK, acronym of Visual Vulnerability and Risk (Flooding), is a GIS-compatible platform that performs micro-scale flood risk assessment for buildings located in homogenous (i.e., characterized as a single class of buildings) urban areas. Figure 7.1 below demonstrates the graphical user interface for VISK.

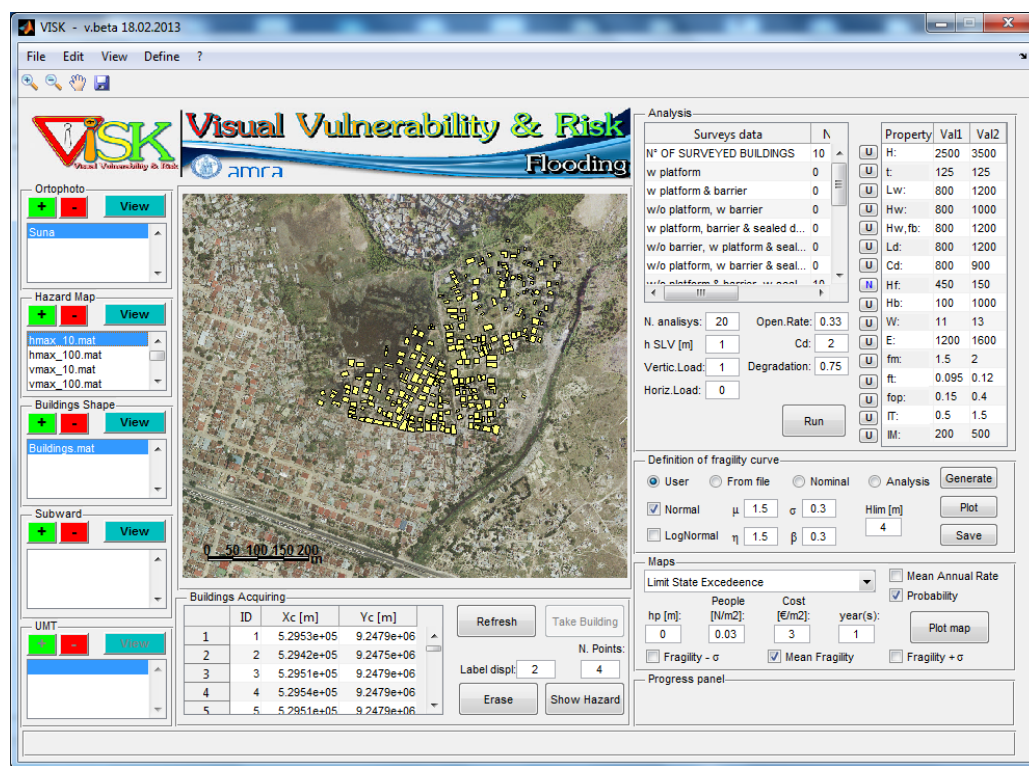


Figure 7.1 - The graphical user interface of VISK

The main parts of the graphical user interface for VISK are: (1) the central display panel in which the orthophoto of the case study area is demonstrated. The orthophoto can be overlaid on the spatial polygons representing buildings' foot-prints (i.e., a GIS shape file) and the flooding height/velocity profile for a prescribed return period; (2) the orthophoto input panel where an orthophoto of the case-study area can be up-loaded; (3) the flood profile panel where a lattice of nodes containing maximum flood depth and velocity pairs for each node for a given return period can be up-loaded; (4) building shape panel where the GIS shape file of the buildings' spatial boundary can be up-loaded; (5) a panel for miscellaneous information in which data such as spatial delineation of administrative boundaries can be up-loaded; (6) a panel for the acquisition of data regarding buildings' spatial foot-prints, where in lieu of shape files, for each building, the spatial foot-print can be specified manually

and processed by the program; (6) a digital survey sheet where the results of building-specific field survey can be specified. This digital panel is matched with a building-specific survey sheet; (7) a structural analysis panel where a specified number of structural model realizations are generated and analyzed based on the data provided by the digital survey sheet; (8) a fragility assessment panel where the fragility curves for a specified limit state are derived based on the results of the simulations performed in the structural analysis panel. This panel also envisions up-loading of user-defined fragility curves; (9) risk map generation panel where risk maps are plotted for various risk metrics such as the frequency of exceeding a given limit state, expected repair/replacement costs, etc; (10) a progress panel which visualizes the progress of the program. In the following, various functionalities of VISK are discussed in detail. In order to render the description more accessible, each section is accompanied by a numerical example.

Background: VISK is created inside the European FP7 project CLUVA: Climate change and urban vulnerability in Africa. The original idea was to create a tool for vulnerability assessment of informal settlements in Africa. The problem of vulnerability assessment for a portfolio of "informal" and non-engineered buildings is particularly challenging due to many aspects such as lack of complete information and poor construction details. In fact, the core vulnerability assessment methodology created for VISK is organized in a manner so that various sources of uncertainty can be taken into account, with particular attention to structural detailing and water-tightness. Moreover, due to lack of precise survey data, the software uses sample surveys as a basis and constructs probability distributions for the probability of observing/not observing certain structural details in a given building in a Bayesian framework. The idea of constructing a probability distribution for a probability may seem unintuitive; however, it relays precious information about the quantity of data/survey results used for calculating it. Needless to say, VISK as a visual interface and platform for vulnerability and risk assessment is applicable not only to the non-engineered structures in an African context but also to other structural typologies in alternative contexts.

7.2 Input data

The input data required by platform VISK are: orthophoto of the case-study area, spatial foot-print of the buildings, flooding height/velocity profiles for prescribed return periods and the uncertainties in structural modeling parameters related to both material mechanical properties, construction details and geometry (in the form of probability distributions). In this section, each input category is described in more detail.

7.2.1. *Orthophoto and footprint of the buildings*

The orthophoto of the case-study area needs to have the following characteristics: at least 300 dpi of resolution, aspect ratio of about one, georeferenced in a specific coordinate system (eg. UTM,WGS 1984) that remains the same for all the other input (i.e. flood hazard maps, buildings shape). As far as it regards the spatial foot-print of the buildings to be analyzed, the program accepts a dataset containing the information stored for each spatial polygon that defines the building boundary (i.e., a GIS shape file format). In case such a spatial dataset is not available, VISK can extract the plan dimensions by performing orthophoto boundary recognition guided by the user. User's role is to manually define the nodes of the polygon that define building's foot print as illustrated in Figure 2.3 in Chapter 2. The user-guided boundary recognition operation not only helps in creating a digital database of buildings for which risk assessment is later going to be performed but also helps in characterizing the building-to-building variability in the dimension of the wall which is going to resist the flood action¹⁸.

7.2.2. *Characterization of uncertainties*

VISK can be used for flooding risk assessment for individual buildings located in a homogenous urban area. Therefore, the main function of VISK as a

¹⁸ Neglecting the effect of internal walls or embedded columns in reducing the "free" loading span.

software for vulnerability assessment is the assessment of fragility curves for a single class of structures. Hopefully, this capability is going to be extended to more than one class of structures in the near future. Therefore, the uncertainties considered are primarily related to building-to-building variability in material properties, geometry and construction details. In the previous chapters, the procedure for characterizing these uncertainties was described in detail.

As mentioned in the previous section, orthophoto recognition can be used in order to capture the variation of buildings' footprints in the case-study area. However, building specific field surveys are needed in order to gain better understanding of the geometry and construction details. As far as it regards survey-based input requirements for VISK, information on the uncertain parameters can be specified in two alternative ways: (1) discrete binary uncertain variables based on a logic-tree approach; (2) continuous uncertain variables, as already described in Chapter 5.

7.2.3. Hydraulic results and flooding hazard curves

Inundation profiles calculated for various return periods are one of the main input data fed into VISK. The inundation profile is generally expressed in terms of flood depth and velocity, for different return periods of the extreme precipitation event, for each node within a lattice that cover the entire case study area. This information is usually obtained through a general hydrologic/hydraulic routine. VISK acquires inundation profiles for various return periods, in terms of gridded data set in Arc ASCII grid format, typical output file of commercial softwares that develop mono/bi-dimensional diffusion models [3, 4].

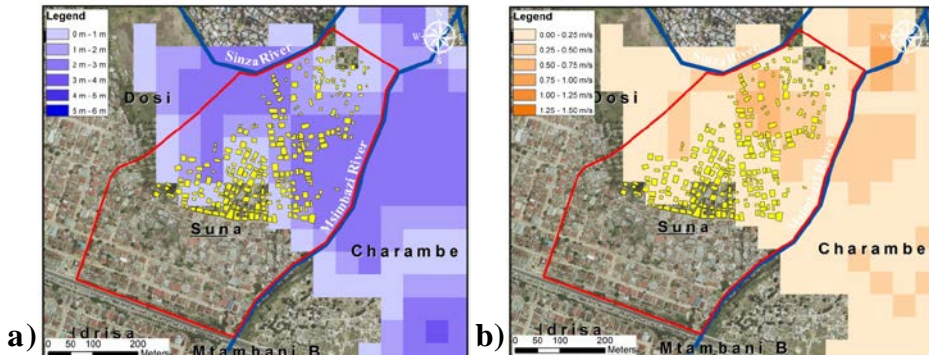


Figure 7.2 - Inundation profiles for a given return period in terms of a) flood depth and b) flood velocity [5]

Once the grid dataset of the inundation profiles has been acquired by VISK, the software creates an overlay of the inundation profile (for various return periods and classified by flooding height and/or velocity) and the uploaded orthophoto of the case-study area.

VISK has the capability of extracting flooding hazard curves in terms of the mean annual frequency of exceeding (equal to the inverse of return period for a homogenous Poisson process) a given flooding height or velocity for a given point within the case-study area (e.g., centroid of a given building), based on the input grid dataset described in the previous paragraph. This is done by a spatial interpolation between the point (identified as G in Figure 3.3) and the flood height/velocity values at the nearby nodes of the lattice grid containing the point in question. This operation is already described in detail in Chapter 3. Moreover, VISK can automatically reproduce the power-law fit between flood depth and velocity, obtaining and storing the parameters a and b for each building.

Using the above-mentioned capabilities, VISK can generate hazard curves for centroid points of all the buildings identified within the case-study area as illustrated in Figure 7.3 below. Figure 7.3 (a) and Figure 7.3 (b) illustrate the hazard curves for all the building centroid points within a given case-study area for flooding height and velocity, respectively. For each

building centroid, the set of $\mathbf{H}=[h_{max}, v_{max}]$ pairs and the power-law relation fitted to them are plotted in Figure 7.3 (c).

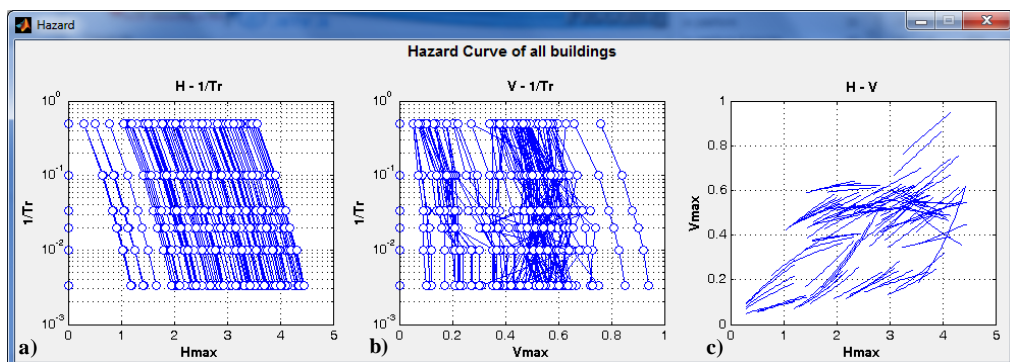


Figure 7.3 - Hazard curves in terms of maximum flood a) height, b) velocity and c) relation between flood height and flood velocity. [5]

7.3 Visual vulnerability assessment platform

Structural vulnerability assessment lies in the core of VISK platform. The vulnerability assessment results are represented as the fragility curves, expressing the probability of exceeding a prescribed limit state. The software envisions various modes for acquiring the necessary input: (a) calculating the fragility curves based on the input provided to VISK; (b) creating Normal/Lognormal fragility curves based on the first two moments (i.e., mean and standard deviation); (c) creating fragility curves based on data uploaded by the user from a file; (d) creating step-function fragilities, referred to in the program as the Nominal fragilities. The approach (a) is fully explained in Chapter 5.

7.3.1. The limit states

The fragility curves are calculated for three limit states, namely, serviceability, structural collapse and life safety. In VISK, limit state thresholds are expressed in terms of the critical flooding height. Serviceability is marked by the critical water beyond which the normal activities in the household is

going to be interrupted, most probably due to water infiltration. For example, for an insufficiently water-tight buildings built on a raised foundation, the critical serviceability water height is equal to the height of raised foundation above the ground level. For buildings constructed according to flood-resistant criteria, the critical water height for limit state of serviceability is taken asymptotically equal to the critical height needed for exceeding collapse limit state assuming brittle failure modes. Collapse limit state is defined as the critical flooding height in which the most vulnerable section of the most vulnerable wall in the building is going to break. Life Safety limit state defines the critical flooding height in which lives of the inhabitants is going to be in danger. This can be caused either due to the infiltration of water inside the building (with the increasing risk of drowning in water), or the structural collapse (defined in the same manner as the critical height for collapse limit state). The critical water height for structural collapse is calculated in VISK by employing structural analysis taking into account the various sources of uncertainties in geometry, material properties and construction details. As far as it regards life safety considerations, VISK allows the consideration of judgment-based or code-based nominal water height.

For all the limit states considered within VISK, a simulation-based routine is employed in order to propagate the various sources of uncertainties described in Chapter 5. VISK employs an efficient simulation-based procedure relying on a small number of simulations (e.g., in the order of 50-100).

Assuming that vector θ consists of all the uncertain parameters considered in the problem, simulation i corresponds to the i^{th} realization of vector θ . Each θ_i is sufficient for defining the structural configuration, flood action, and material strength values for i^{th} simulation realization. Having this information, the critical water height can be calculated for each realization of the structural model/action. With reference to the uncertain parameters considered by VISK and described in Chapter 5, vector θ is partitioned in two sections: θ_1 lists the discrete binary uncertain parameters considered; and θ_2 is related to continuous uncertain parameters. Each simulation realization is generated according to the probability distributions for vector θ (at present, correlation structure is considered only for the discrete variables defined using

logic trees).

It is important to emphasize that the sampling procedure is going to involve both the structural model (configuration and material properties) and the flooding action. In particular, the load considered in the structural analysis is going to depend on the degree of water-tightness assigned to the structure based on the quality of doors and windows. Moreover, the parameters identifying the hydro-dynamic pressure profile have been simulated based on the variability of velocity profile with respect to the flooding height profile in the zone of interest, as demonstrated in detail in the section relative to the loading.

7.3.2. The structural analysis

VISK platform relies on the open-source structural finite element analysis software OpenSees [6] for structural analyses. The structural models developed herein are consisted of two-dimensional elastic shell finite element panels with openings (considered as voids). three types of transversal boundary condition restraints are considered: (a) fixed end; (b) hinged; (c) free. For example, if a good transversal connection between two orthogonal walls are established, wall panel with fixed-end restraints can be used. Based on the uncertain parameters related to the geometrical configuration of the buildings, four different types of structural models are generated. These models are distinguished based on the type, number and relative positioning of openings (door and windows). Figure 5.6 illustrates various configurations generated in the simulation procedure.

The current version of VISK considers three kinds of flood action on the structure: (1) hydrostatic; (2) hydrodynamic pressure; (3) accidental waterborne debris impact; (4) material property deterioration (due to elongated contact with water). Detailed description of the above-mentioned flood actions can be found in [7] and are already described in Chapter 5. As far as it regards the flooding pressure, the flooding profile across structural height is considered and the resulting forces are discretized to the panel joints. The

discretized force on the openings (if they are sealed) is applied to the joints located at the opening boundary (neglected if the opening is not sealed).

The critical flooding height for the structure is established through the procedure explained in Chapter 5. For each step of incremental loading the critical demand-to-capacity ratio is calculated. The different types of failure are recorded and can be shown in VISK.

Figure 11 below shows the histogram of critical section/mode of failure corresponding to h_{cr} for a set of $N=200$ simulations performed by VISK. The red column marked as no collapse identifies the simulations in which, for all the water height levels considered, the capacity is always larger than the capacity (i.e., critical height for which $Y(h_{cr})=1$ is not verified).

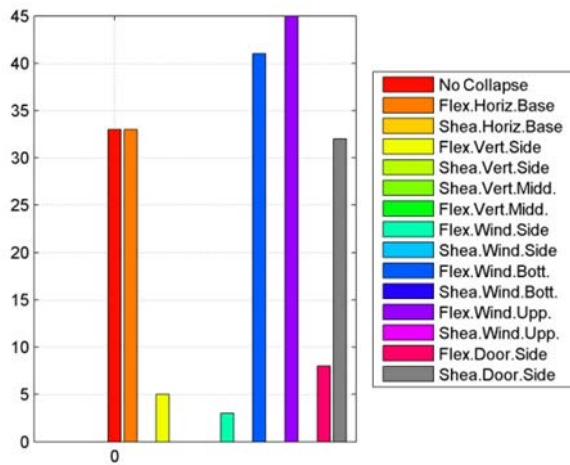


Figure 7.4 - Histogram of critical section/mode of failure corresponding to h_{cr} for a set of $N=200$ simulations

7.3.3. The analytical fragility curves and robust fragility estimation

The analytical fragility curves, and their Bayesian updating to obtain the robust fragility, are calculated for the three limit states as already discussed if Chapter 5.

Figure 7.5 below illustrates the robust fragility curves and their plus/minus one standard deviation interval, corresponding to the three limit states (SE, LS and CO) taken into account into in VISK, based on $N=50$ Monte Carlo simulations.

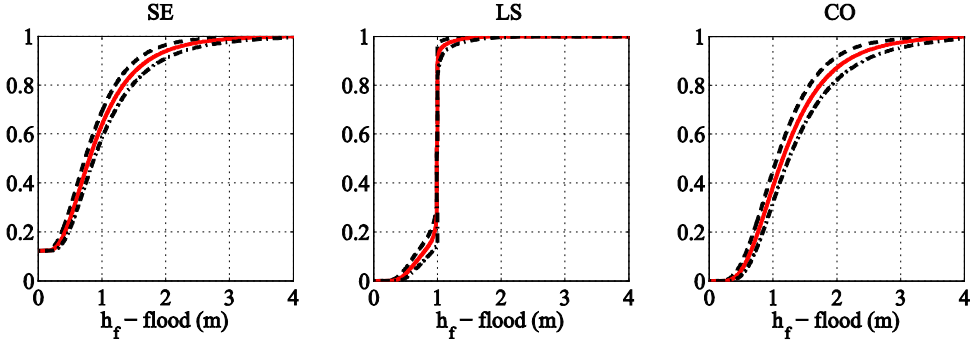


Figure 7.5 - Robust Fragility curves and their plus/minus one standard deviation interval (SE), (LS) and (CO), respectively.

7.4 Visual risk assessment platform

VISK renders point estimates of flooding risk by integrating the robust fragility and its plus/minus one standard deviation intervals ($F \pm \sigma_F$) and the flood hazard at a given point in the zone of study, as shown in Eq. (6.1).

In this case, the flooding risk is $\lambda_{LS}(H_c)^{19}$ is expressed in terms of the mean annual rate of exceeding a prescribed limit state LS (i.e., exceeding the critical flooding height corresponding to the limit state in question) for a given point. The annual probability of exceeding a limit state $P(LS)$, assuming a homogeneous Poisson process model with rate λ_{LS} , can be calculated as shown in Eq. (6.2).

Figure 7.6 and Figure 7.7 illustrates risk maps in terms of mean annual rate λ_{LS} and annual probability $P(LS)$ of exceeding the collapse limit state.

¹⁹ H_c is dropped hereafter for brevity.

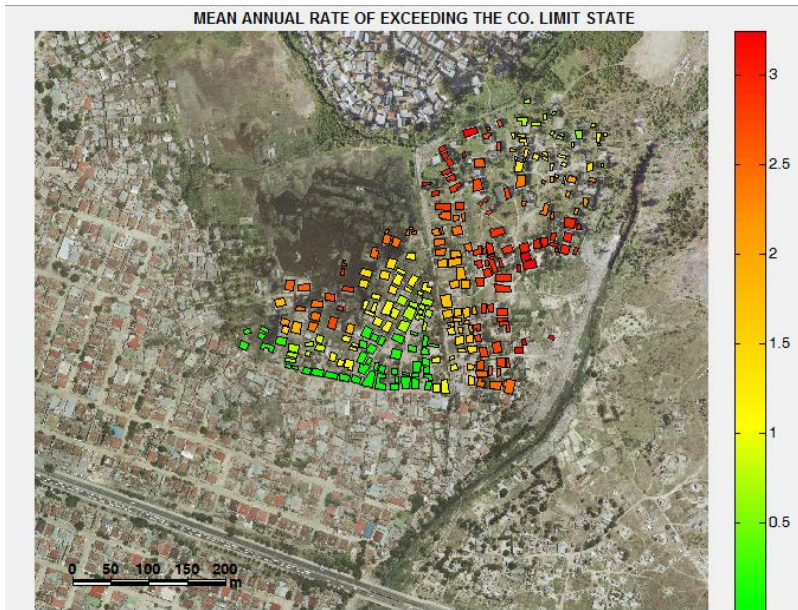


Figure 7.6 - Risk maps in terms of mean annual rate of exceeding the collapse limit state [5]

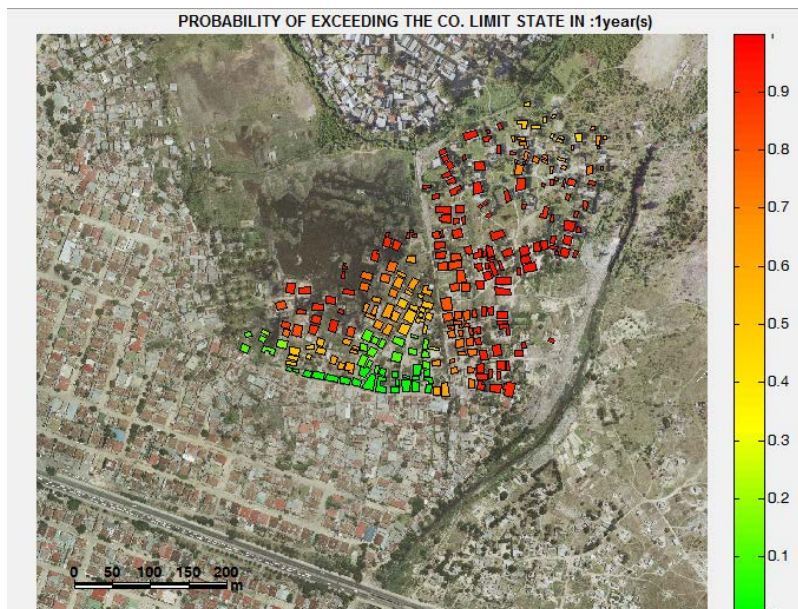


Figure 7.7 - Risk maps in terms of the annual probability of exceeding the collapse limit state [5]

7.4.1. Exposure to risk

VISK estimates the exposure to risk by calculating the total expected replacement costs and the expected number of people endangered for all the buildings identified in the case-study area, for the single limit state of collapse CO. The expected repair cost (per building or per unit residential area), can be calculated as a function of the limit state probabilities as shown in Chapter 6.

7.4.2. Numerical example

Considering a population density of 0.03 per residential square meter and a rebuilding cost of 3 € per square meter (for a single limit state, CO), the expected replacement cost and the expected number of endangered people is calculated from Eq. (6.3) (with $N_{LS}=1$). Figure 15 and 16 illustrate the expected number of casualties and expected replacement cost for the buildings considered in the case-study area.

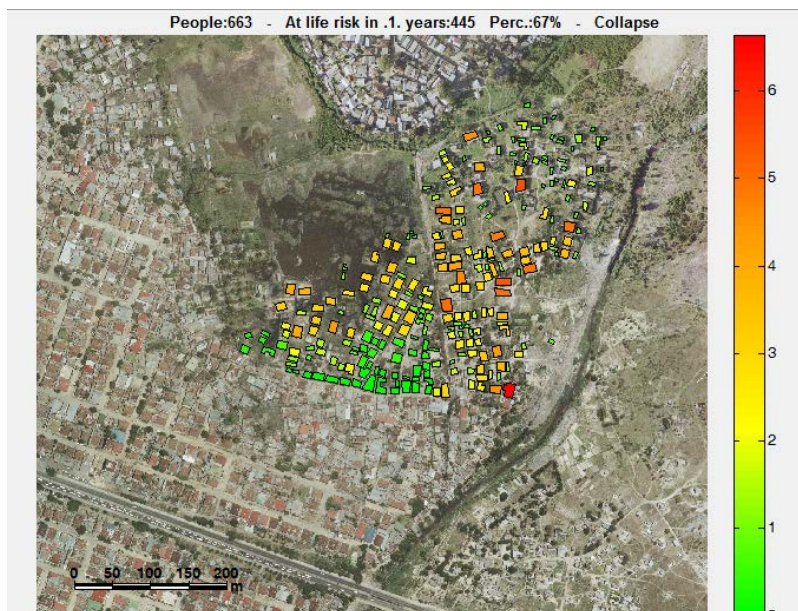


Figure 7.8 - The expected number of casualties [5]

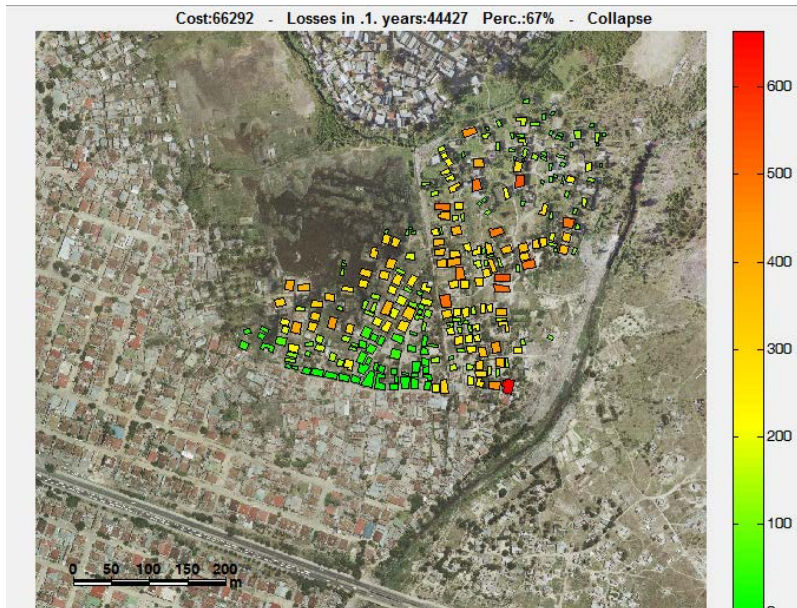


Figure 7.9 - The expected replacement cost [5]

7.5 Summary and Final Remarks

VISK is a new software platform with a graphical user interface for micro-scale flood risk assessment for a single class of buildings. This software, which has been developed in the context of the European FP7 project CLUVA for flood vulnerability assessment of informal settlements (“non-engineered” buildings), is particularly suitable for risk assessment based on incomplete information. This paper has discussed the novel features of VISK. These novel features include: using manual ortho-photo boundary recognition in order to capture the foot-print of the buildings considered; propagation of several sources of uncertainties (e.g., building-to-building variability, incomplete knowledge, limited number of surveys, limited number of simulations) in the calculation of structural fragility for a class of buildings; considering the correlation between discrete binary parameters; using Bayesian parameter estimation based on sample field survey results in order to characterize uncertainties; calculating the structural fragility using an efficient Bayesian small-sample simulation method; an exhaustive iterative procedure for

localizing the structural damage in the model structure; considering the openings in the model structure; taking into account flood actions such as the hydro-static and hydro-dynamic pressure, the debris impact and material deterioration due to elongated contact with water, taking into account the effect of water-seepage in structural analysis. The fragility curves for the class of buildings are calculated for three limit states of serviceability (SE), structural collapse (CO), and life safety (LS). Various point-wise risk metrics are adopted in VISK for evaluating the flooding risk, the mean annual rate and annual probability of exceeding a prescribed limit state, the expected loss, and the expected number of people affected by flooding.

It should be noted that, although VISK is developed for micro-scale flood risk assessment of informal settlements, it can be applied to other building types in general. As future development, the authors intend to extend the capabilities of VISK in order to perform vulnerability assessment for multiple classes of structures.

References

1. Scawthorn C., Blais N., Seligson H., Tate E., Mifflin E., Thomas W., Murphy J., and Jones C., *HAZUS-MH flood loss estimation methodology. I: Overview and flood hazard characterization*. Natural Hazards Review, 2006. 7(2): p. 60-71.
2. Scawthorn C., Flores P., Blais N., Seligson H., Tate E., Chang S., Mifflin E., Thomas W., Murphy J., and Jones C., *HAZUS-MH flood loss estimation methodology. II. Damage and loss assessment*. Natural Hazards Review, 2006. 7(2): p. 72-81.
3. O'Brien J., Julien P., and Fullerton W., *Two-dimensional water flood and mudflow simulation*. Journal of hydraulic engineering, 1993. 119(2): p. 244-261.
4. FLO-2D S.I., *FLO-2D® User's Manual*. 2004: Nutrioso, Arizona.
5. DeRisi R., Jalayer F., DePaola F., Iervolino I., Giugni M., Topa M.E., Mbuya E., Kyessi A., Manfredi G., and Gasparini P., *Flood Risk Assessment for Informal Settlements, Under Review*. Natural Hazards, 2013.
6. McKenna F., Fenves G., and Scott M., *OpenSees: Open system for earthquake engineering simulation*. Pacific Earthquake Engineering Center, University of California, Berkeley, CA., <http://opensees.berkeley.edu>, 2006.
7. Kelman I. and Spence R., *An overview of flood actions on buildings*. Engineering Geology, 2004. 73(3): p. 297-309.

Chapter 8

SUMMARY AND FINAL REMARKS

This thesis develops a probability-based procedure for flood risk assessment in urban areas with special attention to informal settlements. Flooding in urban areas can be classified as riverine and coastal. Riverine floods are mainly caused by the overflow of stream channels. Coastal floods can result from storm surges, unusually high tides, or tsunamis. Floods can also be a result of accidental situations, such as the breaching of a levee or a dam. This thesis has focused the attention on the Riverine floods.

In Chapter 2, the flooding phenomenon is described in detail, identifying its main elements: rainfall (IDF) curve, river network, catchment (basin), closure point, and hydrograph. Moreover, Chapter 2 lays out the main data acquisition requirements/instruments for flood risk assessment for a group of buildings. Here are some examples of data requirements on the hazard assessment side: historical rainfall data, climate change projections, topography (also the wetness topographic index, TWI), soil type, land use. As much as it regards the vulnerability and exposure, orthophotos and their by-products (buildings' footprints, the urban morphology types, UMT), Census information, sample field surveys and last but not least, laboratory tests for estimating the buildings' mechanical material properties, can be used as data resources.

It is worth noting that the flood risk assessment for informal settlements can be quite challenging due to lack of complete information. This thesis employs the Bayesian framework for taking into account not only all the available information but also the incomplete information and the uncertainties. This was done in a GIS-based environment given the necessity to

process and handle large amounts of geo-spatial data.

In Chapter 3 a classical method for the flood hazard assessment at micro-scale level is described, considering both historical data and climate change projections. This procedure produces the inundation profiles for a zone of interest given the flooding return period. The inundation profile, reported as the flooding heights (and velocities) for various nodes within a lattice covering a given area for different return periods, can be obtained by means of classic hydraulic routines of various degrees of sophistication and accuracy. The calculation of the inundation profiles can be summarized in a step-by-step manner as follows:

1. Definition of the rainfall curves for different return periods (T_R) based on historic rainfall annual maxima/ down-scaled climate projections.
2. Acquisition of cartographic information such as, digital elevation model (DEM), digital surface model (DSM), the geology map, and a representation of land use/land cover, for the zone(s) of interest.
3. Calculation of the hydrographs for the various return periods associated to the rainfall curves. The hydrograph refers to the flow discharge as a function of time and constitutes the input for the hydraulic diffusion model. The area under the hydrograph is equal to the total discharge volume for the basin under study.
4. Diffusion of the total discharge volume (area under the hydrograph) based on the general constitutive equations of continuity and fluid dynamics (i.e. one-dimensional or bi-dimensional diffusion models). This can be done by means of various software tools.

The inundation profile, obtained through a procedure similar to the one described above, is later used in Chapter 4 to delineate the inundated areas, for a given return period, as those areas within the zones of interest where the inundation height is greater than zero.

In this chapter (Chapter 3), a new method for point-wise representation of flooding hazard is proposed. In particular, the hazard curves (in terms of mean annual rate of exceeding a given flood depth) are extracted, for any given point within the zone of interest, using the inundation profiles as a basis.

Moreover, based on the inundation profiles, a power-law relationship is fitted to flooding velocity/height pairs, for any given point within the zone of interest. Establishing such relationship between height and velocity, helps in transforming a vector-based risk assessment problem (based on the vector of height and velocity values) to a scalar risk assessment problem using the maximum flooding height as the interface variable (between hazard and vulnerability).

The micro-scale flood hazard assessment has been performed for two case-study areas/neighborhoods: the Suna Subward, in Dar es Salaam (Tanzania) and the sub-city of Little Akaky in Addis Ababa (Ethiopia). It was demonstrated that climate change does not affect significantly the city of Dar es Salaam; meanwhile, it severely affects the city of Addis.

The micro-scale flood hazard assessment procedure described in Chapter 3 is propaedeutic to the novel developments in this work. In particular, the novel methodology proposed in Chapter 4 for meso-scale flood hazard assessment, the micro-scale flood vulnerability assessment procedure presented in Chapter 5 for a portfolio of informal settlements, and the procedure for the assessment of flooding risk in the urban areas, proposed in Chapter 6, all rely on flood hazard assessment.

In Chapter 4, a new procedure for meso-scale flood hazard assessment was presented. The potentially flood prone areas based on the TWI method were identified by delineating the areas distinguished with a TWI larger than a certain threshold. This threshold was calibrated based on available information, such as inundation profiles calculated for a certain area within the basin or delineated historically flood prone areas, as showed in Chapter 3. A probabilistic GIS-based method is used for calculating the maximum likelihood estimate and the 16th and 50th percentiles for the TWI threshold based on available inundation profiles/historically inundated areas. Bayesian parameter estimation was used to evaluate the threshold based on inundation profiles calculated for more than one area within the basin.

The proposed methodology is applied to the case study of Dar es Salaam and Addis Ababa. It is demonstrated that the maximum likelihood estimator of

TWI threshold is not sensitive to the return period corresponding to the inundation profile used for calibrating the TWI. Moreover, in both cases, the resulting likelihood function for the TWI threshold reveals an interval in which it reaches its maximum value and remains more-or-less invariable referred to as the 99% maximum likelihood interval.

It was also demonstrated that the proposed methodology can be used to estimate the TWI threshold using information from delineated flooded areas based on previous flooding events. In particular the proposed procedure is applied to Ouagadougou (Burkina Faso), based on available imagery of inundated areas for a relatively recent flooding event (2009). It is demonstrated that the TWI threshold can be successfully identified based on such information.

In Chapter 5, an efficient Bayesian simulation-based procedure for the assessment of flood vulnerability for a portfolio of structures is presented. The procedure for calculating the robust fragility curves for a class of structures is described in a detailed and step-by-step manner. It is also demonstrated that the portfolio fragility can be calculated as a weighted average of robust fragility curves for the various building classes identified within the portfolio. The robust fragility curves for a class of structures are represented as the statistics (e.g., various percentiles) of the plausible fragility curves inferred based on simulation of the various sources of uncertainty. The confidence interval reported by the robust fragility curves reflects the uncertainty due to limited number of simulations.

A set of three limit states is adopted based on a comprehensive description of flooding damage buildings. The limit states are: serviceability (SE), life safety (LS) and structural collapse (CO). For each limit state considered, the simulation procedure provides a set of critical water height values. These critical water height values are used then as data in order to calculate, using Bayesian parameter estimation, the posterior probability distribution for the parameters of prescribed analytic fragility functions.

Finally, the robust fragility is calculated as the expected fragility based on the posterior probability distribution calculated for the parameters of the prescribed analytic fragility functions. Note that this posterior probability distribution can be interpreted as the degree of belief in the analytic fragility model defined based on a specific set of parameters.

This simulation-based method relies on a detailed structural analysis procedure. Here are some of the salient aspects of the structural analysis procedure: structural modeling (e.g., modeling the openings, different type of boundary restraints, etc.) and loading (hydrostatic, hydrodynamic, accidental debris impact and material degradation).

A complete application of the portfolio vulnerability assessment procedure is demonstrated for a portion of the informal settlements located in the Suna subward, in Dar es Salaam. The resulting robust fragility curves are obtained based on, alternative extraction procedures, alternative boundary conditions, number of extractions, and the flood loading combinations. It is demonstrated that the results obtained with a large number of extractions (i.e. 200) are well contained in the confidence interval created by the robust fragility curves based on a small number of extractions (i.e. 20 and 50).

In Chapter 6, coherent with division of work in meso- and micro-scale, two alternative methodologies for flood risk assessment are presented. As far as it concerns the meso-scale assessment, urban flooding hot-spot for residential buildings and urban corridors (major roads) are delineated by overlaying three GIS-based datasets, namely, the topographic wetness index (TWI), the urban morphology types (UMT), and the population density. The flood prone areas delineated for various threshold statistics (e.g. ML, 16th percentile) are then overlaid with the UMT units identified as residential and major road corridors in order to identify the urban hot spot and the extent of the UMT units affected by flooding. Integrating the population density geo-spatial dataset as a third layer, leads to estimation of the number of people affected by flooding.

This methodology leads to evaluation of the potential flooding exposure of the urban area in consideration. In this thesis, the meso-scale flood risk assessment methodology is applied to the case study cities of Addis Ababa and Dar es Salaam. Arguably, urban hot spot identification can be considered as one of the fundamental initial steps in strategic urban planning, helping to establish zones of high exposure.. In addition to forming a basis for retrospective and pre-emptive urban planning, this information can be used in order to predict future urban trends and development scenarios.

It is also interesting to explore the possibility of further development the presented methodology for the identification of the urban hot spots in order to take into account: (a) spatial variation of flooding hazard within the flood prone areas; (b) variation of vulnerability within residential UMT spatial units.

Regarding to the micro-scale flood risk assessment, an integrated modular approach to flood risk assessment for structures in a portfolio of buildings is proposed. It integrates the climate modeling, hydrographic basin modeling and structural fragility modeling in order to generate point-wise risk maps for the zone of interest. The flooding risk is expressed as the annual probability of exceeding the structural limit state of interest and it is obtained by integrating the flooding hazard and fragility curves over the entire range of possible flooding heights. The total expected repair costs and the expected number of people affected by flooding can also be calculated based on the annual limit state probabilities.

An application to the Suna subward of Dar es Salaam illustrates the methodology. The case-study assessment is focused on the limit state of life safety which is defined as an ultimate state in the structure when the life of its inhabitants is in danger. It should be noted that the quantitative and novel approach presented in this thesis specifically for micro-scale flood risk assessment of informal settlements, is general with respect to the building classes considered. It can be extended to make vulnerability (and risk) assessments for a portfolio of buildings consisting of various classes of

structures.

In Chapter 7, a new software platform is developed that mirrors the micro-scale flood risk assessment procedure. VISK is a new software platform with a graphical user interface for micro-scale flood risk assessment for a single class of buildings. This software is particularly suitable for risk assessment based on incomplete information. This chapter discusses the main features of VISK. These features include: using manual orthophoto boundary recognition in order to capture the foot-print of the buildings considered; propagation of several sources of uncertainties (e.g., building-to-building variability, incomplete knowledge, limited number of surveys, limited number of simulations) in the calculation of structural fragility for a class of buildings; considering the correlation between discrete uncertain binary parameters; using Bayesian parameter estimation based on sample field survey results in order to characterize uncertainties; calculating the structural fragility using an efficient Bayesian small-sample simulation method; an exhaustive iterative procedure for localizing the structural damage in the model structure; considering the openings in the model structure; taking into account flood actions such as the hydro-static and hydro-dynamic pressure, the debris impact and material deterioration due to elongated contact with water, taking into account the effect of water-seepage in structural analysis. The robust fragility curves for the class of buildings are calculated for three limit states of serviceability (SE), structural collapse (CO), and life safety (LS). Various point-wise risk metrics are adopted in VISK for evaluating the flooding risk, namely, mean annual rate and annual probability of exceeding a prescribed limit state, expected loss, and expected number of people affected by flooding.

It should be noted that, although VISK is developed for micro-scale flood risk assessment of informal settlements, it could be applied to other building types in general.

As a perspective into future developments, various possible directions can be laid out. In the first place, it is interesting to note that the bi-scale flood

assessment procedure developed herein, has significant potentials for being integrated into a unique procedure. For example, the portfolio vulnerability assessment procedure be applied also at the meso-scale, based on the meso-scale delineation of urban hot spots and the class fragilities developed at the micro-scale. Therefore, a possible interesting future direction is that of developing an integrated probability-based multi-scale framework for the urban flood risk assessment. Clearly, this entails the application of fragility assessment methodology beyond the case of informal settlements.

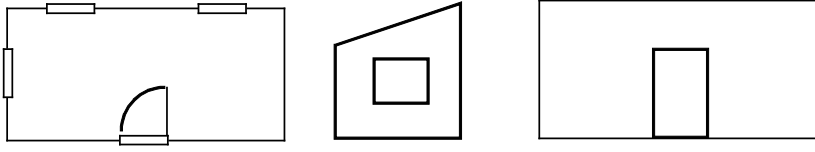

Another possible future direction is to further enrich the procedure by considering also the observed levels of flooding damage (i.e., the damage states). In the modular risk framework employed herein, this involves defining and integrating also the fragility/vulnerability curves that map the (quantified) structural performance to observed flooding damage states.

Needless to say, VISK is going to evolve continuously, following the future progress in flood risk assessment procedure. In particular, major developments are envisioned with regard to: a) extending the fragility calculations in order to consider than one typology/class of structural system; b) embedding a hydraulic calculation routine in the platform; and c) including the meso-scale risk assessment procedure.

Appendix A

THE SAMPLE FILED SURVEY SHEET

A typical survey sheet that filled during the phase of data acquisition in the field, Suna sub-ward, Dar Es Salaam.

PLAN VIEW WITH EXTERNAL SIZE				
				
PHOTO 1		PHOTO 2		
				
GPS Coordinates		06° 48.316' S 39° 15.974' E		
N° of stories	1		Height of story	3.55 m
Presence of Mezzanine (Mansard)			Yes <input type="checkbox"/>	No <input checked="" type="checkbox"/>
Geometrical size				
L (plan Length)	8.00 m		W (plan width)	3.40 m
Wall Material	Cement Blocks			
Wall Thickness	0.125 m			
Presence of cross connection in the corners	Yes <input checked="" type="checkbox"/>		No	<input type="checkbox"/>
Presence of buttresses	Yes <input type="checkbox"/>		No	<input checked="" type="checkbox"/>
Presence of plaster	Yes <input type="checkbox"/>		No	<input checked="" type="checkbox"/>
Presence of water-proof paint	Yes <input type="checkbox"/>		No	<input checked="" type="checkbox"/>
If the wall material is wood and mud:	Are the wooden piles anchored in foundation?		Yes <input type="checkbox"/>	No <input type="checkbox"/>
	Are the wooden horizontal piles connected and continuous over the perimeter?		Yes <input type="checkbox"/>	No <input type="checkbox"/>
Roof Typology	Flat	<input type="checkbox"/>	Pitch	<input checked="" type="checkbox"/>
			One Side	<input checked="" type="checkbox"/>
			Two Side	<input type="checkbox"/>
	Structural Material (a)	Corrugated Iron		
	Presence of roof beams	Yes <input checked="" type="checkbox"/>	If yes, material (b):	
		No <input type="checkbox"/>	wood	
	Presence of drainage or drip	Yes <input type="checkbox"/>	No <input checked="" type="checkbox"/>	
	Presence of roof coverage	Yes <input type="checkbox"/>	If yes, material (c):	
	No <input checked="" type="checkbox"/>			
Use of waterproof Material	Yes <input type="checkbox"/>	If yes, material:		
	No <input checked="" type="checkbox"/>			
Presence of foundation	No	<input type="checkbox"/>	Yes	<input checked="" type="checkbox"/>
			If yes:	
			Construction material	stone
		Elevation from ground	0.00 m	
Presence of lintel beam		Yes <input checked="" type="checkbox"/>		No <input type="checkbox"/>
Functionality of doors and windows (in impeding/delaying the water entrance)	Quality of the doors:	Good <input type="checkbox"/>	Bad <input checked="" type="checkbox"/>	
	Quality of the windows:	Good <input type="checkbox"/>	Bad <input checked="" type="checkbox"/>	
Minimum height of the windows above the floor	1.20 m			
Window dimensions	L (plan Length)	1.23 m	H (height)	1.20 m
Height of the door above the floor	0.00 m			
Door dimensions	L (plan Length)	1.22 m	H (height)	1.95 m
Presence of barrier in front of the door	No	<input type="checkbox"/>	Yes	<input checked="" type="checkbox"/>
			If yes:	
		Elevation from ground	1.00 m	